

## Precision Higgs Physics at the CEPC<sup>\*</sup>

Fenfen An<sup>4,21</sup> Yu Bai<sup>9</sup> Chunhui Chen<sup>21</sup> Xin Chen<sup>5</sup> Zhenxing Chen<sup>3</sup> Joao Guimaraes da Costa<sup>4</sup>  
 Zhenwei Cui<sup>3</sup> Yaquan Fang<sup>4,6</sup> Chengdong Fu<sup>4</sup> Jun Gao<sup>10</sup> Yanyan Gao<sup>20</sup> Yuanning Gao<sup>5</sup>  
 Shao-Feng Ge<sup>15,27</sup> Jiayin Gu<sup>13</sup> Fangyi Guo<sup>1,4</sup> Jun Guo<sup>10,11</sup> Tao Han<sup>5,29</sup> Shuang Han<sup>4</sup>  
 Hong-Jian He<sup>10,11</sup> Xianke He<sup>10</sup> Xiao-Gang He<sup>10,11</sup> Jifeng Hu<sup>10</sup> Shih-Chieh Hsu<sup>30</sup> Shan Jin<sup>8</sup>  
 Maoqiang Jing<sup>4,7</sup> Ryuta Kiuchi<sup>4</sup> Chia-Ming Kuo<sup>19</sup> Pei-Zhu Lai<sup>19</sup> Boyang Li<sup>5</sup> Congqiao Li<sup>3</sup> Gang Li<sup>4</sup>  
 Haifeng Li<sup>12</sup> Liang Li<sup>10</sup> Shu Li<sup>10,11</sup> Tong Li<sup>12</sup> Qiang Li<sup>3</sup> Hao Liang<sup>4,6</sup> Zhijun Liang<sup>4</sup>  
 Libo Liao<sup>4</sup> Bo Liu<sup>4,21</sup> Jianbei Liu<sup>1</sup> Tao Liu<sup>14</sup> Zhen Liu<sup>24,28</sup> Xinchou Lou<sup>4,6,31</sup> Lianliang Ma<sup>12</sup>  
 Bruce Mellado<sup>17</sup> Xin Mo<sup>4</sup> Mila Pandurovic<sup>16</sup> Jianming Qian<sup>22</sup> Zhuoni Qian<sup>18</sup>  
 Nikolaos Rompotis<sup>20</sup> Manqi Ruan<sup>4</sup> Alex Schuy<sup>30</sup> Lian-You Shan<sup>4</sup> Jingyuan Shi<sup>9</sup> Xin Shi<sup>4</sup>  
 Shufang Su<sup>23</sup> Dayong Wang<sup>3</sup> Jing Wang<sup>4</sup> Lian-Tao Wang<sup>25</sup> Yifang Wang<sup>4,6</sup> Yuqian Wei<sup>4</sup>  
 Yue Xu<sup>5</sup> Haijun Yang<sup>10,11</sup> Weiming Yao<sup>26</sup> Dan Yu<sup>4</sup> Kaili Zhang<sup>4,6</sup> Zhaoru Zhang<sup>4</sup>  
 Mingrui Zhao<sup>2</sup> Xianghu Zhao<sup>4</sup> Ning Zhou<sup>10</sup>

<sup>1</sup> Department of Modern Physics, University of Science and Technology of China, Anhui 230026, China

<sup>2</sup> China Institute of Atomic Energy, Beijing 102413, China

<sup>3</sup> School of Physics, Peking University, Beijing 100871, China

<sup>4</sup> Institute of High Energy Physics, Beijing 100049, China

<sup>5</sup> Department of Engineering Physics, Physics Department, Tsinghua University, Beijing 100084, China

<sup>6</sup> School of Physical Sciences, University of Chinese Academy of Science (UCAS), Beijing 100049, China

<sup>7</sup> School of Nuclear Science and Technology, University of South China, Hengyang 421001, China

<sup>8</sup> Department of Physics, Nanjing University, Nanjing 210093, China

<sup>9</sup> Department of Physics Southern Eastern University, Nanjing 210096, China

<sup>10</sup> School of Physics and Astronomy, Shanghai Jiao Tong University, KLPPAC-MoE, SKLPPC, Shanghai 200240, China

<sup>11</sup> Tsung-Dao Lee Institute, Shanghai 200240, China

<sup>12</sup> Institute of Frontier and Interdisciplinary Science and Key Laboratory of Particle Physics and Particle Irradiation (MOE), Shandong University, Qingdao 266237, China

<sup>13</sup> PRISMA Cluster of Excellence & Mainz Institute of Theoretical Physics, Johannes Gutenberg-Universität Mainz, Mainz 55128, Germany

<sup>14</sup> Department of Physics, Hong Kong University of Science and Technology, Hong Kong

<sup>15</sup> Kavli IPMU (WPI), UTIAS, The University of Tokyo, Kashiwa, Chiba 277-8583, Japan

<sup>16</sup> Vinca Institute of Nuclear Sciences, University of Belgrade, Belgrade 11000, Serbia

<sup>17</sup> School of Physics, University of the Witwatersrand, Johannesburg 2050, South Africa

<sup>18</sup> Center for Theoretical Physics of the Universe, Institute of Basic Science, Daejeon 34126, South Korea

<sup>19</sup> Department of Physics and Center for High Energy and High Field Physics, National Central University, Taoyuan City 32001, Taiwan

<sup>20</sup> Department of Physics, University of Liverpool, Liverpool L69 7ZX, United Kingdom

<sup>21</sup> Department of Physics and Astronomy, Iowa State University, Ames 50011-3160, USA

<sup>22</sup> Department of Physics, University of Michigan, Ann Arbor, Michigan 48109, USA

<sup>23</sup> Department of Physics, University of Arizona, Arizona 85721, USA

<sup>24</sup> Theoretical Physics Department, Fermi National Accelerator Laboratory, Batavia 60510, USA

<sup>25</sup> Department of Physics, University of Chicago, Chicago 60637, USA

<sup>26</sup> Lawrence Berkeley National Laboratory, Berkeley, California 94720, USA

<sup>27</sup> Department of Physics, University of California, Berkeley, California 94720, USA

<sup>28</sup> Maryland Center for Fundamental Physics, Department of Physics, University of Maryland, College Park, Maryland 20742, USA

<sup>29</sup> Department of Physics & Astronomy, University of Pittsburgh, Pittsburgh 15260, USA

<sup>30</sup> Department of Physics, University of Washington, Seattle 98195-1560, USA

<sup>31</sup> Department of Physics, University of Texas at Dallas, Texas 75080-3021, USA

**Abstract:** The discovery of the Higgs boson with its mass around 125 GeV by the ATLAS and CMS Collaborations marked the beginning of a new era in high energy physics. The Higgs boson will be the subject of extensive studies of the ongoing LHC program. At the same time, a lepton collider based Higgs factory has been proposed as a possible

Received XX August XXXX

\* Supported by the National Key Program for S&T Research and Development (2016YFA0400400); CAS Center for Excellence in Particle Physics; Yifang Wangs Science Studio of the Ten Thousand Talents Project; the CAS/SAFEA International Partnership Program for Creative Research Teams (H751S018S5); IHEP Innovation Grant (Y4545170Y2); Key Research Program of Frontier Sciences, CAS (XQYZDY-SSW-SLH002); Chinese Academy of Science Special Grant for Large Scientific Project (113111KYSB20170005); the National Natural Science Foundation of China(11675202); the Hundred Talent Programs of Chinese Academy of Science (Y3515540U1); the National 1000 Talents Program of China; Fermi Research Alliance, LLC (DE-AC02-07CH11359)

next step beyond the LHC, with its main goal as the precise measurement of the properties and probing potential new physics associated with the Higgs boson. The Circular Electron Positron Collider (CEPC) is one of such proposed Higgs factories. The CEPC is an  $e^+e^-$  circular collider proposed by China. Located in a tunnel of approximately 100 km in circumference, it will operate at a center-of-mass energy of 240 GeV as the Higgs factory. In this paper, we present the first estimates on the precision of Higgs property measurements achievable at the CEPC.

**Key words:** CEPC, Higgs boson, Higgs property measurement

**PACS:** 1-3 PACS(Physics and Astronomy Classification Scheme, <http://www.aip.org/pacs/pacs.html/>)

## 1 Introduction

The historic discovery of a Higgs boson in 2012 by the ATLAS and CMS collaborations [1, 2] at the Large Hadron Collider (LHC) has opened a new era in particle physics. Subsequent measurements of the properties of the new particle have indicated compatibility with the Standard Model (SM) Higgs boson [3–9]. While the SM has been remarkably successful in describing experimental phenomena, it is important to recognize that the SM is not a complete theory. In particular, the SM does not *predict* the parameters in the Higgs potential, such as the Higgs mass. The vast difference between the Planck scale and the weak scale remains a major mystery. There is not a complete understanding of the nature of electroweak phase transition. The discovery of a spin zero Higgs boson, the first elementary particle of its kind, only sharpens these questions. It is clear that any attempt of addressing these questions will involve new physics beyond the SM (BSM). Therefore, the Higgs boson discovery marks the beginning of a new era of theoretical and experimental explorations.

A physics program of precision measurement of Higgs properties will be a critical component of any roadmap for high energy physics in the coming decades. Potential new physics beyond the SM could lead to observable deviations in the Higgs boson couplings from the SM expectations. Typically, such deviations can be parametrized as

$$\delta = c \frac{v^2}{M_{\text{NP}}^2}, \quad (1)$$

where  $v$  and  $M_{\text{NP}}$  are the vacuum expectation value of the Higgs field and the typical mass scale of new physics, respectively. The size of the proportionality constant  $c$  depends on model, but it should not be much larger than  $\mathcal{O}(1)$ . The current and upcoming LHC runs will measure the Higgs couplings to about 5% [10]. At the same time, LHC will directly search for new physics from a few hundreds of GeV to at least a TeV. Eq. (1) implies that probing new physics significantly beyond the LHC reach would require the measurement of the Higgs boson couplings at least at percent level accuracy. To achieve such sub-percent level of precision will need new facilities, a lepton collider operating as a Higgs factory is a natural next step.

The Circular Electron-Positron Collider (CEPC), proposed by the Chinese particle physics community, is one of such possible facilities. The CEPC will be housed in a tunnel with a circumference about 100 km and will operate at a center-of-mass energy of  $\sqrt{s} \sim 240$  GeV, which maximizes the Higgs boson production cross section through the  $e^+e^- \rightarrow ZH$  process. At the CEPC, in contrast to the LHC, Higgs boson candidate events

can be identified through a technique known as the recoil mass method without tagging its decays. Therefore, Higgs boson production can be disentangled from its decay in a model independent way. Moreover, the cleaner environment at a lepton collider allows much better exclusive measurement of Higgs boson decay channels. All of these give the CEPC impressive reach in probing Higgs boson properties. With the expected integrated luminosity of  $5.6 \text{ ab}^{-1}$ , over one million Higgs bosons will be produced. With this sample, the CEPC will be able to measure the Higgs boson coupling to the  $Z$  boson with an accuracy of 0.25%, more than a factor of 10 better than the High Luminosity (HL)-LHC. Such a precise measurement gives the CEPC unprecedented reach into interesting new physics scenarios which are very difficult to probe at the LHC. The CEPC also has strong capability in detecting Higgs boson invisible decay. It is sensitive to the invisible decay branching ratio down to 0.30%. In addition, it is expected to have good sensitivities to exotic decay channels which are swamped by backgrounds at the LHC. It is also important to stress that an  $e^+e^-$  Higgs factory can perform *model independent* measurement of the Higgs boson width. This unique feature in turn allows for model independent determination of the Higgs boson couplings.

This paper documents the first studies of a precision Higgs boson physics program at the CEPC and serves as a supporting document to the CEPC Conceptual Design Report [11]. It is organized as follows: Section 2 briefly summarizes the collider and detector performance parameters assumed for the studies. Section 3 gives an overview of relevant  $e^+e^-$  collision processes and Monte Carlo simulations. Sections 4 and 5 describe inclusive and exclusive Higgs boson measurements. Section 6 discusses the combined analysis to extract Higgs boson production and decay properties. Section 7 interprets the results in the coupling and effective theory frameworks. Section 8 estimates the reaches in the test of Higgs boson spin/ $CP$  properties and in constraining the exotic decays of the Higgs boson based on previously published phenomenological studies. Finally the implications of all these measurements are discussed in Section 9.

## 2 CEPC Detector Concept

### 2.1 The CEPC operating scenarios

The CEPC is designed to operate as a Higgs factory at  $\sqrt{s} = 240$  GeV and as a  $Z$  factory at  $\sqrt{s} = 91.2$  GeV. It will also perform  $WW$  threshold scans around  $\sqrt{s} = 161$  GeV. Table 1 shows potential CEPC operating scenarios and the expected numbers of  $H$ ,  $W$  and  $Z$  bosons produced in these scenarios.

Table 1. CEPC operating scenarios and the numbers of Higgs,  $W$  and  $Z$  bosons produced. The integrated luminosity and the event yields assume two interaction points.

Operation mode	$Z$ factory	$WW$ scan	Higgs factory
$\sqrt{s}$ (GeV)	91.2	161	240
Instantaneous luminosity ( $10^{34} \text{ cm}^{-2} \text{ s}^{-1}$ )	16–32	10	3
Run time (year)	2	1	7
Integrated luminosity ( $\text{ab}^{-1}$ )	8–16	2.6	5.6
Higgs boson yield	–	–	$10^6$
$W$ boson yield	–	$10^7$	$10^8$
$Z$ boson yield	$10^{11-12}$	$10^9$	$10^9$

The CEPC operation as a Higgs factory will run for 7 years and produce a total of 1 Million Higgs bosons with two interaction points. Meanwhile, approximately 100 Million  $W$  bosons and 1 Billion  $Z$  bosons will also be produced in this operation. These large statistical samples of  $W$  and  $Z$  bosons will allow for in-situ detector characterization as well as for precise measurements of electroweak parameters. Benefiting from the clean  $e^+e^-$  collision environment and the large number of Higgs bosons, the CEPC is expected to improve the precision of most of the Higgs boson property measurements by a factor of ten over those achievable at the high luminosity LHC.

Running at the  $WW$  threshold around  $\sqrt{s} = 161$  GeV,  $10^7$   $W$  bosons will be produced in one year. Similarly running as a  $Z$  factory at  $\sqrt{s} = 91.2$  GeV, CEPC will produce  $10^{11-12}$   $Z$  bosons. These large samples will enable high precision measurements of the electroweak observables such as  $A_{FB}^b$ ,  $R_b$ , the  $Z$  boson line-shape parameters, the mass and width of the  $W$  boson. An order of magnitude or more improvement in the precision of these observables are foreseen.

## 2.2 Conceptual detector design

The primary physics objective of the CEPC is the precise determination of the Higgs boson properties. Therefore CEPC detectors must be able to reconstruct and identify all key physics objects that the Higgs bosons are produced with or decay into with high efficiency, purity and accuracy. These objects include charged leptons, photons, jets, missing energy and missing momentum. Moreover, the flavor tagging of jets, such as those from  $b$ ,  $c$  and light quarks or gluons, are crucial for identifying the hadronic decays of Higgs bosons. The detector requirements for the electroweak and flavor physics are similar. One notable additional requirement is the identification of charged particles such as  $\pi^\pm$  and  $K^\pm$  for the flavor physics program.

Using the International Large Detector (ILD) [12, 13]

as a reference, a Particle Flow oriented conceptual detector, CEPC-v1 (see Fig. 1), has been developed for the CEPC. A detailed description of the CEPC-v1 detector can be found in Ref. [14]. Originally developed for LEP experiments [15, 16], Particle Flow is a well validated principle for event reconstructions [17–20] and is based on the premise of reconstructing all visible final-state particles in the most sensitive subdetector system. Specifically, a particle-flow algorithm reconstructs charged particles in the tracking system, measures photons in the electromagnetic calorimeter and neutral hadrons in both electromagnetic and hadronic calorimeters. Physics objects are then identified or reconstructed from the unique list of final state particles. Particle Flow reconstruction provides a coherent interpretation of an entire physics event and, therefore, is particularly well suited for the identification of composite physics objects such as the  $\tau$  leptons and jets.

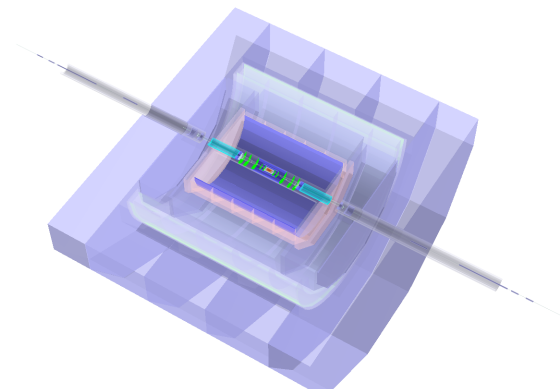


Fig. 1. Conceptual CEPC detector, CEPC-v1, implemented in MOKKA [21] and GEANT 4 [22]. It is comprised of a silicon vertexing and tracking system of both pixel and strips geometry, a TPC tracker, a high granularity calorimeter system, a solenoid of 3.5 Tesla magnetic field, and a muon detector embedded in a magnetic field return yoke.

Particle Flow algorithm requires good spatial separations of calorimeter showers induced by different final state particles for their reconstruction. It is imperative to minimize the amount of material before the calorimeter to reduce the uncertainty induced by the nuclear interactions and Bremsstrahlung radiations. Therefore, a high granularity calorimeter system and low material tracking system are implemented in the CEPC-v1 detector concept. The tracking system consists of silicon vertexing and tracking detectors as well as a Time Projection Chamber (TPC). The calorimetry system is based on the sampling technology with absorber/active-medium combination of Tungsten-Silicon for the electromagnetic calorimeter (ECAL) and Iron-Scintillator for the hadronic calorimeter (HCAL). The calorimeters are segmented at about 1 channel/cm<sup>3</sup>, three orders of magnitude finer than those of the LHC detectors. Both the tracking and the calorimeter system are housed inside a solenoid of 3.5 Tesla magnetic field. The CEPC-v1 detector has a sophisticated machine-detector interface with an 1.5 meter L\* (the distance between the interaction point and the final focusing quadrupole magnet) to accommodate the high design luminosity. Table 2 shows the geometric parameters and the benchmark subdetector performances of the CEPC-v1 detector. A quartic view of the detector is shown in Fig. 2.

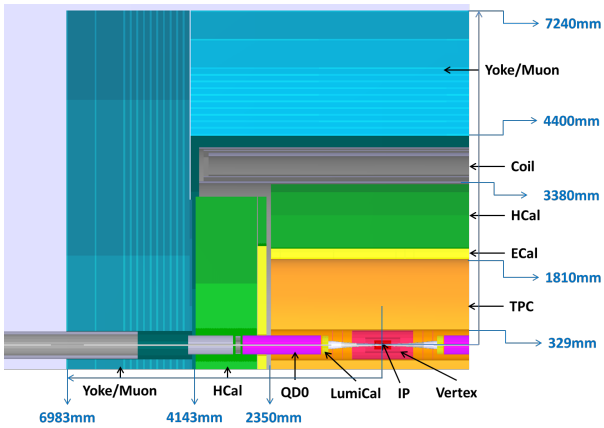


Fig. 2. A schematic quartic view of the CEPC-v1 detector.

### 2.3 Object reconstruction and identification

A dedicated Particle Flow reconstruction toolkit, ARBOR [18], has been developed for the CEPC-v1 detector. Inspired by the tree structure of particle showers, ARBOR attempts to reconstruct every visible final state particle. Figure 3 illustrates a simulated  $e^+e^- \rightarrow ZH \rightarrow q\bar{q}b\bar{b}$  event as reconstructed by the ARBOR algorithm. The al-

gorithm's performance for leptons, photons and jets are briefly summarized here. More details can be found in Ref. [23, 24].

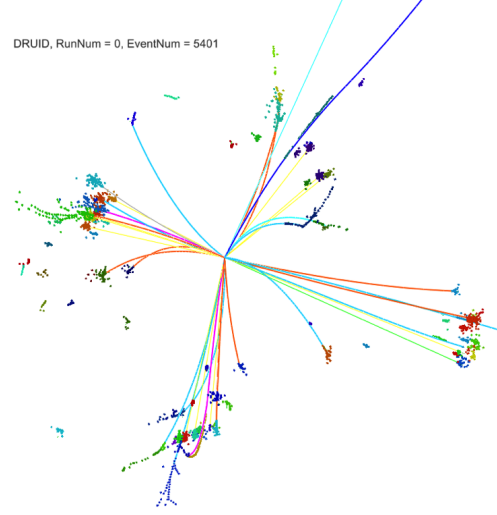


Fig. 3. A simulated  $e^+e^- \rightarrow ZH \rightarrow q\bar{q}b\bar{b}$  event reconstructed with the ARBOR algorithm. Different types of reconstructed final state particles are represented in different colors.

#### 2.3.1 Leptons and Photons

Leptons ( $\ell$ )\* are fundamental for the measurements of the Higgs boson properties at the CEPC. About 7% of the Higgs bosons are produced in association with a pair of leptons through the  $e^+e^- \rightarrow ZH \rightarrow \ell^+\ell^-H$  process. These events allow for the identifications of Higgs bosons using the recoil mass information and therefore enable the measurement of the  $ZH$  production cross section and the Higgs boson mass. Moreover, a significant fraction of Higgs bosons decay into final states with leptons indirectly through the  $W$  or  $Z$  bosons as well as the  $\tau$  leptons. These leptons serve as signatures for identifying different Higgs boson decay modes.

A lepton identification algorithm, LICH [25], has been developed and integrated into ARBOR. Efficiencies close to 99.9% for identifying electrons and muons with energies above 2 GeV have been achieved while the misidentification rates from hadrons are limited to be less than 1%. The CEPC-v1 tracking system provides an excellent momentum resolution that is about ten times better than those of the LEP and LHC detectors. The good resolution is illustrated in the narrow invariant mass distribution of muon pairs from the  $H \rightarrow \mu^+\mu^-$  decays as shown in Fig. 4(a).

\*Unless otherwise noted, leptons refer to electrons and muons or their antiparticles thereafter, i.e.  $\ell = e, \mu$ .

Table 2. Basic parameters and performances of the CEPC-v1 detector. The radiation length ( $X_0$ ) and the nuclear interaction length ( $\lambda$ ) are measured at normal incidences. The cell sizes are for transverse readout sensors and the layer numbers are for longitudinal active readouts.

Tracking system	
Vertex detector	6 layers pixel layers
Silicon tracker	3 barrel layers, 6 forward disks each side
Time projection chamber	220 radial readouts
Calorimetry	
ECAL	W/Si, $24X_0$ , $5 \times 5$ mm <sup>2</sup> cell with 30 layers
HCAL	Fe/Scintillator, $6\lambda$ , $10 \times 10$ mm <sup>2</sup> cell with 40 layers
Performances	
Track momentum resolution	$\Delta(1/p_T) \sim 2 \times 10^{-5}$ (1/GeV)
Impact parameter resolution	$5 \mu\text{m} \oplus 10 \mu\text{m}/[(p/\text{GeV})(\sin\theta)^{3/2}]$
ECAL energy resolution	$\Delta E/E \sim 16\%/\sqrt{E/\text{GeV}} \oplus 1\%$
HCAL energy resolution	$\Delta E/E \sim 60\%/\sqrt{E/\text{GeV}} \oplus 1\%$

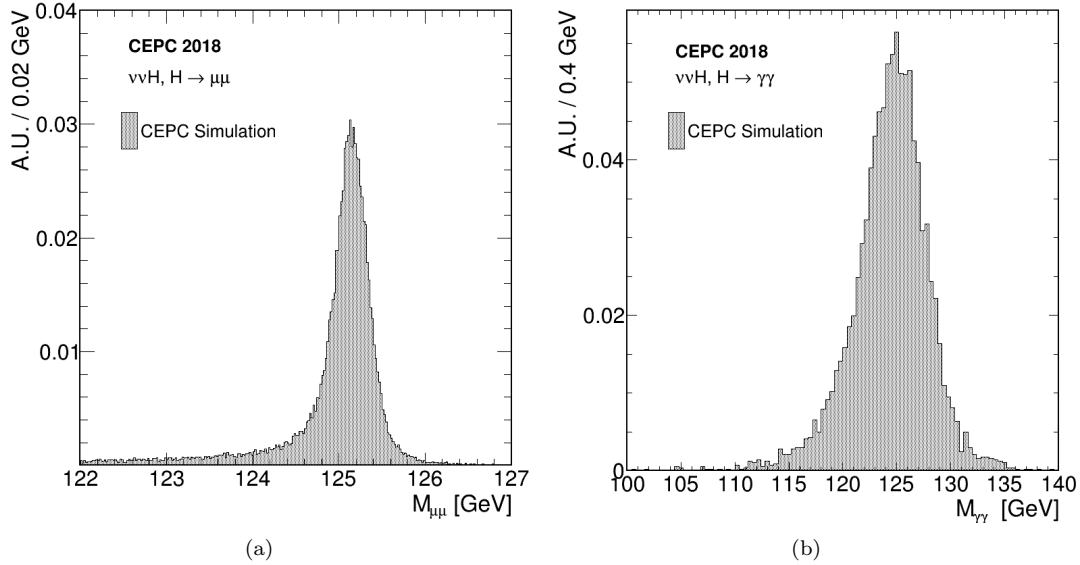


Fig. 4. Simulated invariant mass distributions of (a) muon pairs from  $H \rightarrow \mu^+\mu^-$  and (b) photon pairs from  $H \rightarrow \gamma\gamma$ , both from the  $e^+e^- \rightarrow ZH$  process with the  $Z \rightarrow \nu\bar{\nu}$  decay. The  $M_{\mu^+\mu^-}$  distribution is fit with a Gaussian core plus a small low-mass tail from the Bremsstrahlung radiation. The Gaussian has a width of 0.2 GeV, representing a relative mass resolution of 0.16%. The  $M_{\gamma\gamma}$  distribution is described well by a Crystal Ball function with a width of 3.1 GeV, corresponding to a relative mass resolution of 2.5%.

Photons are essential for the studies of  $H \rightarrow \gamma\gamma$  and  $H \rightarrow Z\gamma$  decays. They are also important for the reconstructions and measurements of  $\tau$  leptons and jets. The  $H \rightarrow \gamma\gamma$  decay is an ideal process to characterize the photon performance of the CEPC-v1. Figure 4(b) shows the invariant mass distribution of photon pairs from the  $H \rightarrow \gamma\gamma$  decays.

### 2.3.2 Jets

Approximately 70% of Higgs bosons decay directly into jets ( $b\bar{b}, c\bar{c}, gg$ ) and an additional 22% decay indirectly into final states with jets through the  $H \rightarrow WW^*, ZZ^*$  cascades. Therefore, efficient jet reconstruction and precise measurements of their momenta are pre-requisite for a precision Higgs physics program. In ARBOR, jets are reconstructed using the Durham algo-

rithm [26]. As a demonstration of the CEPC-v1 jet performance, Fig. 5 shows the reconstructed dijet invariant mass distributions of the  $W \rightarrow q\bar{q}$ ,  $Z \rightarrow q\bar{q}$  and  $H \rightarrow b\bar{b}/c\bar{c}/g\bar{g}$  decays from the  $ZZ \rightarrow \nu\bar{\nu}q\bar{q}$ ,  $WW \rightarrow \ell\nu q\bar{q}$  and  $ZH \rightarrow \nu\bar{\nu}(b\bar{b}/c\bar{c}/g\bar{g})$  processes respectively. Compared with  $W \rightarrow q\bar{q}$ , the  $Z \rightarrow q\bar{q}$  and  $H \rightarrow b\bar{b}/c\bar{c}/g\bar{g}$  distributions have long low-mass tails, resulting from the heavy-flavor jets in these decays. The jet energy resolution is expected to be between 3–5% for the jet energy range relevant at the CEPC. This resolution is approximately 2–4 times better than those of the LHC experiments. The dijet mass resolution for the  $W$  and  $Z$  bosons is approximately 4.4%, which allows for an average separation of  $2\sigma$  or better of the two decays.

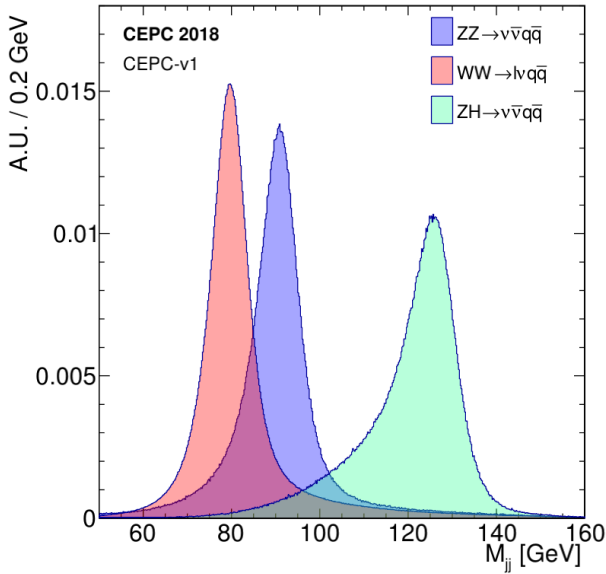


Fig. 5. Distributions of the reconstructed dijet invariant mass for the  $W \rightarrow q\bar{q}$ ,  $Z \rightarrow q\bar{q}$  and  $H \rightarrow b\bar{b}/c\bar{c}/g\bar{g}$  decays from, respectively, the  $WW \rightarrow \ell\nu q\bar{q}$ ,  $ZZ \rightarrow \nu\bar{\nu}q\bar{q}$  and  $ZH \rightarrow \nu\bar{\nu}(b\bar{b}/c\bar{c}/g\bar{g})$  processes. All distributions are normalized to unit area.

Jets originating from heavy flavors ( $b$ - or  $c$ -quarks) are tagged using the LCFIPlus algorithm [27]. The algorithm combines information from the secondary vertex, jet mass, number of leptons etc. to construct  $b$ -jet and  $c$ -jet discriminating variables. The tagging performance characterized using the  $Z \rightarrow q\bar{q}$  decays from the  $Z$  pole running is shown in Fig. 6. For an inclusive  $Z \rightarrow q\bar{q}$  sample,  $b$ -jets can be tagged with an efficiency of 80% and a purity of 90% while the corresponding efficiency and purity for tagging  $c$ -jets are 60% and 60%, respectively.

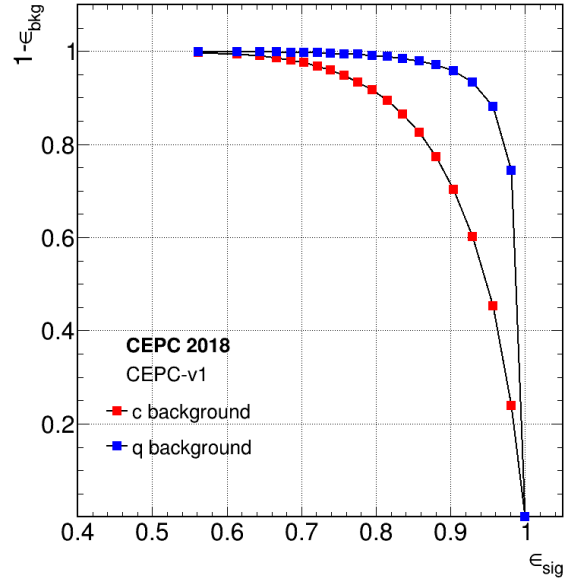


Fig. 6. Efficiency for tagging  $b$ -jets vs rejection for light-jet background (blue) and  $c$ -jet background (red), determined from an inclusive  $Z \rightarrow q\bar{q}$  sample from the  $Z$  pole run.

## 2.4 Ongoing optimization

The CEPC-v1 detector concept is used as the reference detector for the studies summarized in this paper. A series of optimizations have been performed meanwhile. These optimizations are intended to reduce the power consumption and the construction cost and to improve the machine-detector interface while minimizing negative impacts on the Higgs boson physics. An updated detector concept, CEPC-v4, has thus been developed. The CEPC-v4 has a smaller solenoidal field of 3 Tesla and a reduced calorimeter dimensions along with fewer readout channels. In particular, the ECAL readout sensor size is changed from  $5 \times 5 \text{ mm}^2$  to  $10 \times 10 \text{ mm}^2$ . A new Time-of-Flight measurement capability is added to improve the flavor physics potential.

The weaker magnetic field degrades momentum resolution for charged particles by 14% which translates directly into a degraded muon momentum resolution. The impact on other physics objects such as electrons, photons and jets are estimated to be small as the track momentum resolution is not a dominant factor for their performances. In parallel with the detector optimization, the accelerator design has chosen 240 GeV as the nominal center-of-mass energy for the Higgs factory. However, the simulation of CEPC-v1 assumes  $\sqrt{s} = 250 \text{ GeV}$ . The estimated precision of Higgs boson property measurements for CEPC-v1 operating at 250 GeV are therefore extrapolated to obtain those for CEPC-v4 at  $\sqrt{s} = 240 \text{ GeV}$ , as discussed Section 6.2. Figure 7 compares the dimuon invariant mass distribution of  $H \rightarrow \mu^+\mu^-$  and the recoil mass distribution of  $Z \rightarrow \mu^+\mu^-$  of  $e^+e^- \rightarrow ZH$

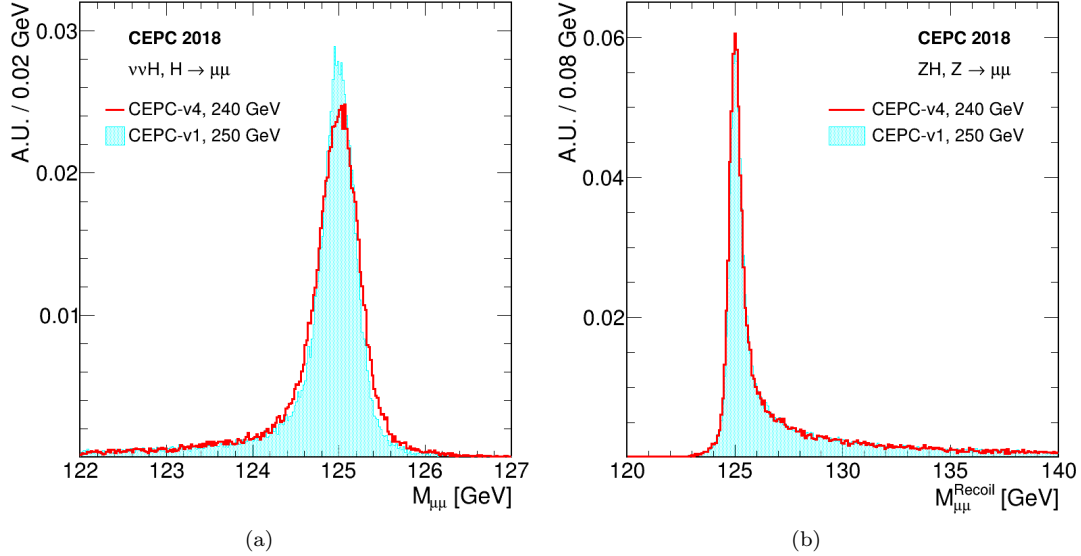


Fig. 7. (a) The dimuon invariant mass distribution of  $H \rightarrow \mu^+\mu^-$  and (b) the recoil mass distribution of  $Z \rightarrow \mu^+\mu^-$ , both from the  $e^+e^- \rightarrow ZH$  process, comparing CEPC-v1 at 250 GeV and CEPC-v4 at 240 GeV. All distributions are normalized to unit area.

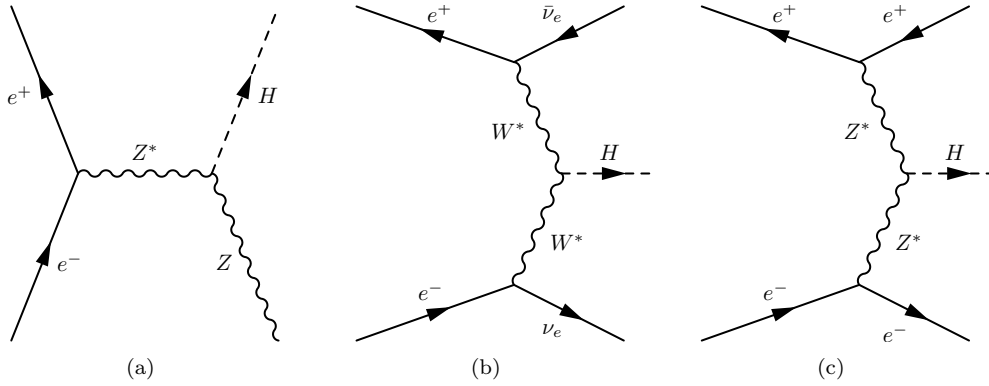


Fig. 8. Feynman diagrams of the Higgs boson production processes at the CEPC: (a)  $e^+e^- \rightarrow ZH$ , (b)  $e^+e^- \rightarrow \nu_e\bar{\nu}_eH$  and (c)  $e^+e^- \rightarrow e^+e^-H$ .

events simulated for CEPC-v1 and CEPC-v4 concepts. As expected, there are small but noticeable differences

in the former and little difference in the latter.

### 3 Theory and Monte Carlo Samples

#### 3.1 Higgs boson production and decay

Production processes for a 125 GeV SM Higgs boson at the CEPC operating at  $\sqrt{s} \sim 240 - 250$  GeV are  $e^+e^- \rightarrow ZH$  ( $ZH$  associate production or Higgsstrahlung),  $e^+e^- \rightarrow \nu_e\bar{\nu}_eH$  ( $W$  fusion) and  $e^+e^- \rightarrow e^+e^-H$  ( $Z$  fusion) as illustrated in Fig. 8. The  $W$  and  $Z$  fusion processes are collectively referred to as vector-boson fusion (VBF) production.

The total and individual cross sections for the pro-

duction of a SM Higgs boson with a mass of 125 GeV as functions of center-of-mass energy are plotted in Fig. 9 while its decay branching ratios and total width are shown in Table 3. As an  $s$ -channel process, the cross section of the  $e^+e^- \rightarrow ZH$  process reaches its maximum at  $\sqrt{s} \sim 250$  GeV, and then decreases asymptotically as  $1/s$ . The VBF production processes are through  $t$ -channel exchanges of vector bosons. Their cross sections increase logarithmically as  $\ln^2(s/M_V^2)$ . Because of the accidental small neutral-current  $Zee$  coupling, the VBF cross section is dominated by the  $W$  fusion process.

Numerical values of these cross sections at  $\sqrt{s} = 250$  GeV are listed in Table 4. Because of the interference effects between  $e^+e^- \rightarrow ZH$  and  $e^+e^- \rightarrow \nu_e\bar{\nu}_eH$  for the  $Z \rightarrow \nu_e\bar{\nu}_e$  decay and between  $e^+e^- \rightarrow ZH$  and  $e^+e^- \rightarrow e^+e^-H$  for the  $Z \rightarrow e^+e^-$  decay, the cross sections of these processes cannot be separated. The breakdowns in Fig. 9 and Table 4 are for illustration only. The  $e^+e^- \rightarrow ZH$  cross section shown is from Fig. 8(a) only whereas the  $e^+e^- \rightarrow \nu_e\bar{\nu}_eH$  and  $e^+e^- \rightarrow e^+e^-H$  cross sections include contributions from their interferences with the  $e^+e^- \rightarrow ZH$  process.

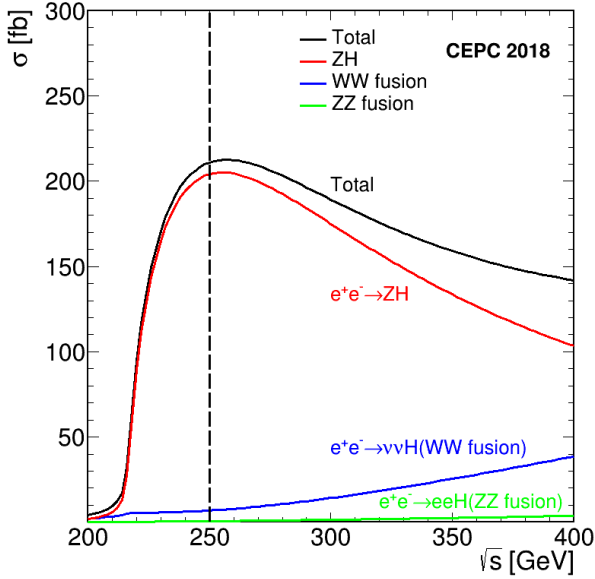


Fig. 9. Production cross sections of  $e^+e^- \rightarrow ZH$  and  $e^+e^- \rightarrow (e^+e^-/\nu\bar{\nu})H$  as functions of  $\sqrt{s}$  for a 125 GeV SM Higgs boson. The vertical indicates  $\sqrt{s} = 250$  GeV, the energy assumed for most of the studies summarized in this paper.

The CEPC as a Higgs boson factory is designed to deliver a total of  $5.6\text{ab}^{-1}$  integrated luminosity to two detectors in 7 years. Over  $10^6$  Higgs boson events will be produced during this period. The large statistics, well-defined event kinematics and clean collision environment will enable the CEPC to measure Higgs boson production cross sections as well as its properties (mass, decay width and branching ratios, etc.) with precision far beyond those achievable at the LHC. Compared with hadron collisions,  $e^+e^-$  collisions are unaffected by underlying event and pile-up effects. Theoretical calculations are less dependent on higher order QCD radiative corrections. Therefore, more precise tests of theoretical predictions can be performed at the CEPC. The tagging of  $e^+e^- \rightarrow ZH$  events using the invariant mass of the system recoiling against the  $Z$  boson, independent of the Higgs boson decay, is unique to lepton colliders. It provides a powerful tool for the model-independent measurements of the inclusive  $e^+e^- \rightarrow ZH$  production cross

section,  $\sigma(ZH)$ , and of Higgs boson decay branching ratios. Combinations of these measurements will enable to determine the total Higgs boson decay width and to extract the Higgs boson couplings to fermions and vector bosons, providing sensitive probes to potential new physics beyond the SM.

### 3.2 Background processes

Apart from Higgs boson production, other SM processes include  $e^+e^- \rightarrow e^+e^-$  (Bhabha scattering),  $e^+e^- \rightarrow Z\gamma$  (ISR return),  $e^+e^- \rightarrow WW/ZZ$  (diboson) as well as the single boson production of  $e^+e^- \rightarrow e^+e^-Z$  and  $e^+e^- \rightarrow e^+\nu W^-/e^-\bar{\nu}W^+$ . Their cross sections and expected numbers of events for an integrated luminosity of  $5.6\text{ab}^{-1}$  at  $\sqrt{s} = 250$  GeV are shown in Table 4 as well. The energy dependence of the cross sections for these and the Higgs boson production processes are shown Fig. 10. Note that many of these processes can lead to identical final states and thus can interfere. For example,  $e^+e^- \rightarrow e^+\nu_e W^- \rightarrow e^+\nu_e e^-\bar{\nu}_e$  and  $e^+e^- \rightarrow e^+e^-Z \rightarrow e^+e^-\nu_e\bar{\nu}_e$  have the same final state. Unless otherwise noted, these processes are simulated together to take into account interference effects for the studies presented in this paper. The breakdowns shown in the table and figure are for illustration only.

Along with  $1.2 \times 10^6$  Higgs boson events,  $5.8 \times 10^6$   $ZZ$ ,  $8.6 \times 10^7$   $WW$  and  $2.8 \times 10^8$   $q\bar{q}(\gamma)$  events will be produced. Though these events are backgrounds to Higgs boson events, they are important for the calibration and characterization of the detector performances and for the measurements of electroweak parameters.

### 3.3 Event generation and simulation

The following software tools have been used to generate events, simulate detector responses and reconstruct simulated events. A full set of SM samples, including both the Higgs boson signal and SM background events, are generated with WHIZARD [30]. The generated events are then processed with MokkaC [21], the official CEPC simulation software based on the framework used for ILC studies [31]. Limited by computing resources, background samples are often pre-selected with loose generator-level requirements or processed with fast simulation tools.

All Higgs boson signal samples and part of the leading background samples are processed with Geant4 [22] based full detector simulation and reconstruction. The rest of backgrounds are simulated with a dedicated fast simulation tool, where the detector acceptances, efficiencies, intrinsic resolutions for different physics objects are parametrized. Samples simulated for ILC studies [32] are used for cross checks of some studies.

Table 3. Standard model predictions of the decay branching ratios and total width of a 125 GeV Higgs boson. These numbers are obtained from Refs. [28, 29].

Decay mode	Branching ratio	Relative uncertainties
$H \rightarrow b\bar{b}$	57.7%	+3.2%, -3.3%
$H \rightarrow c\bar{c}$	2.91%	+12%, -12%
$H \rightarrow \tau^+\tau^-$	6.32%	+5.7%, -5.7%
$H \rightarrow \mu^+\mu^-$	$2.19 \times 10^{-4}$	+6.0%, -5.9%
$H \rightarrow WW^*$	21.5%	+4.3%, -4.2%
$H \rightarrow ZZ^*$	2.64%	+4.3%, -4.2%
$H \rightarrow \gamma\gamma$	$2.28 \times 10^{-3}$	+5.0%, -4.9%
$H \rightarrow Z\gamma$	$1.53 \times 10^{-3}$	+9.0%, -8.8%
$H \rightarrow gg$	8.57%	+10%, -10%
$\Gamma_H$	4.07 MeV	+4.0%, -4.0%

 Table 4. Cross sections of Higgs boson production and other SM processes at  $\sqrt{s} = 250$  GeV and numbers of events expected in  $5.6 \text{ ab}^{-1}$ . The cross sections are calculated using the Whizard program [30]. Note that there are interferences between the same final states from different processes after the  $W$  or  $Z$  boson decays. Their treatments are explained in the text.

Process	Cross section	Events in $5.6 \text{ ab}^{-1}$
Higgs boson production, cross section in fb		
$e^+e^- \rightarrow ZH$	204.7	$1.15 \times 10^6$
$e^+e^- \rightarrow \nu_e\bar{\nu}_e H$	6.85	$3.84 \times 10^4$
$e^+e^- \rightarrow e^+e^- H$	0.63	$3.53 \times 10^3$
Total	212.1	$1.19 \times 10^6$
Background processes, cross section in pb		
$e^+e^- \rightarrow e^+e^-$ (Bhabha)	25.1	$1.4 \times 10^8$
$e^+e^- \rightarrow q\bar{q}(\gamma)$	50.2	$2.8 \times 10^8$
$e^+e^- \rightarrow \mu^+\mu^- (\gamma)$ [or $\tau^+\tau^- (\gamma)$ ]	4.40	$2.5 \times 10^7$
$e^+e^- \rightarrow WW$	15.4	$8.6 \times 10^7$
$e^+e^- \rightarrow ZZ$	1.03	$5.8 \times 10^6$
$e^+e^- \rightarrow e^+e^- Z$	4.73	$2.7 \times 10^7$
$e^+e^- \rightarrow e^+\nu W^- / e^-\bar{\nu} W^+$	5.14	$2.9 \times 10^7$

## 4 Higgs Boson Tagging using Recoil Mass

Unlike in hadron collisions, the energy of  $e^+e^-$  collisions is known. For a Higgsstrahlung event where the  $Z$  boson decays to a pair of visible fermions ( $ff$ ), the mass of the system recoiling against the  $Z$  boson, commonly known as the recoil mass, can be calculated assuming the event has a total energy  $\sqrt{s}$  and zero total momentum:

$$M_{\text{recoil}}^2 = (\sqrt{s} - E_{ff})^2 - p_{ff}^2 = s - 2E_{ff}\sqrt{s} + m_{ff}^2. \quad (2)$$

Here  $E_{ff}$ ,  $p_{ff}$  and  $m_{ff}$  are, respectively, the total energy, momentum and invariant mass of the fermion pair. The  $M_{\text{recoil}}$  distribution should show a peak at the Higgs boson mass  $m_H$  for  $e^+e^- \rightarrow ZH$  and  $e^+e^- \rightarrow e^+e^- H$  processes, and is expected to be smooth without a resonance structure for other processes in the mass region around 125 GeV.

Two important measurements of the Higgs boson can be performed from the  $M_{\text{recoil}}$  mass spectrum. The Higgs boson mass can be measured from the peak position of the resonance. The width of the resonance is dominated by the beam energy spread (including ISR effects) and

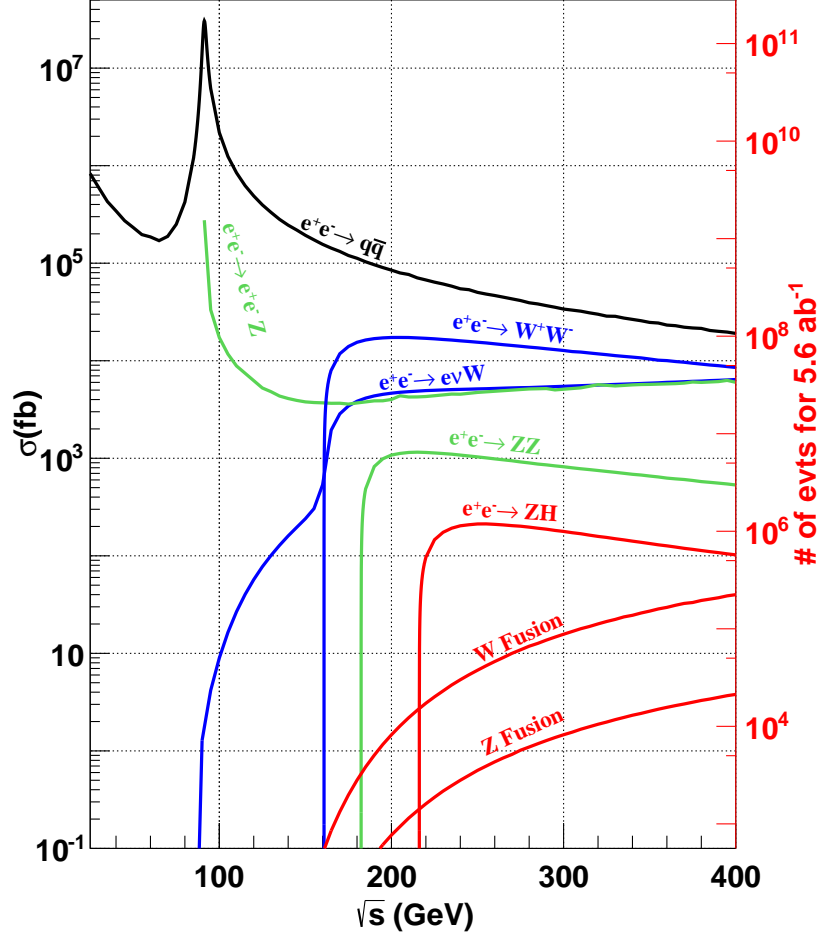


Fig. 10. Cross sections of main Standard Model processes of  $e^+e^-$  collisions as functions of center-of-mass energy  $\sqrt{s}$  obtained from the Whizard program [30]. The calculations include initial-state radiations (ISR). The single  $W$  and  $Z$  processes refer to  $e^+e^- \rightarrow e^+\nu W^-/e^-\bar{\nu}W^+$  and  $e^+e^- \rightarrow e^+e^-Z$  production, respectively. The  $W$  and  $Z$  fusion processes refer to  $e^+e^- \rightarrow \nu\bar{\nu}H$  and  $e^+e^- \rightarrow e^+e^-H$  production, respectively. Their numerical values at  $\sqrt{s} = 250$  GeV can be found in Table 4.

energy/momentum resolution of the detector as the natural Higgs boson width is only 4.07 MeV. The best precision of the mass measurement can be achieved from the leptonic  $Z \rightarrow \ell^+\ell^-$  ( $\ell = e, \mu$ ) decays. The height of the resonance is a measure of the Higgs boson production cross section  $\sigma(ZH)^\dagger$ . By fitting the  $M_{\text{recoil}}$  spectrum, the  $e^+e^- \rightarrow ZH$  event yield, and therefore  $\sigma(ZH)$ , can be extracted, independent of Higgs boson decays. Higgs boson branching ratios can then be determined by studying Higgs boson decays in selected  $e^+e^- \rightarrow ZH$  candidates. The recoil mass spectrum has been investigated for both leptonic and hadronic  $Z$  boson decays as presented below.

#### 4.1 $Z \rightarrow \ell^+\ell^-$

Leptonic  $Z$  decay is ideal for studying the recoil mass spectrum of the  $e^+e^- \rightarrow ZX$  events. The decay is easily identifiable and the lepton momenta can be precisely measured. Figure 11 shows the reconstructed recoil mass spectra of  $e^+e^- \rightarrow ZX$  candidates for the  $Z \rightarrow \mu^+\mu^-$  and  $Z \rightarrow e^+e^-$  decay modes. The analyses are based on the full detector simulation for the signal events and on the fast detector simulation for background events. They are performed with event selections entirely based on the information of the two leptons, independent of the final states of Higgs boson decays. This approach is essen-

<sup>†</sup>For the  $Z \rightarrow e^+e^-$  decay, there will be a small contribution from  $e^+e^- \rightarrow e^+e^-H$  production.

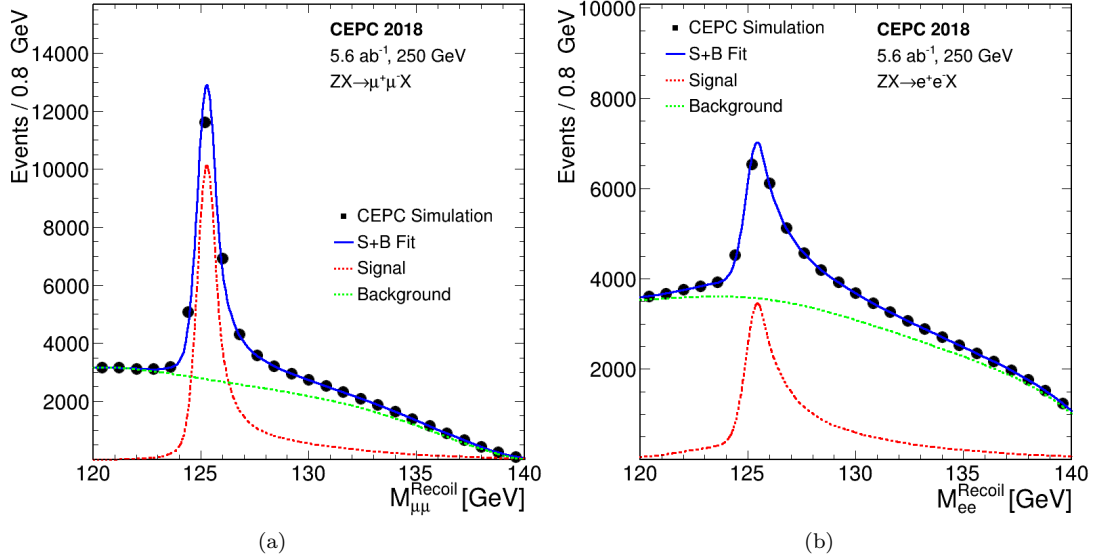


Fig. 11. The inclusive recoil mass spectra of  $e^+e^- \rightarrow ZX$  candidates for (a)  $Z \rightarrow \mu^+\mu^-$  and (b)  $Z \rightarrow e^+e^-$ . No attempt to identify  $X$  is made. The markers and their uncertainties represent expectations from a CEPC dataset of  $5.6\text{ab}^{-1}$  whereas the solid blue curves are the fit results. The dashed curves are the signal and background components.

tial for the measurement of the inclusive  $e^+e^- \rightarrow ZH$  production cross section and the model-independent determination of the Higgs boson branching ratios. SM processes with at least 2 leptons in their final states are considered as backgrounds.

The event selection of the  $Z \rightarrow \mu^+\mu^-$  decay mode starts with the requirement of a pair of identified muons. Events must have the dimuon invariant mass in the range of 80–100 GeV and the recoil mass between 120 GeV and 140 GeV. The muon pair is required to have its transverse momentum larger than 20 GeV, and its opening angle smaller than  $175^\circ$ . A Boost Decision Tree (BDT) technique is employed to enhance the separation between signal and background events. The BDT is trained using the invariant mass, transverse momentum, polar angle and acollinearity of the dimuon system. Leading background contributions after the selection are from  $ZZ$ ,  $WW$  and  $Z\gamma$  events. As shown in Fig. 11(a), the analysis has a good signal-to-background ratio. The long high-mass tail is largely due to the initial-state radiation.

Compared to the analysis of the  $Z \rightarrow \mu^+\mu^-$  decay, the analysis of the  $Z \rightarrow e^+e^-$  decay suffers from additional and large background contributions from Bhabha and single boson production. A cut based event selection is performed for the  $Z \rightarrow e^+e^-$  decay. The electron-positron pair is required to have its invariant mass in the range of 86.2–96.2 GeV and its recoil mass between 120 GeV and 150 GeV. Additional selections based on the kinematic variables of the electron-positron

system, the polar angles and the energies of the selected electron and positron, are applied. Events from  $e^+e^- \rightarrow e^+e^-(\gamma)$ ,  $e^+\nu W^-(e^-\bar{\nu}W^+)$ ,  $e^+e^-Z$  production are the dominant backgrounds after the selection. The recoil mass distribution of the selected events is shown in Fig. 11(b).

Event selections independent of Higgs boson decays are essential for the model-independent measurement of  $\sigma(ZH)$ . Additional selections using the Higgs boson decay information can, however, be applied to improve the Higgs boson mass measurement. This will be particularly effective in suppressing the large backgrounds from Bhabha scattering and single  $W$  or  $Z$  boson production for the analysis of the  $Z \rightarrow e^+e^-$  decay. This improvement is not implemented in the current study.

#### 4.2 $Z \rightarrow q\bar{q}$

The recoil mass technique can also be applied to the hadronic  $Z$  boson decays ( $Z \rightarrow q\bar{q}$ ) of the  $e^+e^- \rightarrow ZX$  candidates. This analysis benefits from a larger  $Z \rightarrow q\bar{q}$  decay branching ratio, but suffers from the fact that jet energy resolution is worse than the track momentum and electromagnetic energy resolutions. In addition, ambiguity in selecting jets from the  $Z \rightarrow q\bar{q}$  decay, particularly in events with hadronic decays of the Higgs boson, can degrade the analysis performance and also introduce model-dependence to the analysis. Therefore, the measurement is highly dependent on the performance of the particle-flow reconstruction and the jet clustering algorithm.

Following the same approach as the ILC study [33], an analysis based on the fast simulation has been performed. After the event selection, main backgrounds arise from  $Z\gamma$ 's and  $WW$  production. Compared with the leptonic decays, the signal-to-background ratio is considerably worse and the recoil mass resolution is significantly poorer.

### 4.3 Measurements of $\sigma(ZH)$ and $m_H$

The inclusive  $e^+e^- \rightarrow ZH$  production cross section  $\sigma(ZH)$  and Higgs boson mass  $m_H$  can be extracted from fits to the recoil mass distributions of the  $e^+e^- \rightarrow Z+X \rightarrow \ell^+\ell^-/q\bar{q}+X$  candidates. For the leptonic  $Z \rightarrow \ell^+\ell^-$  decays, the recoil mass distribution of the signal process  $e^+e^- \rightarrow ZH$  (and  $e^+e^- \rightarrow e^+e^-H$  in case of the  $Z \rightarrow e^+e^-$  decay) is modeled with a Crystal Ball function [34] whereas the total background is modeled with a polynomial function in the fit. As noted above, the recoil mass distribution is insensitive to the intrinsic Higgs boson width if it were as small as predicted by the SM. The Higgs boson mass can be determined with precision of 6.5 MeV and 14 MeV from the  $Z \rightarrow \mu^+\mu^-$  and  $Z \rightarrow e^+e^-$  decay modes, respectively. In combination, an uncertainty of 5.9 MeV can be achieved.  $e^+e^- \rightarrow Z+X \rightarrow q\bar{q}+X$  events contribute little to the precision of the  $m_H$  measurement due to the poor  $Z \rightarrow q\bar{q}$  mass resolution, but dominates the precision of the  $e^+e^- \rightarrow ZH$  cross section measurement benefiting from its large statistics. A relative precision of 0.61% of  $\sigma(ZH)$  is predicted from a simple event counting analysis. In comparison, the corresponding precision from the  $Z \rightarrow e^+e^-$  and  $Z \rightarrow \mu^+\mu^-$  decays is estimated to be 1.4% and 0.9%, respectively. The combined precision of the three measurements is 0.5%. Table 5 summarizes the expected precisions on  $m_H$  and  $\sigma(ZH)$  from a CEPC dataset of  $5.6 \text{ ab}^{-1}$ .

Table 5. Estimated measurement precision for the Higgs boson mass  $m_H$  and the  $e^+e^- \rightarrow ZH$  production cross section  $\sigma(ZH)$  from a CEPC dataset of  $5.6 \text{ ab}^{-1}$ .

$Z$ decay mode	$\Delta m_H$ (MeV)	$\Delta\sigma(ZH)/\sigma(ZH)$
$e^+e^-$	14	1.43%
$\mu^+\mu^-$	6.5	0.86%
$q\bar{q}$	–	0.61%
Combined	5.9	0.5%

## 5 Analyses of Individual Decay Modes

Different decay modes of the Higgs boson can be identified through their unique signatures, leading to the measurements of production rates for these decays. For the  $e^+e^- \rightarrow ZH$  production process in particular, the candidate events can be tagged from the visible decays of the  $Z$  bosons, the Higgs boson decays can then be

probed by studying the rest of the events. These measurements combined with the inclusive  $\sigma(ZH)$  measurement discussed in Section 4 will permit the extraction of the Higgs boson decay branching ratios in a model-independent way.

In this section, the results of the current CEPC simulation studies of many different Higgs boson decay modes are summarized. The studies are based on the CEPC-v1 detector concept and  $e^+e^-$  collisions at  $\sqrt{s} = 250 \text{ GeV}$ . The expected relative precision from a CEPC dataset of  $5.6 \text{ ab}^{-1}$  on the product of the  $ZH$  cross section and the Higgs boson decay branching ratio,  $\sigma(ZH) \times \text{BR}$ , are presented. Detailed discussions of individual analyses are beyond the scope of this paper and therefore only their main features are presented. For the study of a specific Higgs boson decay mode, the other decay modes of the Higgs boson often contribute as well. These contributions are fixed to their SM expectations and are included as backgrounds unless otherwise noted. However for the combination of all decay modes studied, they are allowed to vary within the constraints of the measurements of those decays, see Section 6.

In addition to the invariant and recoil mass, two other mass observables, visible mass and missing mass, are often used in analyses described below. They are defined, respectively, as the invariant mass and recoil mass of all visible particles such as charged leptons, photons and jets, *i.e.* practically all particles other than neutrinos.

### 5.1 $H \rightarrow b\bar{b}/c\bar{c}/gg$

For a SM Higgs boson with a mass of 125 GeV, nearly 70% of all Higgs bosons decay into a pair of jets:  $b$ -quarks (57.7%),  $c$ -quarks (2.9%) and gluons (8.6%). While the  $H \rightarrow b\bar{b}$  decay has recently been observed at the LHC [35, 36], the  $H \rightarrow c\bar{c}$  and  $H \rightarrow gg$  decays are difficult, if not impossible, to be identified there due to large backgrounds. In comparison, all these three decays can be isolated and studied at the CEPC. The  $H \rightarrow c\bar{c}$  decay is likely the only process for studying Higgs boson coupling to the second-generation quarks at collider experiments. The identifications of  $H \rightarrow b\bar{b}/c\bar{c}/gg$  decays pose critical challenges to the CEPC detector performance, particularly its ability to tag  $b$ - and  $c$ -quark jets from light-flavored jets ( $u, d, s, g$ ). Thus they are good benchmarks for the design and optimization of the jet flavor tagging performance of the CEPC detector.

Studies are performed in details for  $e^+e^- \rightarrow ZH$  production with the leptonic decays of the  $Z$  bosons. The contribution from the  $Z$ -fusion process of  $e^+e^- \rightarrow e^+e^-H$  is included in the  $e^+e^- \rightarrow ZH \rightarrow e^+e^-H$  study. The analysis is based on full simulation for the Higgs boson signal samples and fast simulation for the  $\ell^+\ell^-q\bar{q}$  background samples. After selecting two leading leptons with opposite charge, the rest of the reconstructed particles are

clustered into two jets to form a hadronically decaying Higgs boson candidate, whose invariant mass is required to be between 75 GeV and 150 GeV. The dilepton invariant mass is required to be within 70–110 GeV for the  $e^+e^-$  channel and 81–101 GeV for the  $\mu^+\mu^-$  channel. Moreover, the dilepton system must have its transverse momentum in the range 10–90 GeV and its recoil mass between 120 GeV and 150 GeV. In addition, a requirement on the polar angle of the Higgs boson candidate,  $|\cos\theta_H| < 0.8$ , is applied.

In order to identify the flavors of the two jets of the Higgs boson candidate, variables  $L_B$  and  $L_C$  are constructed using information such as those from LCFIPlus jet flavor tagging algorithm. The values of  $L_B$  ( $L_C$ ) are close to one if both jets are originated from  $b(c)$  quarks and are close to zero if both have light-quark or gluon origins. An unbinned maximum likelihood fit to the  $M_{\text{recoil}}$ ,  $L_B$  and  $L_C$  distributions of candidate events is used to extract the individual signal yields of the  $H \rightarrow b\bar{b}$ ,  $H \rightarrow c\bar{c}$  and  $H \rightarrow gg$  decay modes. The total probability density function (PDF) is the sum of signal and background components. For signals, their  $M_{\text{recoil}}$  PDFs are modeled by Crystal Ball functions [34] with small exponential tails. The background PDF is taken as a sum of two components: a background from Higgs boson decays to other final states such as  $WW$  and  $ZZ$ , and a combinatorial background from other sources, dominated by the  $e^+e^- \rightarrow ZZ \rightarrow \ell\ell q\bar{q}$  production. The background from other Higgs boson decay channels has the same  $M_{\text{recoil}}$  PDF as the signals. The  $M_{\text{recoil}}$  distribution of the combinatorial background is modeled by a second order polynomial. The PDFs of the signal  $L_B$  and  $L_C$  distributions are described by two dimensional histograms, taken from the MC simulated events. The  $L_B$  and  $L_C$  distributions of both background components are modeled by 2-dimensional histogram PDFs based on the MC simulation. The dilepton recoil mass distributions of the simulated data and the fit results are shown in Fig. 12(a,b). The estimated relative statistical precision of the measurements of  $\sigma(ZH) \times \text{BR}(H \rightarrow b\bar{b}/c\bar{c}/gg)$  are listed in Table 6.

Table 6 also includes the results of the  $Z \rightarrow \nu\bar{\nu}$  and  $Z \rightarrow q\bar{q}$  decays. For the  $Z \rightarrow q\bar{q}$  final state, events are clustered into four jets and the mass information of jet pairs are used to select the Higgs and  $Z$  boson candidates. In addition to  $ZZ$ ,  $WW$  is also a major background for this analysis, particularly for the  $H \rightarrow c\bar{c}$  and  $H \rightarrow gg$  decays. As for the  $Z \rightarrow \nu\bar{\nu}$  final state, events are clustered into two jets to form the Higgs boson candidate, the invisibly decaying  $Z$  boson is inferred from the missing mass of the event. Fits similar to the one used in the analysis of the  $Z \rightarrow \ell^+\ell^-$  channel is subsequently performed to statistically separate the  $H \rightarrow b\bar{b}$ ,  $c\bar{c}$  and  $gg$  decay components. The simulated data and the fitted

dijet mass distributions of the Higgs boson candidates are shown in Fig. 12(c,d) for  $Z \rightarrow q\bar{q}$  and  $Z \rightarrow \nu\bar{\nu}$ .

Combining all  $Z$  boson decay modes studied, a relative statistical precision for  $\sigma(ZH) \times \text{BR}$  of 0.3%, 3.3% and 1.3% can be achieved for the  $H \rightarrow b\bar{b}$ ,  $c\bar{c}$  and  $gg$  decays, respectively.

Table 6. Expected relative precision on  $\sigma(ZH) \times \text{BR}$  for the  $H \rightarrow b\bar{b}$ ,  $c\bar{c}$  and  $gg$  decays from a CEPC dataset of  $5.6 \text{ ab}^{-1}$ .

$Z$ decay mode	$H \rightarrow b\bar{b}$	$H \rightarrow c\bar{c}$	$H \rightarrow gg$
$Z \rightarrow e^+e^-$	1.3%	12.8%	6.8%
$Z \rightarrow \mu^+\mu^-$	1.0%	9.4%	4.9%
$Z \rightarrow q\bar{q}$	0.5%	10.6%	3.5%
$Z \rightarrow \nu\bar{\nu}$	0.4%	3.7%	1.4%
Combined	0.3%	3.1%	1.2%

## 5.2 $H \rightarrow WW^*$

For a 125 GeV SM Higgs boson, the  $H \rightarrow WW^*$  decay has the second largest branching ratio at 21.5% [37]. The sensitivity of the  $\sigma(ZH) \times \text{BR}(H \rightarrow WW^*)$  measurement is estimated by combining results from the studies of a few selected final states (Table 7) of the  $H \rightarrow WW^*$  decay of  $ZH$  production. SM diboson production is the main background source in all cases.

For  $Z \rightarrow \ell^+\ell^-$ , the  $H \rightarrow WW^*$  decay final states studied are  $\ell\nu\ell'\nu$  and  $\ell\nu q\bar{q}$ . The  $ZH$  candidate events are selected by requiring the dilepton invariant mass in the range of 80–100 GeV and their recoil mass in 120–150 GeV. For  $Z \rightarrow \nu\bar{\nu}$ , the  $\ell\nu q\bar{q}$  and  $q\bar{q}q\bar{q}$  final states are considered for the  $H \rightarrow WW^*$  decay. The presence of neutrinos results in events with large missing mass, which is required to be in the range of 75–140 (75–150) GeV for the  $\ell\nu q\bar{q}$  ( $q\bar{q}q\bar{q}$ ) final state. The total visible mass of the event must be in the range of 100–150 GeV for both  $\ell\nu q\bar{q}$  and  $q\bar{q}q\bar{q}$  final states. In addition, the total transverse momentum of the visible particles must be in the range of 20–80 GeV. Additional requirements are applied to improve the signal-background separations. For  $Z \rightarrow q\bar{q}$ , the  $H \rightarrow WW^* \rightarrow q\bar{q}q\bar{q}$  decay is studied. Candidate events are reconstructed into 6 jets. Jets from  $Z \rightarrow q\bar{q}$ ,  $W \rightarrow q\bar{q}$  and  $H \rightarrow WW^* \rightarrow q\bar{q}q\bar{q}$  decays are selected by minimizing the  $\chi^2$  of their mass differences to the masses of  $Z$ ,  $W$  and  $H$  boson. Figure 13 shows the visible and missing mass distributions after the selection of the  $Z \rightarrow \nu\bar{\nu}$  and  $H \rightarrow WW^* \rightarrow q\bar{q}q\bar{q}$  final state.

The relative precision on  $\sigma(ZH) \times \text{BR}(H \rightarrow WW^*)$  from the decay final states studied are summarized in Table 7. The combination of these decay final states leads to a precision of 0.9%. This is likely a conservative estimate of the precision as many of the final states of the  $H \rightarrow WW^*$  decay remain to be explored. Including these missing final states will no doubt improve the precision.

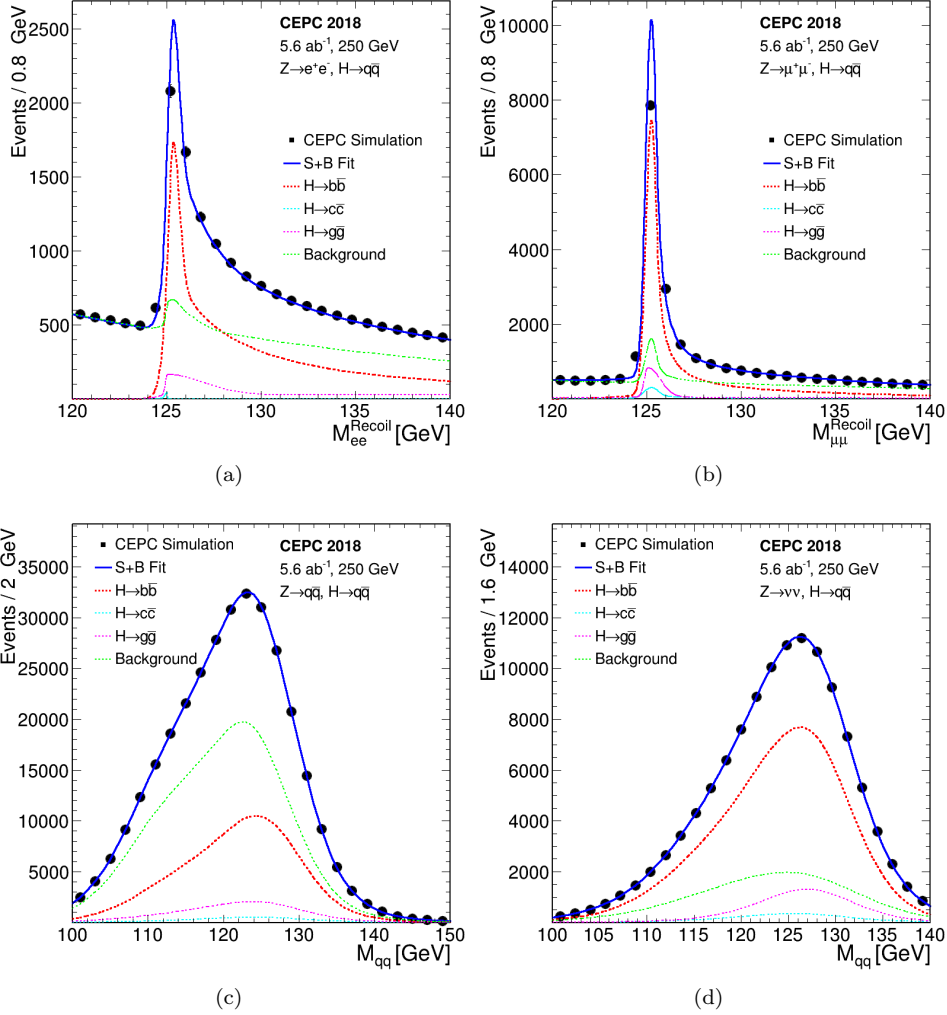


Fig. 12.  $ZH$  production with  $H \rightarrow b\bar{b}/c\bar{c}/g\bar{g}$ : the recoil mass distributions of (a)  $Z \rightarrow e^+e^-$  and (b)  $Z \rightarrow \mu^+\mu^-$ ; the dijet mass distributions of Higgs boson candidates for (c)  $Z \rightarrow q\bar{q}$  and (d)  $Z \rightarrow \nu\bar{\nu}$ . The markers and their uncertainties represent expectations from a CEPC dataset of  $5.6 \text{ ab}^{-1}$  whereas the solid blue curves are the fit results. The dashed curves are the signal and background components. Contributions from other decays of the Higgs boson are included in the background.

Table 7. Expected relative precision on the  $\sigma(ZH) \times \text{BR}(H \rightarrow WW^*)$  measurement from a CEPC dataset of  $5.6 \text{ ab}^{-1}$ .

$ZH$ final state		Precision
$Z \rightarrow e^+e^-$	$H \rightarrow WW^* \rightarrow \ell\nu\ell'\nu, \ell\nu q\bar{q}$	2.6%
$Z \rightarrow \mu^+\mu^-$	$H \rightarrow WW^* \rightarrow \ell\nu\ell'\nu, \ell\nu q\bar{q}$	2.4%
$Z \rightarrow \nu\bar{\nu}$	$H \rightarrow WW^* \rightarrow \ell\nu q\bar{q}, q\bar{q}q\bar{q}$	1.5%
$Z \rightarrow q\bar{q}$	$H \rightarrow WW^* \rightarrow q\bar{q}q\bar{q}$	1.7%
Combined		0.9%

### 5.3 $H \rightarrow ZZ^*$

The  $H \rightarrow ZZ^*$  decay has a branching ratio 2.64% [37] for a 125 GeV Higgs boson in the SM. Events from

$e^+e^- \rightarrow ZH$  production with the  $H \rightarrow ZZ^*$  decay have three  $Z$  bosons in their final states with one of them being off-shell.  $Z$  bosons can decay to all lepton and quark flavors, with the exception of the top quark. Consequently, the  $e^+e^- \rightarrow ZH \rightarrow ZZZ^*$  process has a very rich variety of topologies.

Studies are performed for a few selected  $ZH$  final states:  $Z \rightarrow \mu^+\mu^-$  and  $H \rightarrow ZZ^* \rightarrow \nu\bar{\nu}q\bar{q}$ ;  $Z \rightarrow \nu\bar{\nu}$  and  $H \rightarrow ZZ^* \rightarrow \ell^+\ell^-q\bar{q}$ . The  $W$  and  $Z$  boson fusion processes,  $e^+e^- \rightarrow e^+e^-H$  and  $e^+e^- \rightarrow \nu\bar{\nu}H$ , are included in the  $Z(e^+e^-)H$  and  $Z(\nu\bar{\nu})H$  studies assuming their SM values for the rates. For the final states studied, the SM  $ZZ$  production is the main background.

For  $Z \rightarrow \mu^+\mu^-$  and  $H \rightarrow ZZ^* \rightarrow \nu\bar{\nu}q\bar{q}$ , the muon pairs must have their invariant masses between 80–100 GeV,

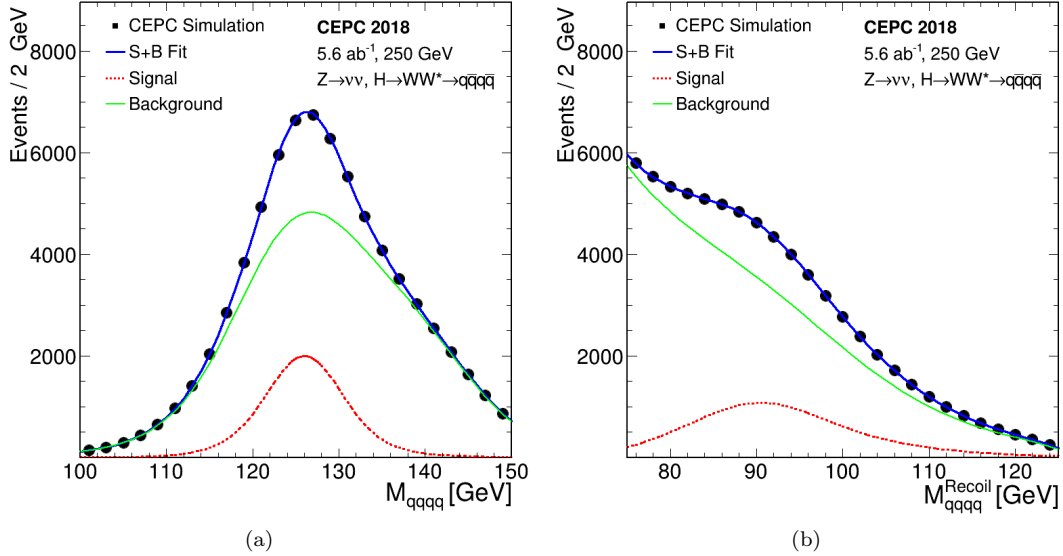


Fig. 13.  $ZH$  production with  $Z \rightarrow \nu\bar{\nu}$  and  $H \rightarrow WW^* \rightarrow q\bar{q}q\bar{q}$ : distributions of (a) the visible mass and (b) the missing mass of selected events. The markers and their uncertainties represent expectations from a CEPC dataset of  $5.6\text{ab}^{-1}$  whereas the solid blue curves are the fit results. The dashed curves are the signal and background components. Contributions from other decays of the Higgs boson are included in the background.

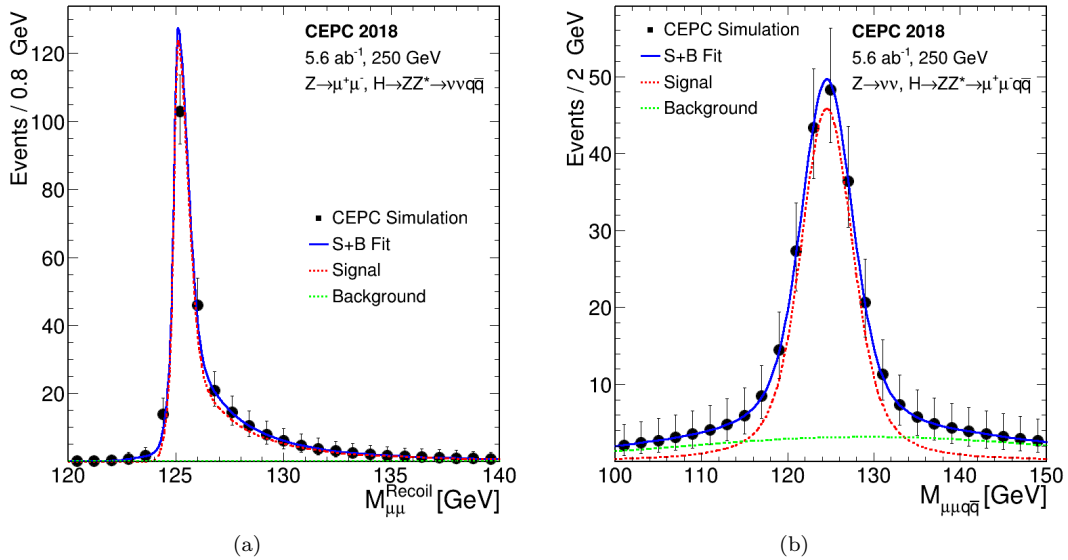


Fig. 14.  $ZH$  production with  $H \rightarrow ZZ^*$ : a) the recoil mass distribution of the  $\mu^+\mu^-$  system for  $Z \rightarrow \mu^+\mu^-$ ,  $H \rightarrow ZZ^* \rightarrow \nu\bar{\nu}q\bar{q}$ ; b) the invariant mass distribution of the  $\mu^+\mu^-q\bar{q}$  system for  $Z \rightarrow \nu\bar{\nu}$ ,  $H \rightarrow ZZ^* \rightarrow \mu^+\mu^-q\bar{q}$ . The markers and their uncertainties represent expectations from a CEPC dataset of  $5.6\text{ab}^{-1}$  whereas the solid blue curves are the fit results. The dashed curves are the signal and background components. Contributions from other decays of the Higgs boson are included in the background.

recoil masses between 120–160 GeV and transverse momenta larger than 10 GeV. The jet pairs are required to have their invariant masses in the range of 10–38 GeV. Figure 14(a) shows the recoil mass distribution of  $Z \rightarrow \mu^+\mu^-$  after the selection. The background is negligible

in this final state.

The candidates of  $Z \rightarrow \nu\bar{\nu}$  and  $H \rightarrow ZZ^* \rightarrow \ell^+\ell^-q\bar{q}$  are selected by requiring a same-flavor lepton pair and two jets. The total visible energy must be smaller than 180 GeV and the missing mass in the range of 58–

138 GeV. Additional requirements are applied on the mass and transverse momenta of the lepton and jet pairs. After the selection, the background is about an order of magnitude smaller than the signal as shown in Fig. 14(b).

Table 8. Expected relative precision for the  $\sigma(ZH) \times \text{BR}(H \rightarrow ZZ^*)$  measurement with an integrated luminosity  $5.6 \text{ ab}^{-1}$ .

$ZH$ final state		Precision
$Z \rightarrow \mu^+ \mu^-$	$H \rightarrow ZZ^* \rightarrow \nu\bar{\nu} q\bar{q}$	7.2%
$Z \rightarrow \nu\bar{\nu}$	$H \rightarrow ZZ^* \rightarrow \ell^+ \ell^- q\bar{q}$	7.9%
Combined		4.9%

Table 8 summarizes the expected precision on  $\sigma(ZH) \times \text{BR}(H \rightarrow ZZ^*)$  from the final states considered. The combination of these final states results in a precision of about 4.9%. The sensitivity can be significantly improved considering that many final states are not included in the current study. In particular, the final state of  $Z \rightarrow q\bar{q}$  and  $H \rightarrow ZZ^* \rightarrow q\bar{q}q\bar{q}$  which represents a third of all  $ZH \rightarrow ZZZ^*$  decay is not studied. Moreover, gain can also be made using multivariate techniques.

#### 5.4 $H \rightarrow \gamma\gamma$

The diphoton decay of a 125 GeV Higgs boson has a small branching ratio of 0.23% in the SM due to its origin involving massive  $W$  boson and top quark in loops. However photons can be identified and measured well, thus the decay can be fully reconstructed with a good precision. The decay also serves as a good benchmark for the performance of the electromagnetic calorimeter.

Studies are performed for the  $ZH$  production with  $H \rightarrow \gamma\gamma$  and four different  $Z$  boson decay modes:  $Z \rightarrow \mu^+ \mu^-$ ,  $\tau^+ \tau^-$ ,  $\nu\bar{\nu}$  and  $q\bar{q}$ . The  $Z \rightarrow e^+ e^-$  decay is not considered because of the expected large background from the Bhabha process. The studies are based on the full detector simulation for the  $Z \rightarrow q\bar{q}$  decay channel and the fast simulation for the rest. Photon candidates are required to have energies greater than 25 GeV and polar angles of  $|\cos\theta| < 0.9$ . The photon pair with the highest invariant mass is retained as the  $H \rightarrow \gamma\gamma$  candidate and its recoil mass must be consistent with the  $Z$  boson mass. For the  $Z \rightarrow \mu^+ \mu^-$  and  $Z \rightarrow \tau^+ \tau^-$  decays, a minimal angle of  $8^\circ$  between any selected photon and lepton is required to suppress backgrounds from final state radiations. After the selection, the main SM background is the  $e^+ e^- \rightarrow (Z/\gamma^*) \gamma\gamma$  process where the  $\gamma$ 's arise from the initial or final state radiations.

The diphoton mass is used as the final discriminant for the separation of signal and backgrounds. The distribution for the  $Z \rightarrow \nu\bar{\nu}$  decay mode is shown in Fig. 15. A relative precision of 6.2% on  $\sigma(ZH) \times \text{BR}(H \rightarrow \gamma\gamma)$  can be achieved.

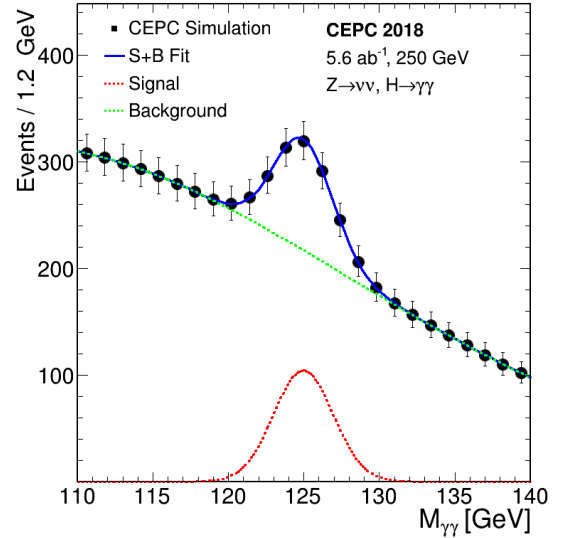


Fig. 15.  $ZH$  production with  $H \rightarrow \gamma\gamma$ : the diphoton invariant mass distribution for the  $Z \rightarrow \nu\bar{\nu}$  decay. The markers and their uncertainties represent expectations from a CEPC dataset of  $5.6 \text{ ab}^{-1}$  whereas the solid blue curve is the fit result. The dashed curves are the signal and background components.

#### 5.5 $H \rightarrow Z\gamma$

Similar to the  $H \rightarrow \gamma\gamma$  decay, the  $H \rightarrow Z\gamma$  decay in the SM is mediated by  $W$  boson and top quark in loops and has a branching ratio of 0.154%. The  $H \rightarrow Z\gamma$  analysis targets the signal process of  $ZH \rightarrow ZZ\gamma \rightarrow \nu\bar{\nu} q\bar{q}\gamma$ , in which one of the  $Z$  bosons decays into a pair of quarks and the other decays into a pair of neutrinos.

The candidate events are selected by requiring exactly one photon with transverse energy between 20–50 GeV and at least two jets, each with transverse energy greater than 10 GeV. The dijet invariant mass and the event missing mass must be within windows of  $\pm 12$  GeV and  $\pm 15$  GeV of the  $Z$  boson mass, respectively. Additional requirements are applied on the numbers of tracks and calorimeter clusters as well as on the transverse and longitudinal momenta of the  $Z$  boson candidates. The backgrounds are dominated by the processes of single boson, diboson,  $q\bar{q}$ , and Bhabha production.

After the event selection, the photon is paired with each of the two  $Z$  boson candidates to form Higgs boson candidates and the mass differences,  $\Delta M = M_{q\bar{q}\gamma} - M_{q\bar{q}}$  and  $\Delta M = M_{\nu\bar{\nu}\gamma} - M_{\nu\bar{\nu}}$ , are calculated. Here the energy and momentum of the  $\nu\bar{\nu}$  system are taken to be the missing energy and momentum of the event. For signal events, one of the mass differences is expected to populate around  $M_H - M_Z \sim 35$  GeV whereas the other should be part of the continuum background. Figure 16 shows the  $\Delta M$  distribution expected from an integrated luminosity of  $5.6 \text{ ab}^{-1}$ . Modeling the signal distribution of

the correct pairing with a Gaussian and the background (including wrong-pairing contribution of signal events) with a polynomial, a likelihood fit results in a relative precision of 13% on  $\sigma(ZH) \times \text{BR}(H \rightarrow Z\gamma)$ .

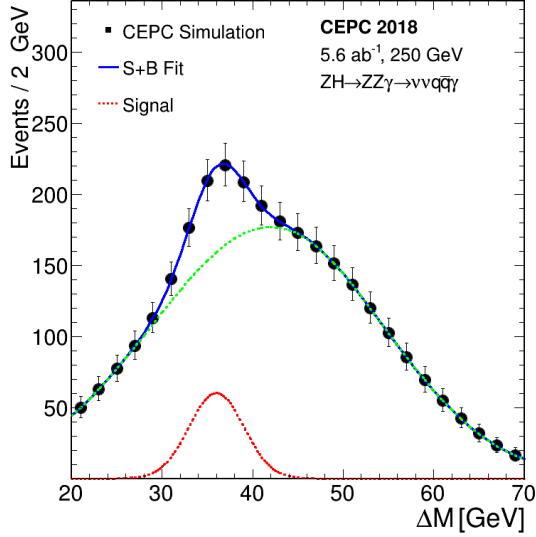


Fig. 16. The distribution of the mass difference  $\Delta M$  ( $M_{q\bar{q}\gamma} - M_{q\bar{q}}$  or  $M_{\nu\bar{\nu}\gamma} - M_{\nu\bar{\nu}}$ ) of the selected  $e^+e^- \rightarrow ZH \rightarrow ZZ\gamma \rightarrow \nu\bar{\nu}q\bar{q}\gamma$  candidates expected from an integrated luminosity of  $5.6\text{ab}^{-1}$ . The signal distribution shown is for the correct pairings of the Higgs boson decays.

This analysis can be improved with additional optimizations and using multivariate techniques. Other decay modes such as  $ZH \rightarrow ZZ\gamma \rightarrow q\bar{q}q\bar{q}\gamma$  should further improve the precision on the  $\sigma(ZH) \times \text{BR}(H \rightarrow Z\gamma)$  measurement.

### 5.6 $H \rightarrow \tau^+\tau^-$

The  $H \rightarrow \tau^+\tau^-$  decay has a branching ratio of 6.32% at  $m_H = 125$  GeV in the SM. The  $\tau$ -lepton is short-lived and decays to one or three charged pions along with a number of neutral pions. The charged and neutral pions, as well as the two photons from the decay of the latter, can be well resolved and measured by the CEPC detector.

Simulation studies are performed for  $e^+e^- \rightarrow ZH$  production with  $H \rightarrow \tau^+\tau^-$  and  $Z \rightarrow \mu^+\mu^-, \nu\bar{\nu}$  and  $q\bar{q}$  decays. For  $Z \rightarrow \mu^+\mu^-$ , candidates are first required to have a pair of oppositely charged muons with their invariant mass between 40–180 GeV and their recoil mass between 110–180 GeV. For  $Z \rightarrow \nu\bar{\nu}$ , candidates are preselected by requiring a missing mass in the range of 65–225 GeV, a visible mass greater than 50 GeV and an event visible transverse momentum between 10–100 GeV. For both decays, a BDT selection is applied after the preselection to identify di-tau candidates. The BDT utilizes information such as numbers of tracks and photons

and the angles between them. After these selections, the  $ZH$  production with the non-tau decays of the Higgs boson is the dominant ( $> 95\%$ ) background for  $Z \rightarrow \mu^+\mu^-$  and contributes to approximately 40% of the total background for  $Z \rightarrow \nu\bar{\nu}$ . The rest of the background in the  $Z \rightarrow \nu\bar{\nu}$  channel comes from diboson production. For  $Z \rightarrow q\bar{q}$ , candidates are required to have a pair of tau candidates with their invariant mass between 20–120 GeV, a pair of jets with their mass between 70–110 GeV and their recoil mass between 100–170 GeV. The main background is again from  $ZH$  production originating from the decay modes other than the intended  $ZH \rightarrow q\bar{q}\tau^+\tau^-$  decay. The rest of the background is primarily from  $ZZ$  production.

The final signal yields are extracted from fits to the distributions of variables based on the impact parameters of the leading tracks of the two tau candidates as shown in Fig. 17. Table 9 summarizes the estimated precision on  $\sigma(ZH) \times \text{BR}(H \rightarrow \tau^+\tau^-)$  expected from a CEPC dataset of  $5.6\text{ab}^{-1}$  for the three  $Z$  boson decay modes studied. The precision from the  $Z \rightarrow e^+e^-$  decay mode extrapolated from the  $Z \rightarrow \mu^+\mu^-$  study is also included. The  $e^+e^- \rightarrow e^+e^-H$  contribution from the  $Z$  fusion process is fixed to its SM value in the extrapolation. In combination, the relative precision of 0.8% is expected for  $\sigma(ZH) \times \text{BR}(H \rightarrow \tau^+\tau^-)$ .

Table 9. Expected relative precision for the  $\sigma(ZH) \times \text{BR}(H \rightarrow \tau^+\tau^-)$  measurement from a CEPC dataset of  $5.6\text{ab}^{-1}$ .

$ZH$ final state	Precision
$Z \rightarrow \mu^+\mu^- \quad H \rightarrow \tau^+\tau^-$	2.6%
$Z \rightarrow e^+e^- \quad H \rightarrow \tau^+\tau^-$	2.6%
$Z \rightarrow \nu\bar{\nu} \quad H \rightarrow \tau^+\tau^-$	2.5%
$Z \rightarrow q\bar{q} \quad H \rightarrow \tau^+\tau^-$	0.9%
Combined	0.8%

The  $ZH$  production with  $Z \rightarrow \ell^+\ell^-, q\bar{q}$  and  $H \rightarrow \tau^+\tau^-$  can also be used to extract the  $CP$  property of the Higgs boson [38]. Using the three tau decay modes with the largest branching ratios ( $\pi^\pm\nu$ ,  $\pi^\pm\pi^0\nu$  and  $\ell\nu\nu$ ), the neutrinos from the tau decay are reconstructed from the mass, energy and impact parameter constraints. A matrix element based method is employed to extract the value of the  $CP$  mixing angle between the even and odd components of the  $H\tau\tau$  coupling. It is estimated that with  $5.6\text{ab}^{-1}$  of the CEPC data, a precision of  $2.9^\circ$  can be achieved for this angle, which can shed light on the potential BSM physics.

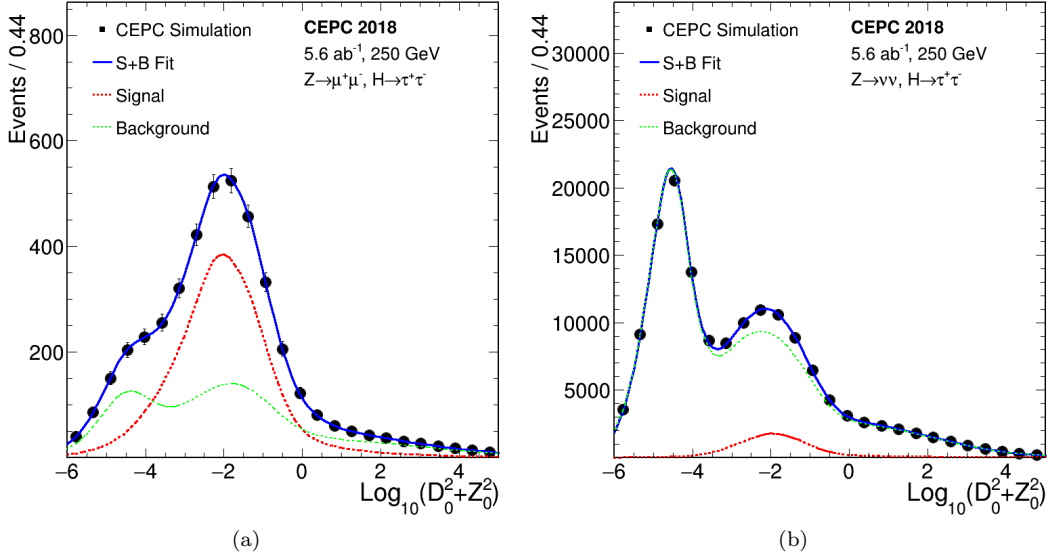


Fig. 17. Distributions of the impact parameter variable of the leading tracks from the two tau candidates in the  $Z$  decay mode: (a)  $Z \rightarrow \mu^+ \mu^-$  and (b)  $Z \rightarrow \nu \bar{\nu}$ . The markers and their uncertainties represent expectations from a CEPC dataset of  $5.6 \text{ ab}^{-1}$  whereas the solid blue curves are the fit results. The dashed curves are the signal and background components. Contributions from other decays of the Higgs boson are included in the background.

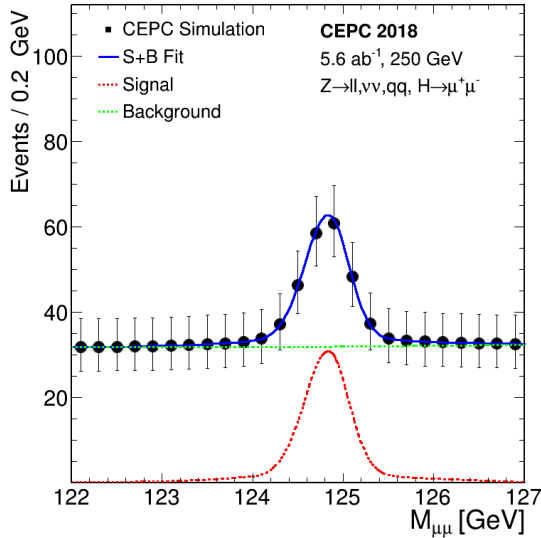


Fig. 18.  $ZH$  production with the  $H \rightarrow \mu^+ \mu^-$  decay: dimuon invariant mass distribution of the selected  $H \rightarrow \mu^+ \mu^-$  candidates expected from an integrated luminosity of  $5.6 \text{ ab}^{-1}$  at the CEPC. The distribution combines contributions from  $Z \rightarrow \ell^+ \ell^-$ ,  $Z \rightarrow \nu \bar{\nu}$ , and  $Z \rightarrow q \bar{q}$  decays. The markers and their uncertainties represent expectations whereas the solid curve is the fit result. The dashed curves are the signal and background components.

### 5.7 $H \rightarrow \mu^+ \mu^-$

The dimuon decay of the Higgs boson,  $H \rightarrow \mu^+ \mu^-$ , is sensitive to the Higgs boson coupling to the second-

generation fermions with a clean final-state signature. In the SM, the branching ratio of the decay is  $2.18 \times 10^{-4}$  [37] for  $m_H = 125$  GeV.

To estimate CEPC's sensitivity for the  $H \rightarrow \mu^+ \mu^-$  decay, studies are performed for the  $ZH$  production with the  $Z$  decay modes:  $Z \rightarrow \ell^+ \ell^-$ ,  $Z \rightarrow \nu \bar{\nu}$ , and  $Z \rightarrow q \bar{q}$ . In all cases, the SM production of  $ZZ$  is the dominant background source. Candidate events are selected by requiring a pair of muons with its mass between 120–130 GeV and their recoiling mass consistent with the  $Z$  boson mass (in the approximate range of 90–93 GeV, depending on the decay mode). Additional requirements are applied to identify specific  $Z$  boson decay modes. For  $Z \rightarrow \ell^+ \ell^-$ , candidate events must have another lepton pair with its mass consistent with  $m_Z$ . In the case of  $Z \rightarrow \mu^+ \mu^-$ , the muon pairs of the  $Z \rightarrow \mu^+ \mu^-$  and  $H \rightarrow \mu^+ \mu^-$  decays are selected by minimizing a  $\chi^2$  based on their mass differences with  $m_Z$  and  $m_H$ . For the  $Z \rightarrow \nu \bar{\nu}$  decay, a requirement on the missing energy is applied. For the  $Z \rightarrow q \bar{q}$  decay, candidate events must have two jets with their mass consistent with  $m_Z$ . To further reduce the  $ZZ$  background, differences between the signal and background in kinematic variables, such as the polar angle, transverse momentum and energy of the candidate  $H \rightarrow \mu^+ \mu^-$  muon pair, are exploited. Simple criteria on these variables are applied for the  $Z \rightarrow \ell^+ \ell^-$  and  $Z \rightarrow \nu \bar{\nu}$  decay mode whereas a BDT is used for the  $Z \rightarrow q \bar{q}$  decay.

In all analyses, the signal is extracted through unbinned likelihood fits to the  $M_{\mu^+ \mu^-}$  distributions in the

range of 120–130 GeV with a signal-plus-background model. Analytical functions are used model both the signal and background distributions. The signal model is a Crystal Ball function while the background model is described by a second-order Chebyshev polynomial. The dimuon mass distribution combining all  $Z$  boson decay modes studied is shown in Fig. 18 with the result of the signal-plus-background fit overlaid. The combined relative precision on the  $\sigma(ZH) \times \text{BR}(H \rightarrow \mu^+ \mu^-)$  measurement is estimated to be about 16% for  $5.6 \text{ ab}^{-1}$  integrated luminosity.

### 5.8 The invisible decay of the Higgs boson: $H \rightarrow \text{inv}$

In the SM, the Higgs boson can decay invisibly via  $H \rightarrow ZZ^* \rightarrow \nu\bar{\nu}\nu\bar{\nu}$ . For a Higgs boson mass of 125 GeV, this decay has a branching ratio of  $1.06 \times 10^{-3}$ . In many extensions to the SM, the Higgs boson can decay directly to invisible particles [39–42]. In this case, the branching ratio can be significantly enhanced.

The sensitivity of the  $\text{BR}(H \rightarrow \text{inv})$  measurement is studied for the  $Z \rightarrow \ell^+ \ell^-$  and  $Z \rightarrow q\bar{q}$  decay modes. The  $H \rightarrow ZZ^* \rightarrow \nu\bar{\nu}\nu\bar{\nu}$  decay is used to model the  $H \rightarrow \text{inv}$  decay in both the SM and its extensions. This is made possible by the fact that the Higgs boson is narrow scalar so that the production and the decay are factorized. The main background is SM  $ZZ$  production with one of the  $Z$  bosons decay invisibly and the other decays visibly. Candidate events in the  $Z \rightarrow \ell^+ \ell^-$  decay mode are selected by requiring a pair of lepton with its mass between 70–100 GeV and event visible energy in the range 90–120 GeV. Similarly, candidate events in  $Z \rightarrow q\bar{q}$  are selected by requiring two jets with its mass between 80–105 GeV and event visible energy in the range 90–130 GeV. Additional selections including using a BDT to exploit the kinematic differences between signal and background events are applied.

Table 10. Expected relative precision on  $\sigma(ZH) \times \text{BR}(H \rightarrow \text{inv})$  and 95% CL upper limit on  $\text{BR}(H \rightarrow \text{inv})$  from a CEPC dataset of  $5.6 \text{ ab}^{-1}$ .

$ZH$ final state studied	Relative precision on $\sigma \times \text{BR}$	Upper limit on $\text{BR}(H \rightarrow \text{inv})$
$Z \rightarrow e^+ e^-$ $H \rightarrow \text{inv}$	339%	0.82%
$Z \rightarrow \mu^+ \mu^-$ $H \rightarrow \text{inv}$	232%	0.60%
$Z \rightarrow q\bar{q}$ $H \rightarrow \text{inv}$	217%	0.57%
Combined	143%	0.41%

Table 10 summarizes the expected precision on the measurement of  $\sigma(ZH) \times \text{BR}(H \rightarrow \text{inv})$  and the 95% confidence-level (CL) upper limit on  $\text{BR}(H \rightarrow \text{inv})$  from a CEPC dataset of  $5.6 \text{ ab}^{-1}$ . Subtracting the SM  $H \rightarrow ZZ^* \rightarrow \nu\bar{\nu}\nu\bar{\nu}$  contribution, a 95% CL upper limit of 0.30% on  $\text{BR}_{\text{inv}}^{\text{BSM}}$ , the BSM contribution the  $H \rightarrow \text{inv}$  decay can be obtained.

### 5.9 Measurement of $\sigma(e^+ e^- \rightarrow \nu_e \bar{\nu}_e H) \times \text{BR}(H \rightarrow b\bar{b})$

The  $W$ -fusion  $e^+ e^- \rightarrow \nu_e \bar{\nu}_e H$  process has a cross section of 3.3% of that of the  $ZH$  process at  $\sqrt{s} = 250$  GeV. The product of its cross section and  $\text{BR}(H \rightarrow b\bar{b})$ ,  $\sigma(\nu\bar{\nu}H) \times \text{BR}(H \rightarrow b\bar{b})$ , is a key input quantity to one of the two model-independent methods for determining the Higgs boson width at the CEPC, see Section 6. The  $e^+ e^- \rightarrow \nu\bar{\nu}H \rightarrow \nu\bar{\nu}b\bar{b}$  process has the same final state as the  $e^+ e^- \rightarrow ZH \rightarrow \nu\bar{\nu}b\bar{b}$  process, but has a rate that is approximately one sixth of  $e^+ e^- \rightarrow ZH \rightarrow \nu\bar{\nu}b\bar{b}$  at  $\sqrt{s} = 250$  GeV. The main non-Higgs boson background is the SM  $ZZ$  production.

The  $Z(\nu\bar{\nu})H$  background is irreducible and can also interfere with  $\nu\bar{\nu}H$  in the case of  $Z \rightarrow \nu_e \bar{\nu}_e$ . However the interference effect is expected to be small and is therefore not taken into account in the current study. The  $\nu\bar{\nu}H$  and  $Z(\nu\bar{\nu})H$  contributions can be separated through the exploration of their kinematic differences. While the invariant mass distributions of the two  $b$ -quark jets are expected to be indistinguishable, the recoil mass distribution should exhibit a resonance structure at the  $Z$  boson mass for  $Z(\nu\bar{\nu})H$  and show a continuum spectrum for  $\nu\bar{\nu}H$ . Furthermore, Higgs bosons are produced with different polar angular distributions, see Fig. 19(a).

Candidate events are selected by requiring their visible energies between 105 GeV and 155 GeV, visible masses within 100–135 GeV, and missing masses in the range of 65–135 GeV. The two  $b$ -quark jets are identified using the  $B$ -likeness variable  $L_B$  as discussed in Section 5.1. To separate  $\nu\bar{\nu}H$  and  $Z(\nu\bar{\nu})H$  contributions, a 2-dimensional fit in the plane of the recoil mass and polar angle of the  $b\bar{b}$  system is performed. The recoil mass resolution is improved through a kinematic fit by constraining the invariant mass of the two  $b$ -jets within its resolution to that of the Higgs boson mass. Figure 19(b) shows the recoil mass distribution of the  $b\bar{b}$  system after the kinematic fit. A fit to the  $M_{b\bar{b}} - \cos\theta$  distribution with both rates of  $\nu\bar{\nu}H$  and  $Z(\nu\bar{\nu})H$  processes as free parameters leads to relative precision of 2.9% for  $\sigma(\nu\bar{\nu}H) \times \text{BR}(H \rightarrow b\bar{b})$  and 0.30% for  $\sigma(ZH) \times \text{BR}(H \rightarrow b\bar{b})$ . The latter is consistent with the study of the  $H \rightarrow b\bar{b}/c\bar{c}/g\bar{g}$  decay described in Section 5.1. Fixing the  $Z(\nu\bar{\nu})H(b\bar{b})$  contribution to its SM expectation yields a relative precision of 2.6% on  $\sigma(e^+ e^- \rightarrow \nu_e \bar{\nu}_e H) \times \text{BR}(H \rightarrow b\bar{b})$ .

## 6 Combinations of Individual Measurements

### 6.1 Combined measurements of $\sigma \times \text{BR}$ and BR

With the measurements of inclusive cross section  $\sigma(ZH)$  and the cross sections of individual Higgs boson decay mode  $\sigma(ZH) \times \text{BR}$ , the Higgs boson decay branch-

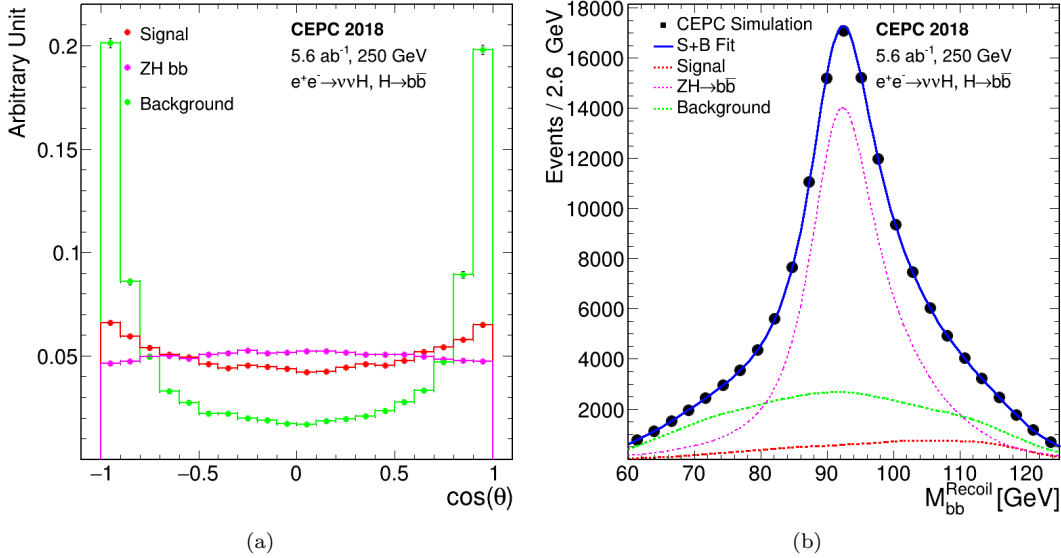


Fig. 19. Distributions of the  $b\bar{b}$  system of the  $e^+e^- \rightarrow \nu\bar{\nu}b\bar{b}$  events: (a) cosine of the polar angle  $\theta$  before the event selection and (b) the recoil mass after the event selection. Contributions from  $e^+e^- \rightarrow \nu_e\bar{\nu}_e H$ ,  $ZH$  and other SM processes are shown. The  $\cos\theta$  distributions are normalized to unity and therefore only shapes are compared.

ing ratio, BR, can be extracted. Most of the systematic uncertainties associated with the measurement of  $\sigma(ZH)$  cancels in this procedure. A maximum likelihood fit is used to estimate the precision on BRs. For a given Higgs boson decay mode, the likelihood has the form:

$$L(\text{BR}, \theta) = \text{Poisson} [N^{\text{obs}} | N^{\text{exp}}(\text{BR}, \theta)] \cdot G(\theta), \quad (3)$$

where BR is the parameter of interest and  $\theta$  represent nuisance parameters associated with systematic uncertainties.  $N^{\text{obs}}$  is the number of the observed events,  $N^{\text{exp}}(\text{BR}, \theta)$  is the expected number of events, and  $G(\theta)$  is a set of constraints on the nuisance parameters within their estimated uncertainties. The number of expected events is the sum of signal and background events. The number of signal events is calculated from the integrated luminosity, the  $e^+e^- \rightarrow ZH$  cross section  $\sigma(ZH)$  measured from the recoil method, Higgs boson branching ratio BR, the event selection efficiency  $\epsilon$ . The number of the expected background events,  $N^b$ , is estimated from Monte Carlo samples. Thus

$$N^{\text{exp}}(\text{BR}, \theta) = \text{Lumi}(\theta^{\text{lumi}}) \times \sigma_{ZH}(\theta^\sigma) \times \text{BR} \times \epsilon(\theta^\epsilon) + N^b(\theta^b), \quad (4)$$

where  $\theta^X$  ( $X = \text{lumi}, \sigma, \epsilon$  and  $b$ ) are the nuisance parameters of their corresponding parameters or measurements. Even with  $10^6$  Higgs boson events, statistical uncertainties are expected to be dominant and thus systematic uncertainties are not taken into account for the current studies. Thus the nuisance parameters are fixed to their nominal values.

For the individual analyses discussed in Section 5, contaminations from Higgs boson production or decays other than the one under study are fixed to their SM values for simplicity. In the combination, however, these constraints are removed and the contaminations are constrained only by the analyses targeted for their measurements. For example, the  $H \rightarrow b\bar{b}/c\bar{c}/g\bar{g}$  analysis suffers from contaminations from the  $H \rightarrow WW^*, ZZ^* \rightarrow q\bar{q}q\bar{q}$  decays. For the analysis discussed in Section 5.1, these contaminations are estimated from SM. In the combination fit, they are constrained by the  $H \rightarrow WW^*$  and  $H \rightarrow ZZ^*$  analyses described in Sections 5.2 and 5.3, respectively. Taking into account these across-channel contaminations properly generally leads to small improvements in precision. For example, the precision on  $\sigma(ZH) \times \text{BR}(H \rightarrow ZZ^*)$  is improved from 5.2% of the standalone analysis to 4.9% from the combination.

Table 11 summarizes the estimated precision of Higgs boson property measurements, combining all studies described in this paper. For the leading Higgs boson decay modes, namely  $b\bar{b}$ ,  $c\bar{c}$ ,  $g\bar{g}$ ,  $WW^*$ ,  $ZZ^*$  and  $\tau^+\tau^-$ , percent level precision are expected. The best achievable statistical uncertainties for  $5.6 \text{ ab}^{-1}$  are 0.26% for  $\sigma(e^+e^- \rightarrow ZH) \times \text{BR}(H \rightarrow b\bar{b})$  and 0.5% for  $\sigma(e^+e^- \rightarrow ZH)$ . Even for these measurements, statistics is likely the dominant source of uncertainties. Systematic uncertainties from the efficiency/acceptance of the detector, the luminosity and the beam energy determination are expected to be small. The integrated luminosity can be measured with a 0.1% precision, a benchmark already achieved at the LEP [43], and can be potentially improved in the

Table 11. Estimated precision of Higgs boson property measurements for the CEPC-v1 detector concept operating at  $\sqrt{s} = 250$  GeV. All precision are relative except for  $m_H$  and  $\text{BR}_{\text{BSM}}(H \rightarrow \text{inv})$  for which  $\Delta m_H$  and 95% CL upper limit are quoted respectively. The extrapolated precision for the CEPC-v4 concept operating at  $\sqrt{s} = 240$  GeV are included for comparisons, see Section 6.2.

Property	Estimated Precision	
	CEPC-v1	CEPC-v4
$m_H$	5.9 MeV	5.9 MeV
$\Gamma_H$	3.1%	3.1%
$\sigma(ZH)$	0.50%	0.50%
$\sigma(\nu\bar{\nu}H)$	3.0%	3.2%

Decay mode	$\sigma \times \text{BR}$	BR	$\sigma \times \text{BR}$	BR
$H \rightarrow b\bar{b}$	0.26%	0.56%	0.27%	0.56%
$H \rightarrow c\bar{c}$	3.1%	3.1%	3.3%	3.3%
$H \rightarrow gg$	1.2%	1.3%	1.3%	1.4%
$H \rightarrow WW^*$	0.9%	1.1%	1.0%	1.1%
$H \rightarrow ZZ^*$	4.9%	5.0%	5.1%	5.1%
$H \rightarrow \gamma\gamma$	6.2%	6.2%	6.8%	6.9%
$H \rightarrow Z\gamma$	13%	13%	15%	15%
$H \rightarrow \tau^+\tau^-$	0.8%	0.9%	0.8%	1.0%
$H \rightarrow \mu^+\mu^-$	16%	16%	17%	17%
$\text{BR}_{\text{BSM}}(H \rightarrow \text{inv})$	–	< 0.28%	–	< 0.30%

future. The center-of-mass energy will be known better than 1 MeV, resulting negligible uncertainties on the theoretical cross section predictions and experimental recoil mass measurements.

## 6.2 Extrapolation to CEPC-v4

As discussed in Section 2.4, the CEPC conceptual detector design has evolved from CEPC-v1 to CEPC-v4 with the main change being the reduction of the solenoidal field from 3.5 Tesla to 3.0 Tesla. In the meantime, the nominal CEPC center-of-mass energy for the Higgs boson factory has been changed from 250 GeV to 240 GeV. The results presented above are based on CEPC-v1 operating at  $\sqrt{s} = 250$  GeV. However given the relative small differences in the performances of the two detector concepts and in  $\sqrt{s}$ , the results for CEPC-v4 operating at  $\sqrt{s} = 240$  GeV can be estimated through extrapolation taking into account changes in signal and background cross sections as well as track momentum resolution. From 250 GeV to 240 GeV, the  $e^+e^- \rightarrow ZH$  and  $e^+e^- \rightarrow \nu_e\bar{\nu}_e H$  cross sections are reduced, respectively, by approximate 5% and 10% while cross sections for background processes are increased by up to 10%. The change in magnetic field affects the  $H \rightarrow \mu^+\mu^-$  analysis the most whereas its effect on other analyses are negligible. The extrapolated results for CEPC-v4 at 240 GeV are included in Table 11. In most cases, small

degradations of a few percent are expected. For the following analyses, the extrapolated results for CEPC-v4 at  $\sqrt{s} = 240$  GeV are used.

## 6.3 Measurement of Higgs boson width

The Higgs boson width ( $\Gamma_H$ ) is of special interest as it is sensitive to BSM physics in Higgs boson decays that are not directly detectable or searched for. However, the 4.07 MeV width predicted by the SM is too small to be measured with a reasonable precision from the distributions of either the invariant mass of the Higgs boson decay products or the recoil mass of the system produced in association with the Higgs boson. Unique to lepton colliders, the width can be determined from the measurements of Higgs boson production cross sections and its decay branching ratios. This is because the inclusive  $e^+e^- \rightarrow ZH$  cross section  $\sigma(ZH)$  can be measured from the recoil mass distribution, independent of Higgs boson decays.

Measurements of  $\sigma(ZH)$  and BR's have been discussed in Sections 4 and 5. Combining these measurements, the Higgs boson width can be calculated in a model-independent way:

$$\Gamma_H = \frac{\Gamma(H \rightarrow ZZ^*)}{\text{BR}(H \rightarrow ZZ^*)} \propto \frac{\sigma(ZH)}{\text{BR}(H \rightarrow ZZ^*)} \quad (5)$$

Here  $\Gamma(H \rightarrow ZZ^*)$  is the partial width of the  $H \rightarrow ZZ^*$

decay. Because of the small expected  $\text{BR}(H \rightarrow ZZ^*)$  value for a 125 GeV Higgs boson (2.64% in the SM), the precision of  $\Gamma_H$  is limited by the  $H \rightarrow ZZ^*$  statistics. It can be improved using the decay final states with the expected large BR values, for example the  $H \rightarrow b\bar{b}$  decay:

$$\Gamma_H = \frac{\Gamma(H \rightarrow b\bar{b})}{\text{BR}(H \rightarrow b\bar{b})} \quad (6)$$

$\Gamma(H \rightarrow b\bar{b})$  can be independently extracted from the cross section of the  $W$  fusion process  $e^+e^- \rightarrow \nu\bar{\nu}H \rightarrow \nu\bar{\nu}b\bar{b}$ :

$$\sigma(\nu\bar{\nu}H \rightarrow \nu\bar{\nu}b\bar{b}) \propto \Gamma(H \rightarrow WW^*) \cdot \text{BR}(H \rightarrow b\bar{b}) \quad (7)$$

$$= \Gamma(H \rightarrow b\bar{b}) \cdot \text{BR}(H \rightarrow WW^*) \quad (8)$$

Thus the Higgs boson total width

$$\Gamma_H = \frac{\Gamma(H \rightarrow b\bar{b})}{\text{BR}(H \rightarrow b\bar{b})} \propto \frac{\sigma(e^+e^- \rightarrow \nu_e\bar{\nu}_e H)}{\text{BR}(H \rightarrow WW^*)} \quad (9)$$

Here  $\text{BR}(H \rightarrow b\bar{b})$  and  $\text{BR}(H \rightarrow WW^*)$  are measured from the  $e^+e^- \rightarrow ZH$  process. The limitation of this method is the precision of the  $\sigma(e^+e^- \rightarrow \nu\bar{\nu}H \rightarrow \nu\bar{\nu}b\bar{b})$  measurement.

The expected precision on  $\Gamma_H$  is 5.4% from the measurements of  $\sigma(ZH)$  and  $\text{BR}(H \rightarrow ZZ^*)$  and is 3.3% from the measurements of  $\sigma(\nu\bar{\nu}H \rightarrow \nu\bar{\nu}b\bar{b})$ ,  $\text{BR}(H \rightarrow b\bar{b})$  and  $\text{BR}(H \rightarrow WW^*)$ . The former is dominated by the precision of the  $\text{BR}(H \rightarrow ZZ^*)$  measurement while the latter by the  $\sigma(\nu\bar{\nu}H \rightarrow \nu\bar{\nu}b\bar{b})$  measurement. The combined  $\Gamma_H$  precision of the two measurements is 3.1%, taking into account correlations between the two measurements.

## 7 Higgs Boson Coupling Measurements

To understand the implications of the predicted measurement precision shown in Table 11 on possible new physics models, one would need to translate them into constraints on the parameters in the Lagrangian. This is frequently referred to as Higgs boson coupling measurement, even though this way of phrasing it can be misleading as discussed in the following.

There are different ways of presenting the constraints. Before going into CEPC results, we briefly comment on the reasons behind choices of schemes in this section. First, the goal of theory interpretation is different from analyzing actual data, where a lot of detailed work will be done to derive the extended sets of observables. Instead, obtaining a broad brushed big picture of the basic capability of the Higgs boson coupling measurement at the CEPC is the goal. Ideally, the presentation would be simple with a intuitive connection with the observables. The presentation would ideally also be free of underlying model assumptions. In addition, it would be convenient

if the result presentation can be interfaced directly with higher order computations, RGE evolutions, and so on. However, achieving all of these goals simultaneously is not possible. Two of the most popular and balanced approaches are the so-called  $\kappa$ -framework and the Effective Field Theory (EFT) analysis. As discussed in more detail later, none of these is perfect. At the same time, neither of these is wrong as long as one is careful not to over interpreting the result. Another important aspect of making projections on the physics potential of a future experiment is that they will be compared with other possible future experiments. Hence, CEPC follows the most commonly used approaches to facilitate such comparisons.

Motivated by these arguments, in the following, CEPC presents the projections using both the  $\kappa$ -framework and EFT approach. In the later part of this section, Higgs physics potential beyond coupling determination will be discussed.

### 7.1 Coupling fits in the $\kappa$ -framework

The Standard Model makes specific predictions for the Higgs boson couplings to the SM fermions,  $g(Hff; \text{SM})$ , and to the SM gauge bosons  $g(HVV; \text{SM})$ .<sup>‡</sup> In the  $\kappa$ -framework, the potential deviations are parametrized by

$$\kappa_f = \frac{g(Hff)}{g(Hff; \text{SM})}, \quad \kappa_V = \frac{g(HVV)}{g(HVV; \text{SM})}, \quad (10)$$

with  $\kappa_i = 1$  indicating agreement with the SM prediction.

In addition to couplings which are present at tree level, the Standard Model also predicts effective couplings  $H\gamma\gamma$  and  $Hgg$ , in terms of other SM parameters. Changes in the gluon and photon couplings can be induced by the possible shifts in the Higgs boson couplings described above. In addition, these couplings can also be altered by loop contributions from new physics states. Hence, these couplings will be introduced as two independent couplings, with their ratios to the SM predictions denoted as  $\kappa_\gamma$  and  $\kappa_g$ .

Furthermore, it is possible that the Higgs boson can decay directly into new physics particles. In this case, two type of new decay channels will be distinguished:

1. Invisible decay. This is a specific channel in which Higgs boson decay into invisible particles. This can be searched for and, if detected, measured.
2. Exotic decay. This includes all the other new physics channels. Whether they can be observed, and, if so, to what precision, depends sensitively on the particular final states. In one extreme, they can be very distinct and can be measured very well.

<sup>‡</sup>For the discussion of coupling fits and their implications, “ $H$ ” is used to denoted the 125 GeV Higgs boson.

In another extreme, they can be in a form which is completely swamped by the background. Whether postulating a precision for the measurement of the exotic decay or treating it as an independent parameter (essentially assuming it can not be measured directly) is an assumption one has to make. In the latter case, it is common to use the total width  $\Gamma_H$  as an equivalent free parameter.<sup>§</sup>

In general, possible deviations of all Standard Model Higgs boson couplings should be considered. However, in the absence of obvious light new physics states with large couplings to the Higgs boson and other SM particles, a very large deviation ( $> \mathcal{O}(1)$ ) is unlikely. In the case of smaller deviations, the Higgs boson phenomenology will not be sensitive to the deviations of  $\kappa_e, \kappa_u, \kappa_d$  and  $\kappa_s$  [44]. Therefore, they will not be considered here and set to be their SM values.

The CEPC will not be able to directly measure the Higgs boson coupling to top quarks. A deviation of this coupling from its SM value does enter  $H\gamma\gamma$  and  $Hgg$  amplitudes. However, this can be viewed as parametrized by  $\kappa_\gamma$  and  $\kappa_g$  already. Therefore, we will not include  $\kappa_t$  as an independent parameter. Hence, the following set of 10 independent parameters is considered:

$$\kappa_b, \kappa_c, \kappa_\tau, \kappa_\mu, \kappa_Z, \kappa_W, \kappa_\gamma, \kappa_g, \text{BR}_{\text{inv}}^{\text{BSM}}, \Gamma_H. \quad (11)$$

Several assumptions can be made that can lead to a reduced number of parameters (see also [37, 45]). It can be reduced to a 7-parameter set, by assuming lepton universality, and the absence of exotic and invisible decays (excluding  $H \rightarrow ZZ^* \rightarrow \nu\bar{\nu}\nu\bar{\nu}$ ) [45, 46]:

$$\kappa_b, \kappa_c, \kappa_\tau = \kappa_\mu, \kappa_Z, \kappa_W, \kappa_\gamma, \kappa_g. \quad (12)$$

This is useful for hadron collider studies since it can not measure the Higgs boson total width with precision; it is more useful for models in which this assumption is satisfied.

There are some pros and cons of the  $\kappa$ -framework.  $\kappa_i$ s give a simple and intuitive parametrization of potential deviations. It has a direct connection with the observables shown in Table 11. It does cover a lot of possible modifications of the coupling. At the same time,  $\kappa$ -framework has its limitations. Strictly speaking, it should not be understood as modifying the SM renormalizable Lagrangian by a multiplicative factor. For instance, individual  $\kappa$  modifications violates gauge invariance. The higher order corrections in the  $\kappa$  framework is not easily defined.  $\kappa_i$ s do not summarize all possible effects of new physics neither. For example, in addition to the overall size, potential new physics can also introduce

form factors which can change the kinematics of particles connected to a vertex. Manifestations of this effect will be seen in the discussion of the EFT approach. Furthermore, the Higgs-to-diphoton in the SM could have non-trivial on-shell and off-shell interference effect [47, 48], which can be used to constrain Higgs boson properties and help resolve higher dimensional operators. It is useful to pause here and compare with the EFT scheme introduced in detail in the next subsection. The EFT scheme relates  $\kappa_Z$  and  $\kappa_W$ , and further expance them into three different Lorentz structures. In addition, some of these higher dimensional  $HVV$  coupling are also in connection with  $\kappa_\gamma$  and anomalous trilinear gauge couplings. The current EFT scheme does not include important new degree of freedom  $\text{BR}_{\text{inv}}^{\text{BSM}}$  and  $\Gamma_H$  as independent parameters. Overall,  $\kappa$ -framework does capture the big picture of the capability of precision Higgs boson measurement at CEPC. It is useful as long as we understand its limitation.

The LHC and especially the HL-LHC will provide valuable and complementary information about the Higgs boson properties. For example, the LHC is capable of directly measure the  $t\bar{t}H$  process [50, 51]. In addition, the LHC could use differential cross sections to differentiate top-loop contributions and other heavy particle-loop contributions to the Higgs boson to gluon coupling [52–55], and similarly to separate contributions from different operators to the Higgs boson to vector boson couplings [56]. For the purpose of the coupling fit in the  $\kappa$ -framework, the LHC with its large statistics, helps improving precision on rare processes such as Higgs boson to diphoton couplings. Note that a large portion of the systematics intrinsic to a hadron collider would be canceled by taking ratios of measured cross sections. For example, combining the ratio of the rates  $pp \rightarrow H \rightarrow \gamma\gamma$  and  $pp \rightarrow H \rightarrow ZZ^*$  and the measurement of  $HZZ$  coupling at the CEPC can significantly improve the measurement of  $\kappa_\gamma$ . These are the most useful inputs from the LHC to combine with the CEPC. Similar studies of combination with the LHC for the ILC can be found in Refs. [57–61].

The 10-parameter fit and the 7-parameter fit for CEPC with integrate luminosity of  $5.6 \text{ ab}^{-1}$  are shown in Table 7.1. In addition, the combinations with expectations (optimistically assuming no theoretical uncertainties) from the HL-LHC from Ref. [49] are shown in the same tables as well.<sup>¶</sup> We assume the HL-LHC will operate at 14 TeV center-of-mass energy and accumulate an integrated luminosity of  $3000 \text{ fb}^{-1}$ .

The CEPC Higgs boson properties measurements mark a giant step beyond the HL-LHC. First of all, in

<sup>§</sup>Total width is a very useful parameter in understanding and deriving parameter precisions in the  $\kappa$ -scheme.

<sup>¶</sup>We note here that the LHC and the CEPC have different sources of theoretical uncertainties, for detailed discussion, see Refs. [37, 46, 62–64].

Table 12. Coupling measurement precision in percentage from the 7-parameter fit and 10-parameter fit described in the text for the CEPC, and corresponding results after combination with the HL-LHC. All the numbers refer to are relative precision except for  $BR_{inv}^{BSM}$  of beyond standard model for which 95% CL upper limit are quoted respectively. Some entries are left vacant for the 7-parameter fit to stress them being dependent parameter under the fitting assumptions of the 7-parameter fit scheme.

	10-parameter fit		7-parameter fit	
	CEPC	+HL-LHC	CEPC	+HL-LHC
$\Gamma_H$	3.1	2.5	–	–
$\kappa_b$	1.6	1.2	1.5	1.1
$\kappa_c$	2.2	1.9	2.2	1.9
$\kappa_g$	1.6	1.3	1.6	1.2
$\kappa_W$	1.4	1.1	1.4	1.0
$\kappa_\tau$	1.5	1.2	1.5	1.1
$\kappa_Z$	0.25	0.25	0.15	0.15
$\kappa_\gamma$	3.7	1.6	3.7	1.6
$\kappa_\mu$	8.7	5.0	–	–
$BR_{inv}^{BSM}$	< 0.30	< 0.30	–	–

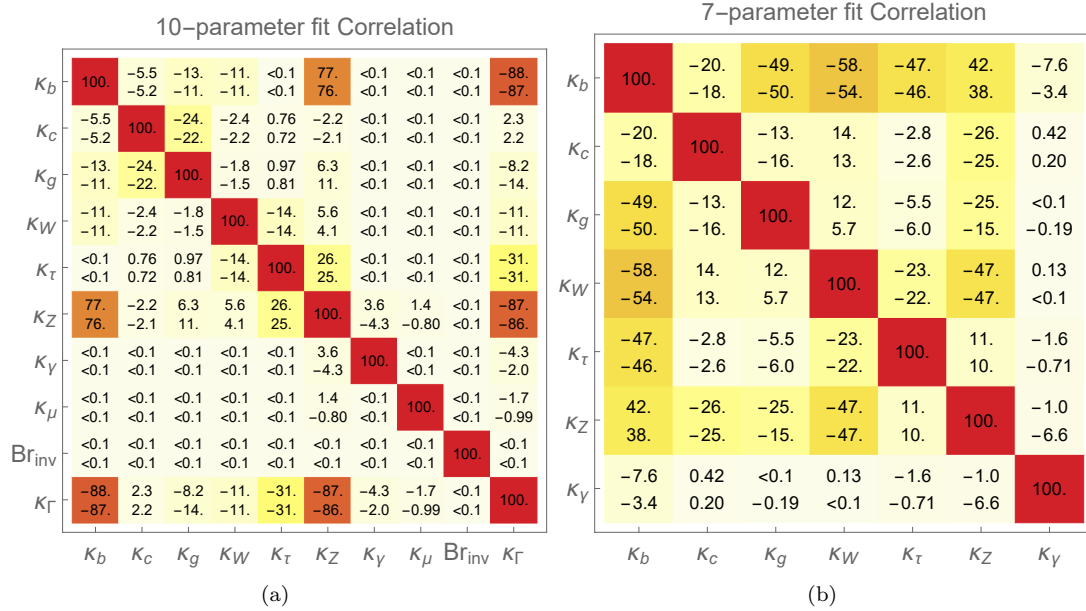


Fig. 20. The correlation of the 10-parameter fit and 7-parameter fit shown the left and right panel, respectively. The upper (lower) number in each entry represent the CEPC (combined fit with HL-LHC) fit results.

contrast to the LHC, a lepton collider Higgs factory is capable of measuring the absolute width and coupling strengths of the Higgs boson. A comparison with the HL-LHC is only possible with model dependent assumptions. One of such comparison is within the framework of a 7-parameter fit, shown in Fig. 21. Even with this set of restrictive assumptions, the advantage of the CEPC is still significant. The measurement of  $\kappa_Z$  is more than a factor of 10 better. The CEPC can also improve significantly on a set of channels which suffers from large

background at the LHC, such as  $\kappa_b$ ,  $\kappa_c$ , and  $\kappa_g$ . Note that this is in comparison with the HL-LHC projection with aggressive assumptions about systematics. Such uncertainties are typically under much better control at lepton colliders. Within this 7-parameter set, the only coupling which the HL-LHC can give a competitive measurement is  $\kappa_\gamma$ , for which the CEPC's accuracy is limited by statistics. This is also the most valuable input that the HL-LHC can give to the Higgs boson coupling measurement at the CEPC, which underlines the importance

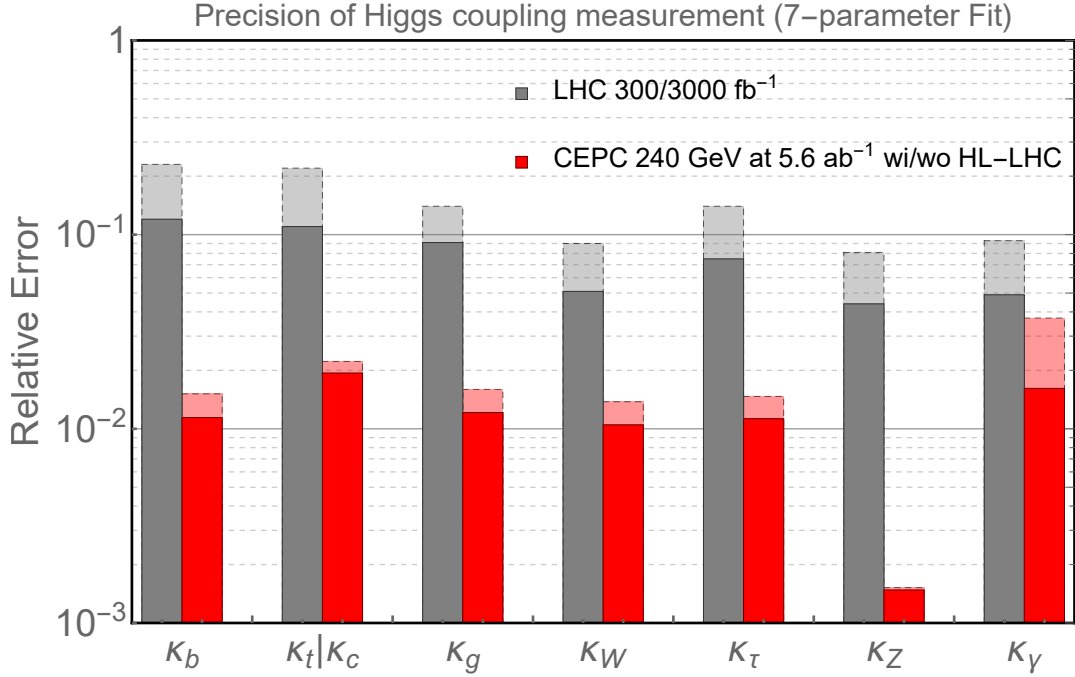


Fig. 21. The 7 parameter fit result, and comparison with the HL-LHC [49]. The projections for the CEPC at 240 GeV with  $5.6ab^{-1}$  integrated luminosity are shown. The CEPC results without combination with the HL-LHC input are shown with dashed edges. The LHC projections for an integrated luminosity of  $300fb^{-1}$  are shown in dashed edges.

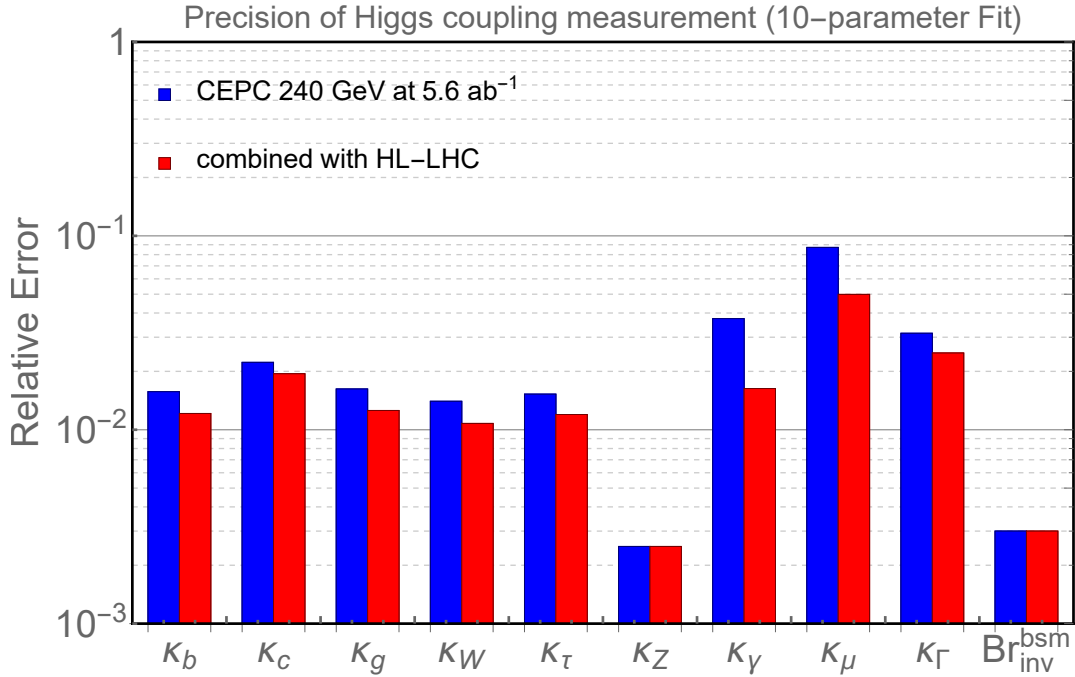


Fig. 22. The 10 parameter fit result for CEPC at 240 GeV with  $5.6ab^{-1}$  integrated luminosity (blue) and in combination with HL-LHC inputs (red). All the numbers refer to are relative precision except for  $BR_{inv}^{BSM}$  for which 95% CL upper limit are quoted respectively.

of combining the results of these two facilities.

The direct search limit for BSM Higgs boson decay into invisible particles  $\text{BR}_{\text{inv}}^{\text{BSM}}$  is well motivated, in close connection to dark sectors. The CEPC with  $5.6 \text{ ab}^{-1}$  can measure this to a high accuracy with a 95% CL upper limit of 0.30%, as shown in Table 7.1. At the same time, the HL-LHC can only manage a much lower accuracy 6–17% [46] and some improved analysis may reach 2–3.5% [65].

As discussed above, one of the greatest advantages of lepton collider Higgs boson factory is the capability of determining the Higgs boson coupling *model independently*. The projection of such a determination at the CEPC is shown in Fig. 22. The advantage of the higher integrated luminosity at a circular lepton collider is apparent. The CEPC has a clear advantage in the measure of  $\kappa_Z$ . It is also much stronger in  $\kappa_\mu$  and  $\text{BR}_{\text{inv}}^{\text{BSM}}$  measurements.

In Fig. 20 the correlation matrix for the 10-parameter and 7-parameter fit in the  $\kappa$ -scheme in percentage are shown in the left panel and right panel, respectively. The darker color represent stronger correlations and the numbers in the off-diagonal entries represent the correlation before and after combination with HL-LHC Higgs boson precision inputs, in the upper and lower entries, respectively. Comparing the 10-parameter with 7-parameter fit, the 7-parameter fit has much larger correlations between different entries, as the improved precision comparing with 10-parameter fit does come from having the total width as a summation of all decay channels. In the 10-parameter fit, the only entries with strong correlations are between  $\kappa_Z$  with  $\Gamma$  and  $\kappa_b$ , which can be understood in the discussion of the large dependence of width determination on inclusive  $ZH$  cross section measurement. Very naturally, the HL-LHC and CEPC are very complimentary and almost all entries after combinations have reduced correlation. One exception is the correlations between  $\kappa_Z$  and  $\kappa_\gamma$  as HL-LHC dominants the precision in  $\kappa_\gamma$  through the ratio measurement in both the 10-parameter fit and 7-parameter fit. In the 7-parameter fit, in addition, the correlation between  $\kappa_b$  and  $\kappa_\gamma$ ,  $\kappa_W$  and  $\kappa_g$ , as well as  $\kappa_g$  with  $\kappa_b$  and  $\kappa_c$  are slightly increased. This slight increase in correlation are mainly coming from the HL-LHC improvement in the  $\kappa_g$  through the gluon-gluon fusion rate measurement.

## 7.2 Effective-field-theory analysis

With the assumption that the new physics particles are heavier than the relevant energy of the Higgs factory, their effect can be characterized in the effective-field-theory (EFT) framework, in which higher dimensional operators supplement the Standard Model Lagrangian. Imposing baryon and lepton numbers conservations, all

higher dimensional operators are of even dimension:

$$\mathcal{L}_{\text{EFT}} = \mathcal{L}_{\text{SM}} + \sum_i \frac{c_i^{(6)}}{\Lambda^2} \mathcal{O}_i^{(6)} + \sum_j \frac{c_j^{(8)}}{\Lambda^4} \mathcal{O}_j^{(8)} + \dots \quad (13)$$

The leading effects of new physics at the electroweak scale would be the dimension-six operators. To obtain robust constraints on the Wilson coefficients  $c_i$ , a global analysis is required which includes the contributions from all possible dimension-six operators. While a large number of dimension-six operators can be written down, only a subset of them contribute to the Higgs boson processes at leading order. Among these operators, some are much better constrained by other measurements. It is thus reasonable to focus on the operators that primarily contribute to the Higgs boson processes and reduce the parameter space by making appropriate assumptions, as done in many recent studies of EFT global analysis at future lepton colliders [61, 66–71]. Following these studies, the  $CP$ -violating operators as well as the ones that induce fermion dipole interactions are discarded in this analysis. At leading order,  $CP$ -violating operators do not have linear contributions to the rates of Higgs boson processes. While they do contribute to the angular observables at the leading order [72, 73], these operators are usually much better constrained by EDM experiments [74–76], though some rooms are still possible for the  $CP$ -violating couplings of Higgs boson to the heavy flavor quarks and leptons [77, 78]. The interference between the fermion dipole interactions with SM terms are suppressed by the fermion masses. The corresponding operators also generate dipole moments, which are stringently constrained especially for light fermions. For the operators that modify the Yukawa matrices, only the five diagonal ones that correspond to the top, charm, bottom, tau, and muon Yukawa couplings are considered, which are relevant for the Higgs boson measurements at CEPC.

Before presenting the projections, some brief comments on the EFT framework are in order. In comparison with the  $\kappa$ -framework, a significant advantage of the EFT framework is that it gives physical parametrizations of the new physics effect. EFT operators can be used directly in computations. It also allows natural inclusions of new observables, with possible correlations automatically taken into account. At the same time, the connections with experimental observables are less direct and intuitive. Sometimes, the EFT approach is referred to as model-independent. This is only accurate to a certain extent. At least, it assumes that there are no new light degrees of freedom. In practice, assumptions are often made to simplify the set of EFT operators, as also done here.

The electroweak precision observables are already tightly constrained by the LEP  $Z$ -pole and  $W$  mass measurements. The CEPC  $Z$ -pole run can further im-

prove the constraints set by LEP, thanks to the enormous amount ( $\sim 10^{11}$ ) of  $Z$  bosons that can be collected. The  $W$  mass can also be constrained within a few MeVs at CEPC even without a dedicated  $WW$  threshold run. Given that the expected precisions of the  $Z$ -pole observables and the  $W$  mass are much higher than the ones of Higgs boson observables, in the Higgs boson analysis, it is assumed that the former ones are perfectly constrained, which significantly simplifies the analysis. In particular, in a convenient basis all the contact interaction terms of the form  $HVf\bar{f}$  can be discarded since they also modify the fermion gauge couplings. Realistic  $Z$ -pole constraints have also been considered in recent studies [61, 69, 71], but certain assumptions (such as flavor-universality) and simplifications are made. Future studies with more general frameworks are desired to fully determine the impact of the  $Z$ -pole measurements on the Higgs boson analysis.

Table 13. The estimated constraints on aTGCs from the measurements of the diboson process ( $e^+e^- \rightarrow WW$ ) in the semi-leptonic channel at CEPC 240 GeV with  $5.6 \text{ ab}^{-1}$  data and unpolarized beams. All angular distributions are used in the fit. Only the statistical uncertainties of the signal events are considered, assuming a selection efficiency of 80%.

CEPC 240 GeV ( $5.6 \text{ ab}^{-1}$ )				
	uncertainty	correlation matrix		
		$\delta g_{1,Z}$	$\delta \kappa_\gamma$	$\lambda_Z$
$\delta g_{1,Z}$	$1.2 \times 10^{-3}$	1	0.08	-0.90
$\delta \kappa_\gamma$	$0.9 \times 10^{-3}$		1	-0.42
$\lambda_Z$	$1.3 \times 10^{-3}$			1

The measurements of the triple gauge couplings (TGCs) from the diboson process ( $e^+e^- \rightarrow WW$ ) play an important role in the Higgs boson coupling analysis under the EFT framework. Focusing on  $CP$ -even dimension-six operators, the modifications to the triple gauge vertices from new physics can be parametrized by three anomalous TGC parameters (aTGCs), conventionally denoted as  $\delta g_{1,Z}$ ,  $\delta \kappa_\gamma$  and  $\lambda_Z$  [79, 80]. Among them,  $\delta g_{1,Z}$  and  $\delta \kappa_\gamma$  are generated by operators that also contribute to the Higgs boson processes. At 240 GeV, the cross section of  $e^+e^- \rightarrow WW$  is almost two orders of magnitude larger than the one of the Higgsstrahlung process. The measurements of the diboson process thus provide strong constraints on the operators that generate the aTGCs. A dedicated study on the TGC measurements at CEPC is not available at the current moment. A simplified analysis is thus performed to estimate the precision reaches on the aTGCs. The results are shown in Table 13. The analysis roughly follows the methods in Refs. [68, 81]. Only the  $WW$  events in the semi-leptonic (electron or muon) channel are used, which have good

event reconstructions and also a sizable branching fraction ( $\approx 29\%$ ). In particular, the production polar angle, as well as the two decay angles of the leptonic  $W$ , can be fully reconstructed, which contain important information on the aTGCs. The two decay angles of the hadronic  $W$  can only be reconstructed with a two-fold ambiguity. A  $\chi^2$  fit of the three aTGC parameters to the binned distribution of all five angles is performed, from which the one-sigma precisions of the three aTGCs as well as the correlations among them are extracted. A signal selection efficiency of 80% is assumed. The effects of systematics and backgrounds are not considered, assuming they are under control after the selection cuts.

Table 14. A complete set of  $CP$ -even dimension-six operators that contribute to the Higgs boson and TGC measurements, assuming there is no correction to the  $Z$ -pole observables and the  $W$  mass, and also no fermion dipole interaction. For  $\mathcal{O}_{y_u}$ ,  $\mathcal{O}_{y_d}$  and  $\mathcal{O}_{y_e}$ , only the contributions to the diagonal elements of the Yukawa matrices that corresponds to the top, charm, bottom, tau, and muon Yukawa couplings are considered.

$$\begin{aligned}
 \mathcal{O}_H &= \frac{1}{2} (\partial_\mu |H^2|)^2 \\
 \mathcal{O}_{WW} &= g^2 |H|^2 W_{\mu\nu}^a W^{a,\mu\nu} \\
 \mathcal{O}_{BB} &= g'^2 |H|^2 B_{\mu\nu} B^{\mu\nu} \\
 \mathcal{O}_{HW} &= ig (D^\mu H)^\dagger \sigma^a (D^\nu H) W_{\mu\nu}^a \\
 \mathcal{O}_{HB} &= ig' (D^\mu H)^\dagger (D^\nu H) B_{\mu\nu} \\
 \mathcal{O}_{GG} &= g_s^2 |H|^2 G_{\mu\nu}^A G^{A,\mu\nu} \\
 \mathcal{O}_{y_u} &= y_u |H|^2 \bar{Q}_L \tilde{H} u_R \quad (u \rightarrow t, c) \\
 \mathcal{O}_{y_d} &= y_d |H|^2 \bar{Q}_L H d_R \quad (d \rightarrow b) \\
 \mathcal{O}_{y_e} &= y_e |H|^2 \bar{L}_L H e_R \quad (e \rightarrow \tau, \mu) \\
 \mathcal{O}_{3W} &= \frac{1}{3!} g \epsilon_{abc} W_\mu^{a\nu} W_\nu^b W^{c\rho\mu}
 \end{aligned}$$

Under the assumptions specified above, the contributions to the Higgs boson and diboson processes from dimension-six operators consist of a total number of twelve degrees of freedom. While all non-redundant basis are equivalent, it is particularly convenient to choose a basis in which the twelve degrees of freedom can be mapped to exactly twelve operators, while the rest are removed by the assumptions. Two such bases are considered in our analysis, one is defined by the set of dimension-six operators in Table 14,

the other is the so-called ‘‘Higgs basis,’’ proposed in Ref. [82]. In the Higgs basis, the parameters are defined in the broken electroweak phase, and can be directly interpreted as the size of the Higgs boson couplings. Different from the original Higgs basis, this analysis follows Ref. [68], with the parameters associated with the  $Hgg$ ,  $H\gamma\gamma$  and  $HZ\gamma$  vertices normalized to the SM one-loop contributions, and denoted as  $\bar{c}_{gg}$ ,  $\bar{c}_{\gamma\gamma}$  and  $\bar{c}_{Z\gamma}$ . The parameter  $\bar{c}_{gg}^{\text{eff}}$  is further defined to absorb all contributions

to the  $Hgg$  vertex, as shown in Eq. 22. These redefined parameters can be more conveniently interpreted as the precisions of the Higgs boson couplings analogous to those in the  $\kappa$  framework. The exact definitions of the Higgs basis and the translation to the basis in Table 14 can be found in the end of the section.

The estimated precisions of all the Higgs boson rate measurements in Section 6 (Table 11), along with the correlations among them, are included as inputs for the EFT global analysis. In addition, the angular observables of the channel  $e^+e^- \rightarrow ZH$ ,  $Z \rightarrow \ell^+\ell^-$ ,  $H \rightarrow b\bar{b}$  are included, following the studies in Refs. [72, 73]. This channel is almost background-free after the selection cuts, with a signal selection efficiency of about 40%. For the TGC measurements, the results in Table 13 are used as inputs. The global  $\chi^2$  is obtained by summing over the  $\chi^2$  of all the measurements. Due to the high precision of the measurements, it is shown that for all observables, keeping only the linear terms of all EFT parameters gives a very good approximation [68]. This greatly simplifies the fitting procedure, as the total  $\chi^2$  can be written as

$$\chi^2 = \sum_{ij} (c - c_0)_i \sigma_{ij}^{-2} (c - c_0)_j, \text{ where } \sigma_{ij}^{-2} \equiv (\delta c_i \rho_{ij} \delta c_j)^{-1}, \quad (14)$$

where  $c_i$ 's are the EFT parameters,  $c_0$ 's are the corresponding central values which are zero by construction, as the measurements are assumed to be SM-like. The one-sigma uncertainties  $\delta c_i$  and the correlation matrix  $\rho$  can be obtained from  $\sigma_{ij}^{-2} = \partial^2 \chi^2 / \partial c_i \partial c_j$ .

For comparison, the reaches of the LHC 14 TeV are also considered, with a total luminosities of  $300 \text{ fb}^{-1}$  or  $3000 \text{ fb}^{-1}$ , which are combined with the diboson ( $e^+e^- \rightarrow WW$ ) measurements at LEP as well as the LHC 8 TeV Higgs boson measurements. For the LHC 14 TeV Higgs boson measurements, the projections by the ATLAS collaboration [49] are used, while the composition of each channel is obtained from Refs. [83–87]. The constraints from the LHC 8 TeV Higgs boson measurements and the diboson measurements at LEP are obtained directly from Ref. [88]. While the LHC diboson measurements could potentially improve the constraints on aTGCs set by LEP [89], they are not included in this analysis due to the potential issues related to the validity of the EFT [90, 91] and the TGC dominance assumption [92].

The results of the 12-parameter fit at CEPC are shown in Fig. 23 for the Higgs basis and Fig. 24 for the basis in Table 14. The results from LHC Higgs boson measurements (both  $300 \text{ fb}^{-1}$  and  $3000 \text{ fb}^{-1}$ ) combined with LEP diboson measurements are shown in comparison. The results of the combination of CEPC with HL-LHC ( $3000 \text{ fb}^{-1}$ ) are also shown in addition to

the ones of CEPC alone. In Fig. 23, the results are shown in terms of the one-sigma precision of each parameter. The LHC results are shown with gray columns with  $300 \text{ fb}^{-1}$  ( $3000 \text{ fb}^{-1}$ ) in light (solid) shades, while the CEPC ones are shown with the red columns, with the CEPC-alone (combination with HL-LHC) results shown in light (solid) shades. In Fig. 24, the results are presented in terms of the reaches of  $\Lambda/\sqrt{|c_i|}$  at 95% confidence level (CL), where  $\Lambda$  is the scale of new physics and  $c_i$  is the corresponding Wilson coefficient for each operator, defined in Eq. 13. Four columns are shown separately for LHC  $300 \text{ fb}^{-1}$ , LHC  $3000 \text{ fb}^{-1}$ , CEPC alone and CEPC combined with HL-LHC. The results of the global fits are shown with solid shades. The results from individual fits are shown with light shades, which are obtained by switching on one operator at a time with the rest fixed to zero. Similar analyses can be found, for example, in Refs. [93, 94].

It is transparent from Fig. 23 that CEPC provides very good reaches on the precisions of Higgs boson couplings, which are of one order of magnitude better than the ones at the LHC. For the parameters  $\bar{c}_{\gamma\gamma}$ ,  $\bar{c}_{Z\gamma}$  and  $\delta y_\mu$ , the clean signal and small branching ratios of the corresponding channels ( $H \rightarrow \gamma\gamma/Z\gamma/\mu\mu$ ) makes the HL-LHC precisions comparable with the CEPC ones. The combination with additional LHC measurements thus provides non-negligible improvements, especially for those parameters. It should be noted that, while  $\delta y_t$  modifies the  $Hgg$  vertex via the top loop contribution, CEPC alone could not discriminate it from the  $Hgg$  contact interaction ( $\bar{c}_{gg}$  in Eq. 23) obtained from integrating out a heavy new particle in the loop. The parameter  $\bar{c}_{gg}^{\text{eff}}$  absorbs both contributions and reflects the overall precision of the  $Hgg$  coupling. The combination with the LHC  $t\bar{t}H$  measurements could resolve this flat direction. The CEPC measurements, in turn, could improve the constraint on  $\delta y_t$  set by the LHC by providing much better constraints on the other parameters that contribute to the  $t\bar{t}H$  process. It should also be noted that the measurement of the charm Yukawa coupling is not reported in Ref. [49], while the projection of its constraint has a large variation among different studies and can be much larger than one [95–100]. Therefore,  $\delta y_c$  is fixed to be zero for the LHC-only fits, as treating  $\delta y_c$  as an unconstrained free parameter generates a flat direction in the fit which makes the overall reach much worse. The CEPC, on the other hand, provides excellent measurements of the charm Yukawa and can constrain  $\delta y_c$  to a precision of  $\sim 2\%$ .

Regarding the reaches of  $\Lambda/\sqrt{|c_i|}$  in Fig. 24, it is also clear that CEPC has a significantly better performance than the LHC. If the couplings are naively assumed to be of order one ( $c_i \sim 1$ ), the Higgs boson measurements at CEPC would be sensitive to new physics scales at mul-

tiple TeVs. While the individual reach for some of the operators at the LHC can be comparable to the ones at CEPC (*e.g.*,  $O_{WW}$  and  $O_{BB}$  from the measurement of  $H \rightarrow \gamma\gamma$ ), the reaches of CEPC are much more robust under a global framework thanks to its comprehensive measurements of both the inclusive  $ZH$  cross section and the exclusive rates of many Higgs boson decay channels. Operators  $O_{GG}$  and  $O_{yt}$  both contribute to the  $Hgg$  vertex. While the CEPC could provide strong constraints on either of them if the other is set to zero, they can only be constrained in a global fit if the  $t\bar{t}H$  measurements at the LHC are also included. It is also important to note that the validity of EFT could be a potential issue for the LHC measurements [90]. Depending on the size of the couplings, the inferred bounds on the new physics scale  $\Lambda$  could be comparable with or even smaller than the energy scale probed by the LHC. The CEPC has a smaller center of mass energy and much better precisions, which ensures the validity of EFT for most new physics scenarios.

In Table 15 and Fig. 25, the numerical results of the global fit are presented for CEPC in terms of the one-sigma precisions of the 12 parameters and the correlations among them. The results assume an integrated luminosity of  $5.6 \text{ ab}^{-1}$  at 240 GeV with unpolarized beams, both without and with the combination of HL-LHC ( $3000 \text{ fb}^{-1}$ ) Higgs boson measurements. With both the one-sigma bounds and the correlation matrix, the corresponding *chi-squared* can be reconstructed, which can be

used to derive the constraints in any other EFT basis or any particular model that can be matched to the EFT. This offers a convenient way to study the reaches on new physics models, as detailed knowledge of the experimental measurements are not required.

In the EFT framework, it is explicitly assumed that the Higgs boson total width is the sum of all the widths of its SM decay channels. This is because the EFT expansion in Eq. 13 relies on the assumption that the new physics scale is sufficiently large, while any potential Higgs boson exotic decay necessarily introduces light BSM particles, thus in direct conflict with this assumption. One could nevertheless treat the Higgs total width as a free parameter in the EFT global fit and obtain an indirect constraint of it, as done in Ref. [61]. With this treatment, the CEPC could constrain the Higgs total width to a precision of 1.7% (1.6% if combined with HL-LHC). This result is significantly better than the one from the 10-parameter coupling fit in Table 7.1 (3.4%/2.6%). The improvement is mainly because the  $HWW$  and  $HZZ$  couplings are treated as being independent in the 10-parameter coupling fit, while in the EFT framework they are related to each other under gauge invariance and custodial symmetry. It should also be noted that the Higgs width determined using Eq. (5) and (9) explicitly assumes that the  $HWW$  and  $HZZ$  couplings are independent of the energy scale. Such an assumption is not valid in the EFT framework with the inclusion of the anomalous couplings.

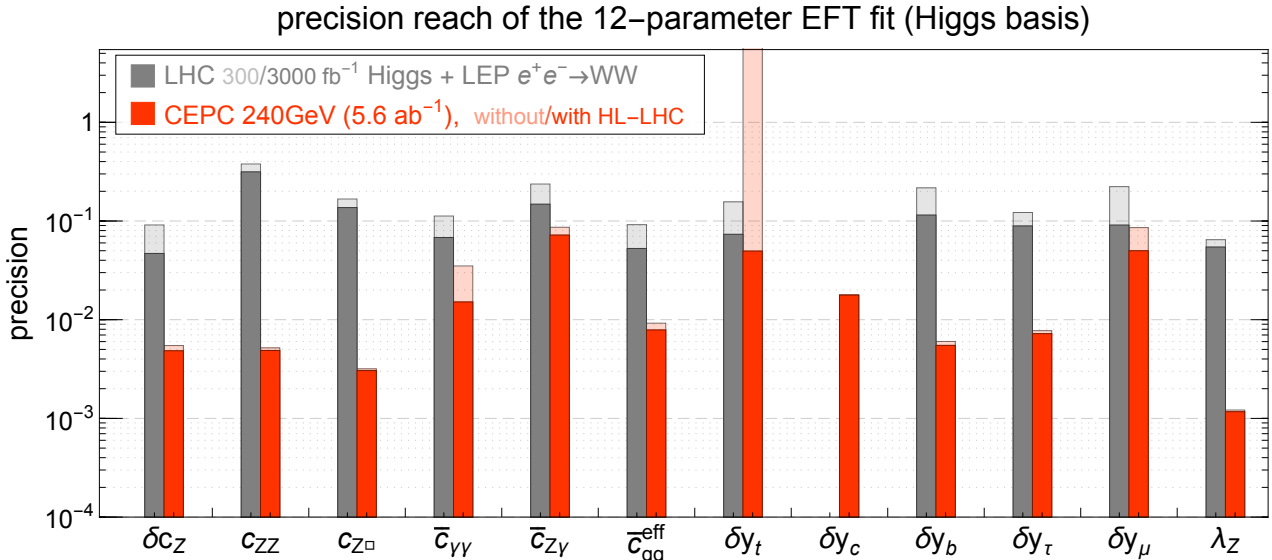


Fig. 23. One-sigma precision reach of the twelve parameters in the Higgs basis. The first column shows the results from the LHC Higgs boson measurements with  $300 \text{ fb}^{-1}$  (light shade) and  $3000 \text{ fb}^{-1}$  (solid shade) combined with LEP diboson ( $e^+e^- \rightarrow WW$ ) measurement. The second column shows the results from CEPC with  $5.6 \text{ ab}^{-1}$  data collected at 240 GeV with unpolarized beam. The results from CEPC alone are shown in light shades, and the ones from a combination of CEPC and HL-LHC are shown in solid shades.  $\delta y_c$  is fixed to zero for the LHC fits.

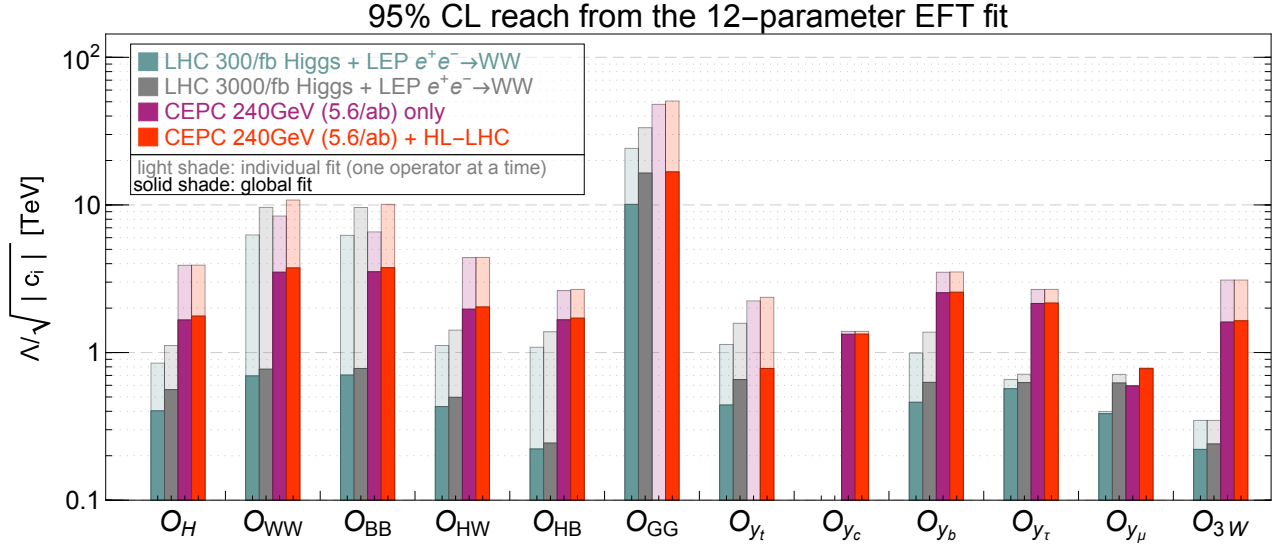


Fig. 24. The 95% CL reach on  $\Lambda/\sqrt{|c_i|}$  for the operators in the basis defined in Table 14. The first two columns show the results from LHC Higgs boson measurements with  $300\text{fb}^{-1}$  and  $3000\text{fb}^{-1}$  combined with LEP diboson ( $e^+e^- \rightarrow WW$ ) measurement. The last two columns show the results from CEPC alone and the combination of CEPC and HL-LHC ( $3000\text{fb}^{-1}$ ). The results of the global fits are shown with solid shades. The results from individual fits (by switching on one operator at a time) are shown with light shades.  $\delta y_c$  is fixed to zero for the LHC fits.

Table 15. The one-sigma uncertainties for the 12 parameters from CEPC (240 GeV,  $5.6\text{ab}^{-1}$ ) in the Higgs basis and the basis of dimension-six operators. For both cases, the upper (lower) row correspond to results without (with) the combination of the HL-LHC Higgs boson measurements. Note that, without the  $t\bar{t}H$  measurements,  $\delta y_t$  can not be constrained in a global fit, thus  $c_{GG}$  and  $c_{y_t}$  can not be resolved.

Higgs basis											
$\delta c_Z$	$c_{ZZ}$	$c_{Z\Box}$	$\bar{c}_{\gamma\gamma}$	$\bar{c}_{Z\gamma}$	$\bar{c}_{gg}^{\text{eff}}$	$\delta y_t$	$\delta y_c$	$\delta y_b$	$\delta y_\tau$	$\delta y_\mu$	$\lambda_Z$
0.0055	0.0052	0.0032	0.035	0.086	0.0092	–	0.018	0.0060	0.0077	0.086	0.0012
0.0048	0.0049	0.0031	0.015	0.072	0.0079	0.050	0.018	0.0055	0.0072	0.050	0.0012
$c_i/\Lambda^2$ [TeV <sup>-2</sup> ] of dimension-six operators											
$c_H$	$c_{WW}$	$c_{BB}$	$c_{HW}$	$c_{HB}$	$c_{GG}$	$c_{y_t}$	$c_{y_c}$	$c_{y_b}$	$c_{y_\tau}$	$c_{y_\mu}$	$c_{3W}$
0.18	0.041	0.040	0.13	0.18	–	–	0.28	0.077	0.11	1.4	0.19
0.16	0.036	0.035	0.12	0.17	0.0018	0.82	0.28	0.076	0.11	0.83	0.19

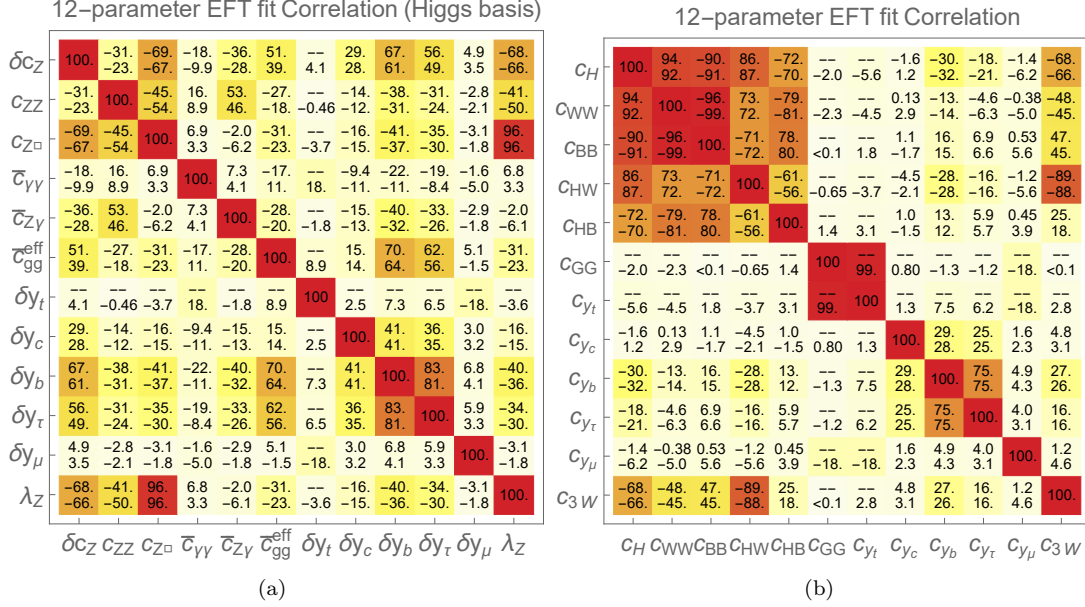


Fig. 25. The correlation matrix of the 12-parameter fit at the CEPC in (a) the Higgs basis and (b) the basis of dimension-six operators. The upper (lower) entries correspond to results without (with) the combination of the HL-LHC Higgs boson measurements.

### 7.2.1 The “12-parameter” EFT framework

The Higgs basis is proposed in Ref. [82] and applied in EFT studies of the LHC Higgs measurements such as Refs. [88, 101]. While the SM and the dimension-six operators are included with gauge invariances imposed, the parameters in the Higgs basis are defined in the broken electroweak phase Lagrangian, which makes the connection to measurements more straightforward. This analysis follows the framework in Ref. [68], which applies the Higgs basis to measurements at future lepton colliders. For simplicity, the  $CP$ -violating operators and the ones that induce fermion dipole interactions are discarded, and the  $Z$ -pole observables and  $W$  mass are assumed to be SM-like.

The SM and dimension-6 operators relevant for this study are

$$\mathcal{L} \supset \mathcal{L}_{HVV} + \mathcal{L}_{Hff} + \mathcal{L}_{\text{tgc}}, \quad (15)$$

where the couplings of the Higgs to the SM gauge bosons are

$$\begin{aligned} \mathcal{L}_{HVV} = & \frac{h}{v} \left[ (1 + \delta c_W) \frac{g^2 v^2}{2} W_\mu^+ W^{-\mu} \right. \\ & + (1 + \delta c_Z) \frac{(g^2 + g'^2) v^2}{4} Z_\mu Z^\mu \\ & + c_{WW} \frac{g^2}{2} W_{\mu\nu}^+ W^{-\mu\nu} \\ & + c_{W\Box} g^2 (W_\mu^- \partial_\nu W^{+\mu\nu} + \text{h.c.}) \\ & + c_{gg} \frac{g_s^2}{4} G_{\mu\nu}^a G^{a\mu\nu} \\ & + c_{\gamma\gamma} \frac{e^2}{4} A_{\mu\nu} A^{\mu\nu} + c_{Z\gamma} \frac{e\sqrt{g^2 + g'^2}}{2} Z_{\mu\nu} A^{\mu\nu} \\ & + c_{ZZ} \frac{g^2 + g'^2}{4} Z_{\mu\nu} Z^{\mu\nu} + c_{Z\Box} g^2 Z_\mu \partial_\nu Z^{\mu\nu} \\ & \left. + c_{\gamma\Box} gg' Z_\mu \partial_\nu A^{\mu\nu} \right]. \quad (16) \end{aligned}$$

Not all the parameters in Eq. 16 are independent. Imposing gauge invariances, one could choose to rewrite  $\delta c_W$ ,  $c_{WW}$ ,  $c_{W\Box}$  and  $c_{\gamma\Box}$  as<sup>||</sup>

$$\begin{aligned} \delta c_W &= \delta c_Z + 4\delta m, \\ c_{WW} &= c_{ZZ} + 2s_{\theta_W}^2 c_{Z\gamma} + s_{\theta_W}^4 c_{\gamma\gamma}, \\ c_{W\Box} &= \frac{1}{g^2 - g'^2} [g^2 c_{Z\Box} + g'^2 c_{ZZ} - e^2 s_{\theta_W}^2 c_{\gamma\gamma} - (g^2 - g'^2) s_{\theta_W}^2 c_{Z\gamma}], \\ c_{\gamma\Box} &= \frac{1}{g^2 - g'^2} [2g^2 c_{Z\Box} + (g^2 + g'^2) c_{ZZ} - e^2 c_{\gamma\gamma} - (g^2 - g'^2) c_{Z\gamma}], \end{aligned} \quad (17)$$

<sup>||</sup>In this subsection,  $s_{\theta_W}$ ,  $c_{\theta_W}$  and  $t_{\theta_W}$  are shorthands for  $\sin\theta_W$ ,  $\cos\theta_W$  and  $\tan\theta_W$ , where  $\theta_W$  is the weak mixing angle.

where  $\delta m$  is induced by custodial symmetry breaking effects and is set to zero in our framework. While the modifications to the Yukawa couplings are in general  $3 \times 3$  complex matrices in the family space, only the diagonal ones of  $t$ ,  $c$ ,  $b$ ,  $\tau$ ,  $\mu$  are considered,

$$\mathcal{L}_{Hff} = -\frac{h}{v} \sum_{f=t,c,b,\tau,\mu} m_f (1 + \delta y_f) \bar{f}_R f_L + \text{h.c.}, \quad (18)$$

which are relevant for the measurements. The anomalous triple gauge couplings (aTGCs) are given by

$$\begin{aligned} \mathcal{L}_{\text{tgc}} = & ig s_{\theta_W} A^\mu (W^{-\nu} W_{\mu\nu}^+ - W^{+\nu} W_{\mu\nu}^-) \\ & + ig (1 + \delta g_1^Z) c_{\theta_W} Z^\mu (W^{-\nu} W_{\mu\nu}^+ - W^{+\nu} W_{\mu\nu}^-) \\ & + ig [(1 + \delta \kappa_Z) c_{\theta_W} Z^{\mu\nu} + (1 + \delta \kappa_\gamma) s_{\theta_W} A^{\mu\nu}] W_\mu^- W_\nu^+ \\ & + \frac{ig}{m_W^2} (\lambda_Z c_{\theta_W} Z^{\mu\nu} + \lambda_\gamma s_{\theta_W} A^{\mu\nu}) W_v^{-\rho} W_{\rho\mu}^+, \end{aligned} \quad (19)$$

where  $V_{\mu\nu} \equiv \partial_\mu V_\nu - \partial_\nu V_\mu$  for  $V = W^\pm, Z, A$ . Gauge invariance further imposes  $\delta \kappa_Z = \delta g_{1,Z} - t_{\theta_W}^2 \delta \kappa_\gamma$  and  $\lambda_Z = \lambda_\gamma$ , thus leaving three independent aTGC parameters, which are chosen to be  $\delta g_{1,Z}$ ,  $\delta \kappa_\gamma$  and  $\lambda_Z$ . Two of them,  $\delta g_{1,Z}$  and  $\delta \kappa_\gamma$ , are related to Higgs observables and can be written as

$$\begin{aligned} \delta g_{1,Z} = & \frac{1}{2(g^2 - g'^2)} [-g^2(g^2 + g'^2) c_{Z\Box} - g'^2(g^2 + g'^2) c_{ZZ} \\ & + e^2 g'^2 c_{\gamma\gamma} + g'^2(g^2 - g'^2) c_{Z\gamma}], \\ \delta \kappa_\gamma = & -\frac{g^2}{2} \left( c_{\gamma\gamma} \frac{e^2}{g^2 + g'^2} + c_{Z\gamma} \frac{g^2 - g'^2}{g^2 + g'^2} - c_{ZZ} \right). \end{aligned} \quad (20)$$

In the Higgs basis, one therefore has the following 12 parameters:

$$\begin{aligned} \delta c_Z, \quad c_{ZZ}, \quad c_{Z\Box}, \quad c_{\gamma\gamma}, \quad c_{Z\gamma}, \quad c_{gg}, \\ \delta y_t, \quad \delta y_c, \quad \delta y_b, \quad \delta y_\tau, \quad \delta y_\mu, \quad \lambda_Z. \end{aligned} \quad (21)$$

A full list of the relevant observables in terms of the 12 EFT parameters can be found in Ref. [68]. In particular, only the tree level contributions of the EFT parameters are considered, except for the  $Hgg$  vertex for which the contributions of  $\delta y_t$  and  $\delta y_b$  via the fermion loops are also included. Also, following Ref. [68],  $c_{\gamma\gamma}$ ,  $c_{Z\gamma}$  and  $c_{gg}$  are normalized with respect to the SM 1-loop contributions to the  $H\gamma\gamma$ ,  $HZ\gamma$  and  $Hgg$  vertices. The corresponding parameters are denoted by  $\bar{c}_{\gamma\gamma}$ ,  $\bar{c}_{Z\gamma}$  and  $\bar{c}_{gg}$ , defined as

$$\frac{\Gamma_{\gamma\gamma}}{\Gamma_{\gamma\gamma}^{\text{SM}}} \simeq 1 - 2\bar{c}_{\gamma\gamma}, \quad \frac{\Gamma_{Z\gamma}}{\Gamma_{Z\gamma}^{\text{SM}}} \simeq 1 - 2\bar{c}_{Z\gamma}, \quad (22)$$

and

$$\frac{\Gamma_{gg}}{\Gamma_{gg}^{\text{SM}}} \simeq 1 + 2\bar{c}_{gg}^{\text{eff}} \simeq 1 + 2\bar{c}_{gg} + 2.10\delta y_t - 0.10\delta y_b. \quad (23)$$

They are related to the original parameters by

$$\bar{c}_{\gamma\gamma} \simeq \frac{c_{\gamma\gamma}}{8.3 \times 10^{-2}}, \quad \bar{c}_{Z\gamma} \simeq \frac{c_{Z\gamma}}{5.9 \times 10^{-2}}, \quad \bar{c}_{gg} \simeq \frac{c_{gg}}{8.3 \times 10^{-3}}. \quad (24)$$

It should be noted that, without the inclusion of LHC  $t\bar{t}H$  measurements, the CEPC measurements alone could only constrain a linear combination of  $c_{gg}$  and  $\delta y_t$ . In this case, the two parameters can be replaced by  $\bar{c}_{gg}^{\text{eff}}$  (defined in Eq. 23) which parametrize the total contribution to the  $Hgg$  vertex.

To translate to the basis in Table 14, a different normalization of the Wilson coefficients is chosen in order to simplify the expressions, defined as

$$\begin{aligned} \mathcal{L}_{\text{D6}} = & \frac{c_H}{v^2} \mathcal{O}_H + \frac{\kappa_{WW}}{m_W^2} \mathcal{O}_{WW} + \frac{\kappa_{BB}}{m_W^2} \mathcal{O}_{BB} + \frac{\kappa_{HW}}{m_W^2} \mathcal{O}_{HW} + \frac{\kappa_{HB}}{m_W^2} \mathcal{O}_{HB} \\ & + \frac{\kappa_{GG}}{m_W^2} \mathcal{O}_{GG} + \frac{\kappa_{3W}}{m_W^2} \mathcal{O}_{3W} + \sum_{f=t,c,b,\tau,\mu} \frac{c_{y_f}}{v^2} \mathcal{O}_{y_f}. \end{aligned} \quad (25)$$

In this basis, the aTGCs are given by

$$\begin{aligned} \delta g_{1,Z} = & -\frac{\kappa_{HW}}{c_{\theta_W}^2}, \\ \delta \kappa_\gamma = & -\kappa_{HW} - \kappa_{HB}, \\ \lambda_Z = & -\kappa_{3W}. \end{aligned} \quad (26)$$

The translation between the two bases is straightforward, given by

$$\begin{aligned} \delta c_Z = & -\frac{1}{2} c_H, \\ c_{ZZ} = & \frac{4}{g^2 + g'^2} (-\kappa_{HW} - t_{\theta_W}^2 \kappa_{HB} + 4c_{\theta_W}^2 \kappa_{WW} + 4t_{\theta_W}^2 s_{\theta_W}^2 \kappa_{BB}), \\ c_{Z\Box} = & \frac{2}{g^2} (\kappa_{HW} + t_{\theta_W}^2 \kappa_{HB}), \\ c_{\gamma\gamma} = & \frac{16}{g^2} (\kappa_{WW} + \kappa_{BB}), \\ c_{Z\gamma} = & \frac{2}{g^2} (\kappa_{HB} - \kappa_{HW} + 8c_{\theta_W}^2 \kappa_{WW} - 8s_{\theta_W}^2 \kappa_{BB}), \\ c_{gg} = & \frac{16}{g^2} \kappa_{GG}, \\ \delta y_f = & -\frac{1}{2} c_H - c_{y_f}. \end{aligned} \quad (27)$$

Note that Eq. 26 and Eq. 27 are only valid under the assumptions made in this analysis, more specifically, that there is no correction to the  $Z$ -pole observables and the  $W$  mass. The general expressions for the aTGCs can be found in Ref. [102]. Basis translations from the Higgs basis to the SILH' basis (and others) are provided in Ref. [82]. To go from the SILH' basis to the one in Ta-

ble 14, one simply trades  $\mathcal{O}_W, \mathcal{O}_B$  for  $\mathcal{O}_{WW}, \mathcal{O}_{WB}$ , using

$$\begin{aligned}\mathcal{O}_B &= \mathcal{O}_{HB} + \frac{1}{4}\mathcal{O}_{BB} + \frac{1}{4}\mathcal{O}_{WB}, \\ \mathcal{O}_W &= \mathcal{O}_{HW} + \frac{1}{4}\mathcal{O}_{WW} + \frac{1}{4}\mathcal{O}_{WB},\end{aligned}\quad (28)$$

where  $\mathcal{O}_{WB}$  is directly related to the  $Z$ -pole measurements and is discarded in our analysis.

### 7.3 The Higgs self-coupling

The Higgs boson self-coupling is a critical parameter governing the dynamics of the electroweak symmetry breaking. In the Standard Model, the Higgs trilinear and quadrilinear couplings are fixed once the values of the electroweak VEV and the Higgs mass are known. Any deviation from the SM prediction is thus clear evidence of new physics beyond the SM. The Higgs trilinear coupling is probed at the LHC with the measurement of the double-Higgs process,  $pp \rightarrow HH$ . Current bounds on the Higgs trilinear coupling is at the  $\mathcal{O}(10)$  level, while the HL-LHC is expected to improve the precision to the level of  $\mathcal{O}(1)$  [103]. The prospects for extracting the Higgs quadrilinear coupling are much less promising, even for a 100 TeV hadron collider [104].

To measure the double-Higgs processes at a lepton collider, a sufficiently large center of mass energy ( $\gtrsim 400$  GeV) is required, which is likely to be achieved only at a linear collider. The CEPC, instead, can probe the Higgs trilinear coupling via its loop contributions to the single Higgs processes. This indirect approach nevertheless provides competitive reaches since the loop suppression is compensated by the high precision of the Higgs measurements at CEPC [105]. With a precision of 0.5% on the inclusive  $ZH$  cross section at 240 GeV, the Higgs trilinear coupling can be constrained to a precision of 35%, assuming all other Higgs couplings that contributes to  $e^+e^- \rightarrow ZH$  are SM-like. \*\* While this indirect bound is comparable to the direct ones at linear colliders, it relies on strong assumptions which are only applicable to some specific models. A more robust approach is to include all possible deviations on the Higgs couplings simultaneously and constrain the Higgs trilinear coupling in a global fit. The EFT framework presented in Section 7.2 is ideal for such an analysis. Under this framework, the one-loop contributions of the trilinear Higgs coupling to all the relevant Higgs production and decay processes are included, following Ref. [70]. The new physics effect is parametrized by the quantity  $\delta\kappa_\lambda \equiv \kappa_\lambda - 1$ , where  $\kappa_\lambda$  is the ratio of the Higgs trilinear coupling to its SM value,

$$\kappa_\lambda \equiv \frac{\lambda_3}{\lambda_3^{\text{sm}}}, \quad \lambda_3^{\text{sm}} = \frac{m_H^2}{2v^2}. \quad (29)$$

The global fit is performed simultaneously with  $\delta\kappa_\lambda$  and the 12 EFT parameters in Section 7.2. The results are presented in Table 16. The results for HL-LHC are also shown, which were obtained in Ref. [106] under the same global framework. For CEPC 240 GeV, the one-sigma bound on  $\delta\kappa_\lambda$  is around  $\pm 3$ , significantly worse than the 35% in the  $\delta\kappa_\lambda$ -only fit. This is a clear indication that it is difficult to resolve the effects of  $\delta\kappa_\lambda$  from those of other Higgs couplings. For HL-LHC, the reach on  $\delta\kappa_\lambda$  is still dominated by the double-Higgs process. However, as a result of the destructive interferences among diagrams, the double-Higgs process at LHC could not constrain  $\delta\kappa_\lambda$  very well on its positive side, even with the use of differential observables [107]. The combination of HL-LHC and CEPC 240 GeV thus provides a non-trivial improvement to the HL-LHC result alone, in particular for the two-sigma bound on the positive side, which is improved from  $+6.1$  to  $+2.7$ . This is illustrated in Fig. 26, which plots the profiled  $\chi^2$  as a function of  $\delta\kappa_\lambda$  for the two colliders.

Table 16. The  $\Delta\chi^2 = 1$  (one-sigma) and  $\Delta\chi^2 = 4$  (two-sigma) bounds of  $\delta\kappa_\lambda$  for various scenarios, obtained in a global fit by profiling over all other EFT parameters. The results for HL-LHC are obtained from Ref. [106].

bounds on $\delta\kappa_\lambda$	$\Delta\chi^2 = 1$	$\Delta\chi^2 = 4$
CEPC 240 GeV (5.6ab <sup>-1</sup> )	[-3.0, +3.1]	[-5.9, +6.2]
HL-LHC	[-0.9, +1.3]	[-1.7, +6.1]
HL-LHC+CEPC 240 GeV	[-0.8, +1.0]	[-1.5, +2.7]

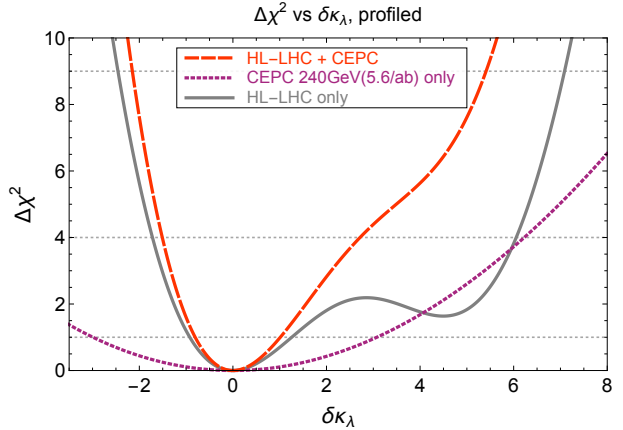


Fig. 26. Chi-square as a function of  $\delta\kappa_\lambda$  after profiling over all other EFT parameters for HL-LHC, CEPC and their combination.

### 7.4 Higgs and top couplings

Interactions of the Higgs boson with the top quark are widely viewed as a window to new physics beyond the Standard Model. Parametrizing effects of new physics in

\*\* A better precision can be obtained by also using the exclusive channels, such as  $\sigma(ZH) \times \text{BR}(H \rightarrow b\bar{b})$ , but would require an even stronger assumption that all Higgs couplings contributing to the branching ratios are also SM-like except the Higgs trilinear coupling.

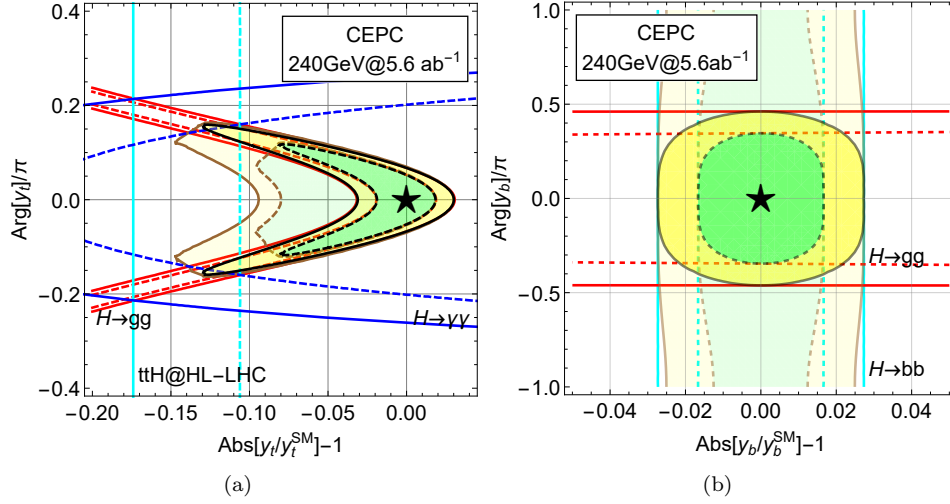


Fig. 27. Results for analysis on  $C_{y_t}$  and  $C_{y_b}$  in the projected allowed regions for modification to top and bottom Yukawa couplings in magnitude and  $CP$  phase at 68% and 95% confidence level. The combined results for CEPC are shown in black curves. The source of individual constraints for the single operator analysis are labeled correspondingly. For a joint analysis of simultaneous appearance of both  $\mathcal{O}_{y_t}$  and  $\mathcal{O}_{y_b}$  operators, the results for CEPC are shown in the enlarged yellow (95%) and green regions (68%) with thick brown boundary lines.

terms of dimension-six gauge-invariant operators modifying the Higgs-top interactions [108, 109], the Higgs top couplings physics potential at CEPC can be evaluated [110–113]. This EFT basis enlarges the Higgs EFT considered above. Moreover, the  $CP$  violation effects in the third generation Yukawas can be reflected as the complexity of the Wilson coefficients of operator  $\mathcal{O}_{y_t}$  and  $\mathcal{O}_{y_b}$ ,

$$\Delta y_t = y_t^{\text{SM}} \left( \Re[C_{y_t}] \frac{v^3}{2m_t \Lambda^2} + i \Im[C_{y_t}] \frac{v^3}{2m_t \Lambda^2} \right) \quad (30)$$

$$\Delta y_b = y_b^{\text{SM}} \left( \Re[C_{y_b}] \frac{v^3}{2m_b \Lambda^2} + i \Im[C_{y_b}] \frac{v^3}{2m_b \Lambda^2} \right) \quad (31)$$

In this section, the effect of introducing  $CP$  phases in the Yukawa operators in Higgs physics are discussed. For more detailed discussion on a complete set of Higgs and Top operators, see Ref. [110]. The dominant sources of constraints are from  $H \rightarrow \gamma\gamma$  and  $H \rightarrow gg$  for  $\mathcal{O}_{y_t}$ , and  $H \rightarrow gg$  and  $H \rightarrow b\bar{b}$  for  $\mathcal{O}_{y_b}$ . Given that  $H \rightarrow gg$  measurements are sensitive to both operators, a joint analysis of  $\mathcal{O}_{y_t}$  and  $\mathcal{O}_{y_b}$  will yield a significantly different result comparing to individual operator analysis. A joint analysis for these two operators in terms of Yukawa coupling strengths and the associated  $CP$  phases is performed at CEPC. The important physics cases for such considerations are highlighted.

In Fig. 27 constraints on the top and bottom Yukawa coupling strengths and their  $CP$  phases are presented in the left panel and right panel, respectively. The 68% and 95% exclusion bands are shown in solid and dashed lines. The limits for CEPC are shown in *bright* black

and magenta lines for individual operator analysis and the *bright* green and yellow shaded regions representing the 68% and 95% allowed parameter space, respectively. The *dimmed* thick black curves represent the results after turning on both operators  $\mathcal{O}_{tH}$  and  $\mathcal{O}_{bH}$  at the same time, using a profile-likelihood method profiling over other parameters. Furthermore, in the left panel the cyan band represents constraints from HL-LHC  $t\bar{t}H$  measurements, red bands are constraints from CEPC  $H \rightarrow gg$  measurements and blue bands are constraints from CEPC  $H \rightarrow \gamma\gamma$  measurements. Similarly in the right panel, the cyan bands are constraints from  $H \rightarrow b\bar{b}$  and the red bands are constraints from  $H \rightarrow gg$  at CEPC.

The left panel of Fig. 27 shows that the expected sensitivity on the modification in the magnitude of top Yukawa is at around  $\pm 3\%$  for the single operator analysis, which is relaxed to  $[-9.5\%, +3\%]$  for the joint analysis allowing the bottom Yukawa and the associated  $CP$  phase to vary freely, in the case of zero  $CP$  phase in the top Yukawa. The phase of the top Yukawa could be constrained to be  $\pm 0.16\pi$ . The constraints on the phase of the top Yukawa is driven by the  $H \rightarrow \gamma\gamma$  measurements, where a sizable phase shift will enlarge the Higgs to diphoton rate via reducing the interference with SM  $W$ -loop. The constraints on the magnitude of the top Yukawa modification is driven by the  $H \rightarrow gg$  measurements due to the dominant contribution to  $H \rightarrow gg$  being from top-loop. Note that constraints from  $H \rightarrow gg$  measurement is not entirely vertical, this is a result of the different sizes of the top-loop contribution to  $Hgg$  through scalar and pseudoscalar couplings. Similarly, as shown

in the right panel of Fig. 27 for the bottom Yukawa magnitude modification, the constraint is  $\pm 2.5\%$  and, for the bottom Yukawa  $CP$  phase, the constraints changes from  $\pm 0.47\pi$  to no constraint for simultaneous modification to top Yukawa.

## 8 Higgs boson $CP$ test and exotic decays

In addition to the studies based on the simulation of the CEPC baseline conceptual detector, reaches in testing Higgs boson spin/ $CP$  properties and in constraining branching ratios of Higgs boson exotic decays are also estimated. These estimates are based on previously published phenomenological studies and are summarized in this section.

### 8.1 Tests of Higgs boson spin/ $CP$ property

The  $CP$  parity of a Higgs boson, and more generally its anomalous couplings to gauge bosons in the presence of BSM physics, can be measured at the CEPC based on the  $e^+e^- (\rightarrow Z^*) \rightarrow ZH \rightarrow \mu^+\mu^- b\bar{b}$  process. It is convenient to express the anomalous coupling measurements in terms of physical quantities of effective fractions of events of the anomalous contribution relative to the SM predictions as detailed in Refs. [114–116], which are invariant under independent re-scalings of all couplings.

Two of the anomalous  $HZZ$  coupling measurements are of particular interest at the CEPC: the fraction of the high-order  $CP$ -even contribution due to either SM contribution or new physics,  $f_{a2}$ , and the fraction of a  $CP$ -odd contribution due to new physics,  $f_{a3}$ . The following two types of observables can be used to measure these anomalous couplings of the Higgs bosons.

1. The dependence of the  $e^+e^- \rightarrow Z^* \rightarrow ZH$  cross section on  $\sqrt{s}$  is different for different  $CP$  property of the Higgs boson [116]. Therefore, measurements of the cross section at several different energies will yield useful information about anomalous  $HZZ$  couplings. However this has non-trivial implications to the accelerator design and is not included in this study as a single value of  $\sqrt{s}$  is assumed for the CEPC operating as a Higgs boson factory.
2. Angular distributions,  $\cos\theta_1$  or  $\cos\theta_2$  and  $\Phi$  as defined in Fig. 28. These angles are also sensitive to interference between  $CP$ -even and  $CP$ -odd couplings. In particular forward-backward asymmetry with respect to  $\cos\theta_1$  or  $\cos\theta_2$  and non-trivial phase in the  $\Phi$  distributions can lead to an unambiguous interpretation of  $CP$  violation.

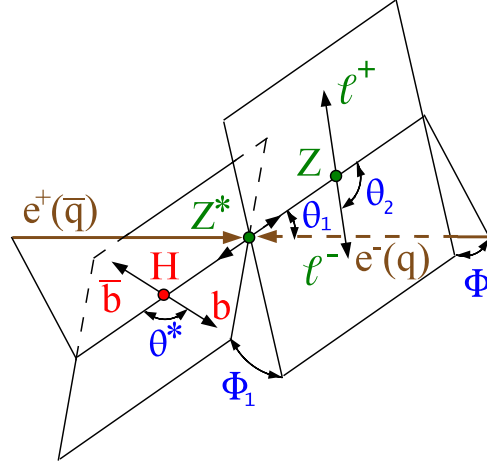


Fig. 28. The Higgs boson production and decay angles for the  $e^+e^- \rightarrow Z^* \rightarrow ZH \rightarrow \mu^+\mu^- b\bar{b}$  process.

To estimate the sensitivities on the anomalous couplings, a maximum likelihood fit [116] is performed to match observed three-dimensional angular distributions to theory predictions including signal and background processes. In this likelihood fit, the signal probability density functions are from analytical predictions that are validated using a dedicated MC program, the JHU generator [114, 115], which incorporates all the anomalous couplings, spin correlations, interference of all contributing amplitudes. The background probability density function is modeled from simulation based on  $e^+e^- \rightarrow ZZ \rightarrow \ell^+\ell^- b\bar{b}$  process in Madgraph [117].

Several thousand statistically-independent experiments are generated and fitted to estimate the sensitivity to  $f_{a2}$  and  $f_{a3}$ , defined as the smallest values that can be measured with  $3\sigma$  away from 0. All other parameters in the fit, including the number of expected signal and background events, are fixed. Figure 29 shows precision on  $f_{a2}$  and  $f_{a3}$  obtained with generated experiments. The expected sensitivity on  $f_{a2}$  and  $f_{a3}$  are 0.018 and 0.007 respectively.

The sensitivities of  $f_{a2}$  and  $f_{a3}$  are then converted to the equivalent parameters defined for the on-shell  $H \rightarrow ZZ^*$  decays,  $f_{a2}^{\text{dec}}$  and  $f_{a3}^{\text{dec}}$ , in order to compare with the sensitivities from the LHC experiments as described in Ref. [116]. The corresponding sensitivities of  $f_{a2}^{\text{dec}}$  and  $f_{a3}^{\text{dec}}$  are  $2 \times 10^{-4}$  and  $1.3 \times 10^{-4}$  respectively. The much smaller values in the  $f_{a2, a3}^{\text{dec}}$  are due to the much smaller  $m_{Z^*}^2$  in the  $H \rightarrow ZZ^*$  decay compared to the value in the  $Z^* \rightarrow ZH$  production. A simultaneous fit of  $f_{a2}$  and  $f_{a3}$  can also be performed with the 68% and 95% confidence level contours shown in Figure 29.

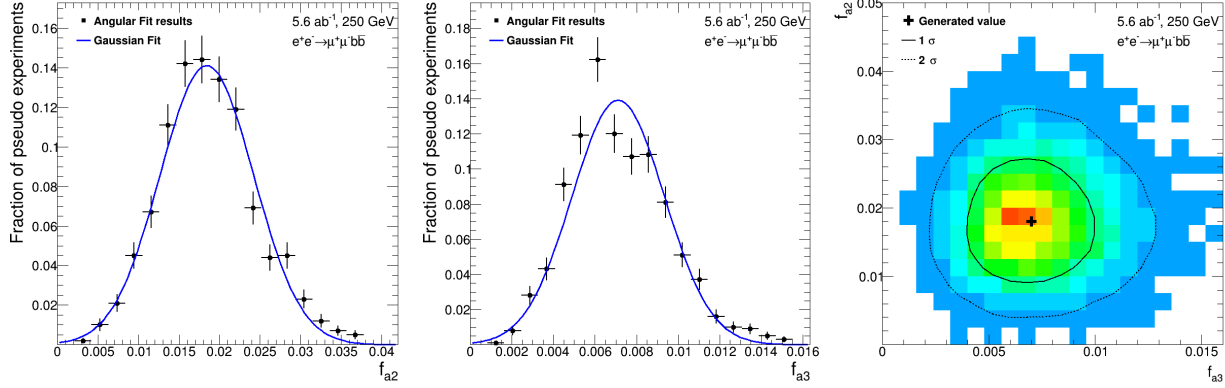


Fig. 29. Distribution of fitted values of  $f_{a2}$  and  $f_{a3}$  in a large number of generated experiments. In the left and middle plots, only the parameter shown is floated. Other parameters are fixed to SM expectations. Right plot: simultaneous fit of non-zero  $f_{a2}$  and  $f_{a3}$ , with 68% and 95% confidence level contours shown.

Compared to the ultimate sensitivity of HL-LHC as shown in Ref. [116], the sensitivities in the  $f_{a2}$  and  $f_{a3}$  at the CEPC are a factor of 300 and 3 better. Further improvements can be achieved by exploring kinematics in the  $H \rightarrow b\bar{b}$  decays, including other  $Z$  decay final states, and combining with the overall cross-section dependence of the signal with a threshold scan in  $\sqrt{s}$ .

## 8.2 Higgs boson exotic decays

Higgs boson can be an important portal to new physics beyond the Standard Model. Such new physics could manifest itself through Higgs boson exotic decays if some of the degrees of freedom are light. The Higgs boson BSM decays have a rich variety of possibilities. Two-body Higgs boson decays into BSM particles  $H \rightarrow X_1 X_2$ , where the BSM particles  $X_i$  are allowed to subsequently decay further, are considered here. These decay modes are classified into four cases, schematically shown in Fig. 30. These processes are well-motivated by BSM models such as singlet extensions of the SM, two-Higgs-doublet-models, SUSY models, Higgs portals, gauge extensions of the SM, and so on [118–120]. In this study, only prompt decays of the BSM particles are considered. For Higgs decays into long-lived particles, novel search strategies can be developed in future studies utilizing the advancement in detector development [121].

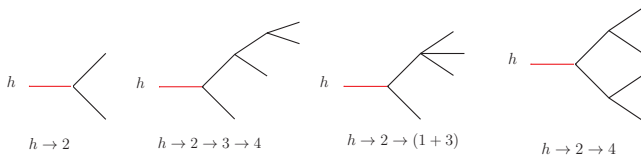


Fig. 30. The topologies of the SM-like Higgs boson exotic decays.

For CEPC running at the center of mass energy 240 GeV, the most important Higgs boson production

mechanism is  $e^+e^- \rightarrow ZH$  production. The  $Z$  boson with visible decays enables Higgs boson tagging using the “recoil mass” technique as described in Section 4. A cut around the peak of the recoil mass spectrum would remove the majority of the SM background. Further selection and tagging on the Higgs boson decay product can hence archive high signal efficiency, and the major background would be from the Higgs boson SM decays. The details of these analysis can be found in Ref. [120].

The set of Higgs boson exotic decays with their projected LHC constraints and limits from the CEPC with  $5.6\text{ab}^{-1}$  integrated luminosity are summarized in Table 17. For the LHC constraints, both the current limits and projected limits on these exotic decay channels from various references are tabulated. The comparison are performed for particular benchmark points to demonstrate the qualitative difference between the (HL-)LHC and CEPC.

In the summary in Table 17 and the corresponding Fig. 31, the exotic Higgs boson decay channels are selected such that they are hard to be constrained at the LHC. The red bars correspond to the results using leptonic decaying  $Z$ -boson that is produced in association with the Higgs boson. The hadronic decaying  $Z$ -boson provides around ten times more statistics and hence further inclusion will definitely improve the results significantly. Based upon the study of the  $H \rightarrow WW^*$ ,  $ZZ^*$  and invisible particles, hadronic decaying  $Z$  bosons are conservatively assumed to provide same upper limit on these channels from leptonic  $Z$  and hence improve the limits by around 40% when combined. This extrapolated results are shown in yellow bars.

In comparison with the HL-LHC, the improvements on the Higgs boson exotic decay branching fractions are significant, varying from one to four orders of magnitude for the channels under consideration. For the Higgs bo-

Table 17. The current and projected limits on Higgs boson exotic decay modes for the (HL-)LHC and CEPC with  $5.6\text{ab}^{-1}$  integrated luminosity, based upon results from Ref. [120]. The projections for the HL-LHC are collected in the third column, where the limits for  $100\text{fb}^{-1}$  and  $300\text{fb}^{-1}$  alone are shown in parentheses and square brackets, respectively.

Decay Mode	95% C.L. limit on BR		
	LHC	HL-LHC	CEPC
$\cancel{E}_T$	0.23	0.056	0.0030
$(b\bar{b}) + \cancel{E}_T$	–	[0.2]	$1 \times 10^{-4}$
$(jj) + \cancel{E}_T$	–	–	$4 \times 10^{-4}$
$(\tau^+\tau^-) + \cancel{E}_T$	–	[1]	$8 \times 10^{-5}$
$b\bar{b} + \cancel{E}_T$	–	[0.2]	$2 \times 10^{-4}$
$jj + \cancel{E}_T$	–	–	$5 \times 10^{-4}$
$\tau^+\tau^- + \cancel{E}_T$	–	–	$8 \times 10^{-5}$
$(b\bar{b})(b\bar{b})$	1.7	(0.2)	$6 \times 10^{-4}$
$(c\bar{c})(c\bar{c})$	–	(0.2)	$8 \times 10^{-4}$
$(jj)(jj)$	–	[0.1]	$2 \times 10^{-3}$
$(b\bar{b})(\tau^+\tau^-)$	[0.1]	[0.15]	$4 \times 10^{-4}$
$(\tau^+\tau^-)(\tau^+\tau^-)$	[1.2]	[0.2 ~ 0.4]	$2 \times 10^{-4}$
$(jj)(\gamma\gamma)$	–	[0.01]	$1 \times 10^{-4}$
$(\gamma\gamma)(\gamma\gamma)$	$[7 \times 10^{-3}]$	$4 \times 10^{-4}$	$8 \times 10^{-5}$

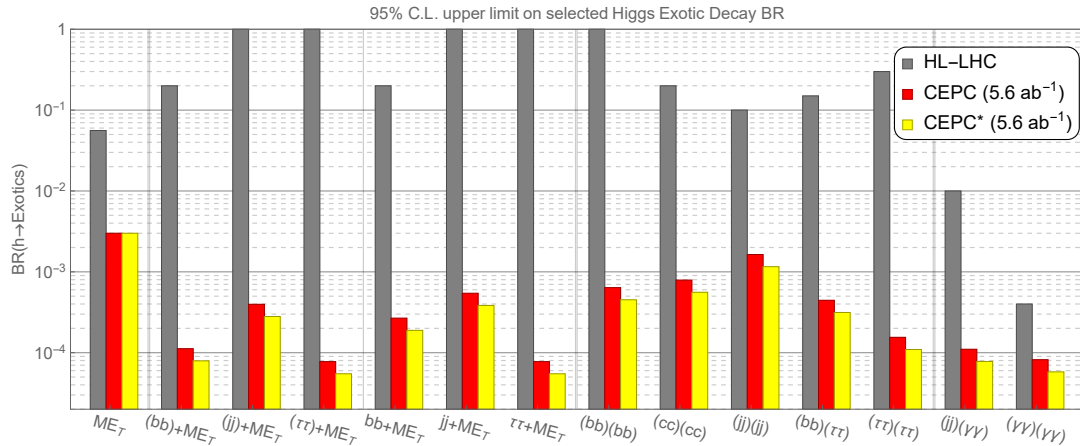


Fig. 31. The 95% C.L. upper limit on selected Higgs boson exotic decay branching fractions at HL-LHC and CEPC, based on Ref. [120]. The benchmark parameter choices are the same as in Table 17. The red bars correspond to the results using leptonically decaying spectator  $Z$ -boson alone. The yellow bars further include extrapolation with the inclusion of the hadronically decaying  $Z$ -bosons. Several vertical lines are drawn in this figure to divide different types of Higgs boson exotic decays.

son exotic decays into hadronic final states plus missing energy,  $b\bar{b} + \cancel{E}_T$ ,  $jj + \cancel{E}_T$  and  $\tau^+\tau^- + \cancel{E}_T$ , CEPC improves on the HL-LHC sensitivity for these channels by three to four orders of magnitude. These significant improvements benefit from low QCD background and the Higgs boson tagging from recoil mass reconstruction at CEPC. As for the Higgs boson exotic decays without missing energy, the comparative improvements vary between two to three orders of magnitude. Reconstructing the Higgs boson mass from the final state particles at the LHC provide additional signal-background discrimination power and hence the improvement from the CEPC on Higgs boson exotic decays without missing energy is significant than those with missing energy in the Higgs boson exotic decays. Moreover, leptons and photons are free from the large QCD background at the LHC and the sensitivity at the HL-LHC on these channels will be very competitive. CEPC complements the HL-LHC for hadronic channels and channels with missing energy.

## 9 Implications

In this section, we briefly discuss the most important physics implications of the Higgs measurements at the CEPC. The measurements of the Higgs boson properties are essential to the understanding of the nature of electroweak symmetry breaking, which remains to be a central and open question in the Standard Model. In the SM, it is parametrized by the so-called ‘‘Mexican Hat’’ Higgs potential,

$$V(H) = -\frac{1}{2}\mu^2|H|^2 + \frac{\lambda}{4}|H|^4, \quad (32)$$

with the vacuum expectation value (VEV) of the Higgs field spontaneously breaking the  $SU(2)_L \times U(1)_Y$  gauge symmetry down to  $U(1)_{\text{em}}$ , and generating masses for the  $W$  and  $Z$  bosons. With the measurements of the Fermi constant (from muon decay) and the Higgs boson mass, the two parameters in Eq. 32,  $\mu^2$  and  $\lambda$ , are determined to very good precisions, and thus the SM Higgs potential is fully determined. However, we would like to emphasize that this simplicity is somewhat misleading, as our knowledge of the electroweak symmetry breaking is far from complete. First of all, even though the values of these parameters can be fixed by the experimental measurement, the SM does not contain an explanation of their sizes, and in particular why the electroweak scale appears to be many orders of magnitude smaller than the Planck scale. Further more, the Mexican Hat potential as well as the SM itself are model assumptions which needs to be explicitly tested by experiments before they are established to be correct. In this section, we will focus on the potential of using precision measurement of Higgs properties at the CEPC to address these important questions.

### 9.1 Naturalness of the electroweak scale

An important question associated with the electroweak symmetry breaking is naturalness. It arises from the need to explain the presence of the weak scale  $\Lambda_{\text{weak}} \sim 10^2$  GeV in terms of a more fundamental theory. New physics is necessarily involved in such a theory, as the SM itself could not answer this question. There are many new physics models which can potentially answer this question. However, a key question for any model of electroweak symmetry breaking, regardless of the model details, is what the scale of new physics is. For instance, if the new physics is the quantum gravity scale,  $M_{\text{Planck}} = 10^{19}$  GeV, then an immediate question is how to explain the 17 orders of magnitude difference between it and the electroweak scale. This is often denoted as the naturalness/hierarchy/fine-tuning problem. More generally, the weak scale in any such model can be expressed using dimensional analysis as

$$\Lambda_{\text{weak}}^2 \sim c_1 M_1^2 + c_2 M_2^2 + \dots, \quad (33)$$

where  $M_i \sim M_{\text{NP}}$  are the scale of new physics. They are typically the masses of the new physics particles. The  $c_i$  are numerical coefficients that depend on the details of the model. However, we do not expect them to be very different from order one. Therefore, a large and precise cancellation is needed if  $M_{\text{NP}} \gg \Lambda_{\text{EW}}$ , with the level of tuning proportional to  $M_{\text{NP}}^2$ . The discovery of the spin-zero Higgs boson deepens this mystery. While it is possible to generate a large cancellation by imposing symmetries instead of tuning – one well-known example is the chiral symmetry which protects the masses of the light fermions from receiving large quantum corrections – there is no obvious symmetry that protects the mass of the Higgs boson if it is an elementary scalar particle. To avoid an excessive amount of fine tuning in the theory, the new physics cannot be too heavy, and should preferably be below the TeV scale. This is the main argument for TeV new physics based on naturalness.

Searching for new physics which leads to a natural electroweak symmetry breaking has been and will continue to be a main part of the physics program at the LHC. Looking for signals from the direct production of the new physics particles, the LHC will probe the new physics scale up to a few TeV. At the same time, as we will show below, the precision measurements at the CEPC can provide competitive reaches, and has the potential of probing significant higher new physics scales for many scenarios. In addition, the reach of the LHC searches has a strong dependence on the production and decay modes of the new physics particles. The measurements at the CEPC thus provides crucial complementary information and can cover some scenarios that the LHC has difficulties to probe. Indeed, the precision measurement of the Higgs couplings offers a very robust way

of probing new physics related to electroweak symmetry breaking. Any such new physics would necessarily contain particles with sizable couplings to the Higgs boson, which leave their imprints in the Higgs couplings. Such a model independent handle is of crucial importance, given the possibility that the new physics could simply be missed by the LHC searches designed based on our wrong expectations of it.

In the following, we demonstrate the potential of probing new physics in several broad classes of models which can address the naturalness of the electroweak symmetry breaking.

One obvious idea is that the Higgs boson is a composite particle instead of an elementary one. After all, many composite light scalars already exist in nature, such as the QCD mesons. The composite Higgs can thus be regarded as a close analogy of the QCD mesons. A light Higgs boson can be naturally obtained if it is implemented as a pseudo-Nambu-Goldstone boson with new dynamics at scale  $f$ . Its physics can be described by a chiral Lagrangian similar to that of the low energy QCD. The explicit breaking comes from the couplings which are responsible for the SM fermion masses, and the SM gauge couplings. In this case, the Higgs boson would not unitarize the  $WW$  scattering amplitude completely, and its coupling to  $W$  and  $Z$  will be shifted approximately by

$$\delta\kappa_W, \delta\kappa_Z \sim \mathcal{O}\left(\frac{v^2}{f^2}\right). \quad (34)$$

Therefore, the measurement of  $\kappa_Z$  provides a strong and robust constraint on  $f$ . Taking the results of the 10-parameter fit in Table 7.1, a precision of 0.21% on  $\kappa_Z$  implies that values of  $f$  below 2.7 GeV are excluded at 95% CL. For specific models, an even stronger bound on  $f$ , up to around 5 TeV, can be obtained by exploiting also its contributions to other Higgs couplings [123]. The masses of the composite resonances are given by  $m_\rho \sim g_\rho f$ , where  $g_\rho$  is the coupling of the new strong interaction, with a size typically much larger than one. This indicates that the CEPC has the potential to probe composite resonance scales much above 10 TeV, which is far beyond the reach of the LHC direct searches. The Higgs measurements at the CEPC thus provides a strong and robust test of the idea of naturalness in the composite Higgs models.

Due to the large Higgs boson coupling to the top quark, arguably the most important particle in addressing the naturalness problem is the top partner. For example, in supersymmetric models (SUSY), the particle mainly responsible for stabilizing the electroweak scale is the scalar top,  $\tilde{t}$ . The presence of stop will modify the Higgs couplings via a loop contribution, which is most notable for the  $Hgg$  and  $H\gamma\gamma$  couplings since they are also generated at one-loop order in the SM. The domi-

nant effect is on the  $Hgg$  coupling,

$$\kappa_g - 1 \simeq \frac{m_t^2}{4m_{\tilde{t}}^2}. \quad (35)$$

The measurement of  $\kappa_g$  at the CEPC, up to 1% accuracy, will allow us to probe stop mass up to 900 GeV [124, 125]. The situation is also very similar for non-SUSY models with fermionic top partners, with the bounds on the top partner mass being even stronger than the stop one [125]. The more detailed exclusion region in the top partner parameter space is presented in Fig. 33 for both scenarios.

This gives us another important handle to test the idea of naturalness. We note that, in favorable cases, the search of stop at the LHC run 2 can set a stronger limit on the stop mass. However, this limit depends strongly on the assumption of the mass spectrum of the other superpartners, as well as the relevant decay modes of the stop. As a result, there will still be significant gaps remaining in the parameter space after the upcoming runs of the LHC, and even very light stops cannot be completely excluded. On the other hand, the measurement of the  $Hgg$  coupling offers a complementary way of probing the stop that is independent of the decay modes of the stop.

It is also possible that the top partner does not have the same SM gauge quantum numbers as the top quark. A particularly interesting possibility is that the top partner is a SM singlet. In such scenarios, it is very difficult to search for the top partner at the LHC. It is nontrivial to construct models with SM-singlet top partners that resolve the fine-tuning problem of the electroweak scale [127, 128]. Nevertheless, they offer an extreme example that new physics with a scale of a few hundred GeVs could still be alive after the current and future LHC runs. However, as mentioned earlier, any model that addresses the electroweak naturalness problem would inevitably contain sizable couplings to the Higgs boson. The Higgs coupling measurements at the CEPC thus offer an ideal way of testing this type of models, which is very important for making robust arguments on the naturalness problem. As an example, we consider a scalar top partner  $\phi_t$  with its only interaction to the SM fields given by  $H^\dagger H \phi_t^\dagger \phi_t$  [126, 129]. This interaction contributes to the Higgs propagator at one-loop level, and induces a universal shift to all Higgs couplings. The precise measurement of the inclusive  $ZH$  cross section imposes a strong constraint on  $\kappa_Z$  and provides the best reach on the mass of the top partner,  $m_\phi$ . As we can see from the left panel of Fig. 34, the CEPC will be able to probe  $m_\phi$  up to around 700 GeV, giving a non-trivial test of naturalness even in this very difficult scenario. A more concrete model is the so-called “folded SUSY”, in which the top partners are scalars analogous to the stops in SUSY. The projected constraints in the folded

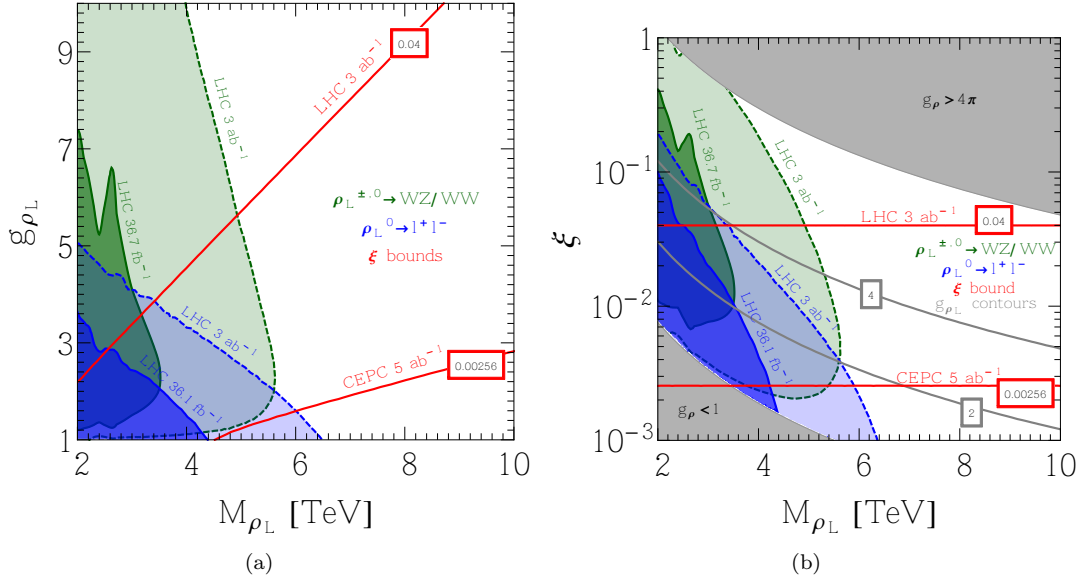


Fig. 32. Limits on the composite Higgs model from both direct searches at the LHC and precision measurement at the CEPC. The figures are updated versions of the ones presented in Ref. [122]

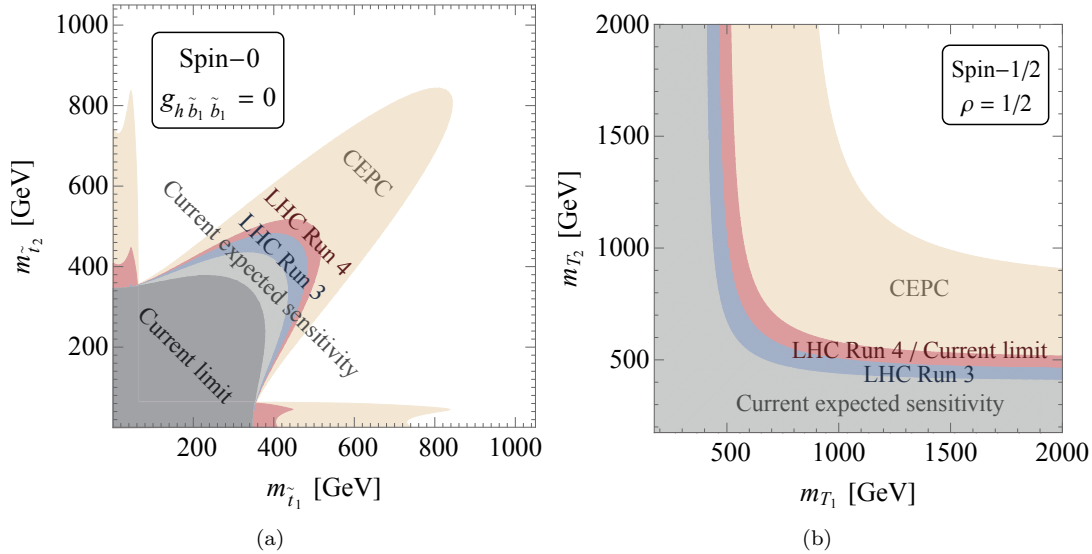


Fig. 33. 95% CL Limits on the stop (a) and fermionic top partner (b) from Higgs coupling measurements at various current and future collider scenarios, including the CEPC. This figure is reproduced from Ref. [125].

stop mass plane is shown on in the right panel of Fig. 34, which are at least around 350 GeV for both stops.

## 9.2 Electroweak phase transition

The measurement of the properties of the Higgs boson at the LHC has been consistent with the SM so far. At the same time, the nature of the electroweak phase transition remains unknown. While we have a very good knowledge of the sizes of the electroweak VEV and the

Higgs mass, they only allows us to uncover a small region of the Higgs potential near the vacuum, and the global picture of the Higgs potential is largely undetermined. This is shown schematically in Fig. 35.

The remaining region of the Higgs potential is difficult to probe, even with an upgraded LHC. Meanwhile, it has important consequences on the early universe cosmology and the understanding of our observable world. For example, it is crucial in determining whether the

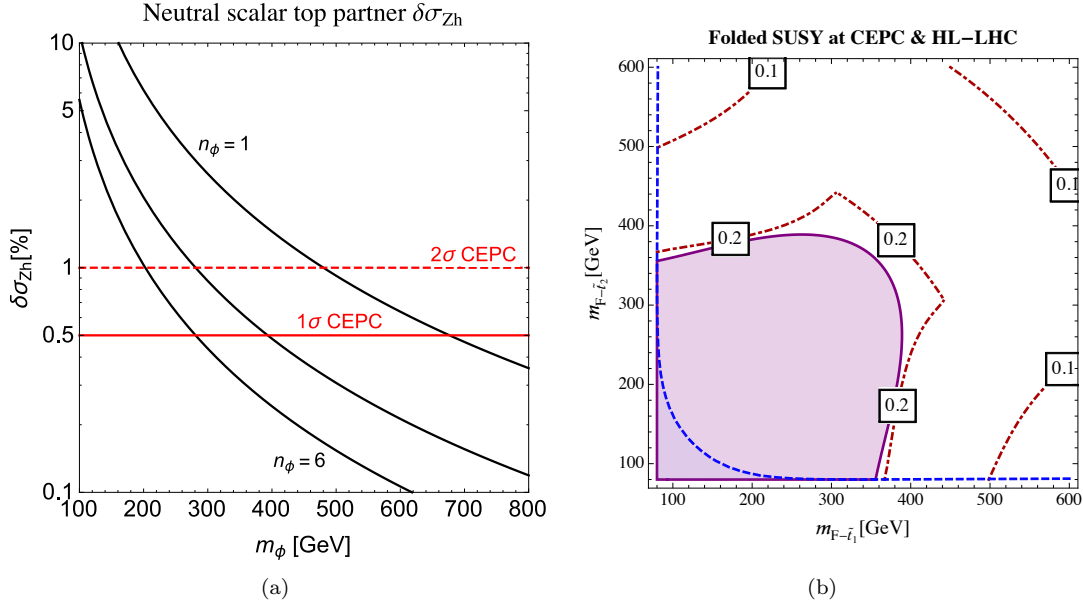


Fig. 34. (a) The fractional deviation of  $\sigma_{ZH}$  at the Higgs factory in the scalar singlet top partner model with the  $H^\dagger H \phi_t^\dagger \phi_t$  interaction, reproduced from Ref. [126]. (b) Projected constraints in the folded stop mass plane from the  $H\gamma\gamma$  coupling measurements at HL-LHC and CEPC, reproduced from Ref. [124]. The dot-dashed red contours indicates the fine-tuning in the Higgs mass from the quadratic sensitivity to stop soft terms.

electroweak phase transition is of first order or second one. The nature of the electroweak phase transition can also be relevant for the matter anti-matter asymmetry in the Universe, as a large class of models of baryogenesis rely on a first order electroweak phase transition. The CEPC has the capability of probing many of these models and potentially revealing the nature of the electroweak phase transition and the origin of baryogenesis.

It is well known that, under the assumption of a minimal Higgs potential and the Higgs sector of the SM, the electroweak phase transition is of second order. New physics with sizable couplings to the Higgs boson are needed to make the phase transition a first order one. The measurement of the triple Higgs coupling offers an ideal testing ground for these new physics models. Being the third derivative, it carries more information about the global shape of the Higgs potential than the mass. It can also be determined to a reasonable precision at the future colliders, unlike the quartic Higgs coupling. Indeed, most models with first order electroweak phase transition predict a triple Higgs coupling with large deviations from the SM prediction. This is demonstrated with a simple example in Fig. 36, which shows the deviation in the Higgs boson self-coupling for a generic singlet model. For the model points that produces a first order phase transition, the value of triple Higgs coupling indeed covers a wide range and can be different from the SM prediction by up to 100%.

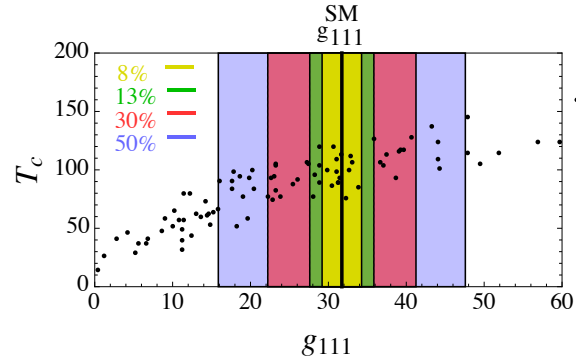


Fig. 36. The deviation in the Higgs boson self-coupling in a generic singlet model that could produce first order electroweak phase transition, reproduced from Ref. [130]. Black dots are points where the phase transition is of first order.  $g_{111}$  is the triple Higgs boson coupling.

The CEPC could probe the triple Higgs coupling via its loop contributions to single Higgs processes. As pointed out in Section 7.3, it will have a limited reach in the most general scenario where all Higgs couplings are allowed to deviate from SM values. An additional run at 350 GeV helps improve the reach, while a direct measurement using the double-Higgs processes would have to wait for a future proton proton collider, or a lepton collider running at much higher energies. However, it should be noted that the model independent approach

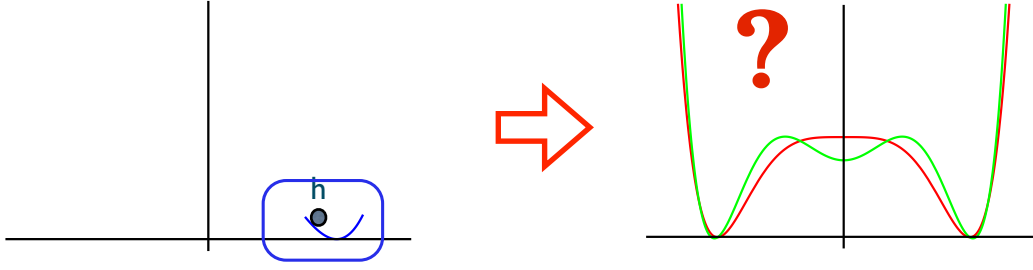


Fig. 35. A schematic drawing illustrating the question of the nature of the electroweak phase transition. **Left:** Our current knowledge of the Higgs potential. **Right:** Based on our current knowledge, we could not distinguish the SM Mexican Hat potential from an alternative one with more wiggles.

in Section 7.3 makes no assumption on any possible connection between the triple Higgs coupling and other couplings. In practice, to induce large deviation in triple Higgs coupling requires the new physics to be close to the weak scale, while the presence of such new physics will most likely induce deviations in other Higgs couplings as well, such as the couplings to the electroweak gauge bosons. Without some symmetry or fine tuning, both deviations are expected to come in at the order of  $v^2/M_{\text{NP}}^2$ . Such deviations can be probed very well at lepton colliders.

We will now demonstrate this in the context of models. Instead of a comprehensive survey, we will focus here on some of the simplest possibilities which are also difficult to probe. The minimal model that has been well studied in this class introduces an additional singlet scalar which couples to the Higgs boson [130–135]. The general potential of the Higgs boson and the new scalar  $S$  is

$$V(H, S) = \frac{1}{2}\mu^2|H|^2 + \frac{\lambda}{4}|H|^4 + m_S^2 S^2 + \tilde{a}S|H|^2 + \tilde{\kappa}S^2|H|^2 + \tilde{b}S^3 + \lambda_S S^4. \quad (36)$$

After integrating out the singlet, it will generate an  $|H|^6$  interaction (shown in panel (a) in Fig. 37), which, after electroweak symmetry breaking, leads to a modification of the triple Higgs coupling on the order of  $v^2/m_S^2$ . At the same time, it will also generate the operator  $|H^\dagger \partial H|^2$ . This leads to a wave function renormalization, which gives rises to universal shift of the Higgs couplings. In particular, the modification of the  $HZZ$  coupling is also of order  $\sim v^2/m_S^2$ . We thus expect  $\kappa_Z$ , which is constrained within 0.25% even with the inclusive  $ZH$  measurement alone, to provide the best constraining power on this model. This is explicitly verified with a scan in the model parameter space, shown in Fig. 38. The model points with a first order phase transition are projected on the plane of the  $HZZ$  and triple Higgs couplings. Indeed, for model points with a large deviation in the triple Higgs coupling, a sizable deviation in the  $HZZ$  coupling

is also present. In this model, constraining power of the  $HZZ$  coupling measurement at CEPC is almost the same as the triple Higgs coupling measurement at a future 100 TeV hadron collider. A more detailed view of the parameter space of the real singlet model is presented in Fig. 39. In addition to the deviations in  $\sigma(ZH)$  at CEPC, the sensitivities of the current and future electroweak precision tests are also presented [136]. The  $\sigma(ZH)$  measurement, with a projected precision of 0.5%, indeed provides the best sensitivity in this scenario. We thus conclude that CEPC has an excellent coverage in the full model space that gives a first order electroweak phase transition.

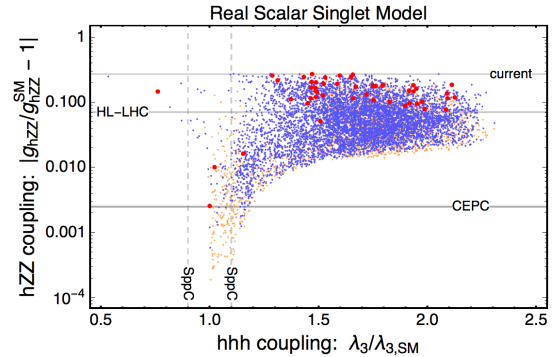


Fig. 38. The  $HZZ$  and  $HHH$  couplings in the real scalar singlet model of Eq. 36. The points in this figure represent models with a first order electroweak phase transition, and are obtained by scanning over the theory space. Points with a first order phase transition are shown in orange, points with a strongly first order phase transition are shown in blue, and points with a strongly first order phase transition that also produces detectable gravitational waves are shown in red. This figure is reproduced from Ref. [137].

A more restricted scenario, in which a discrete  $Z_2$  symmetry is imposed on the singlet, has also been considered [131, 135]. It is significantly more difficult to achieve a first order electroweak phase transition in this scenario,

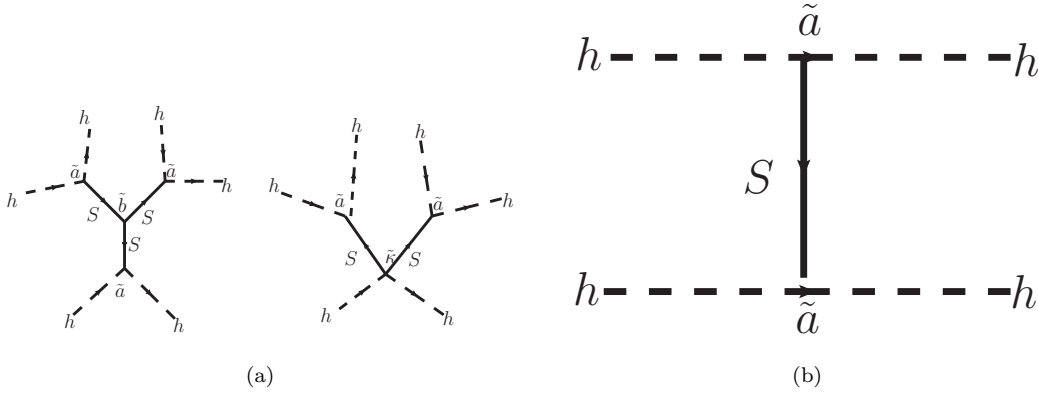


Fig. 37. (a) Induced  $|H|^6$  couplings after integrating out the singlet. (b) Induced wave function renormalization of the Higgs,  $|H^\dagger \partial H|^2$ .

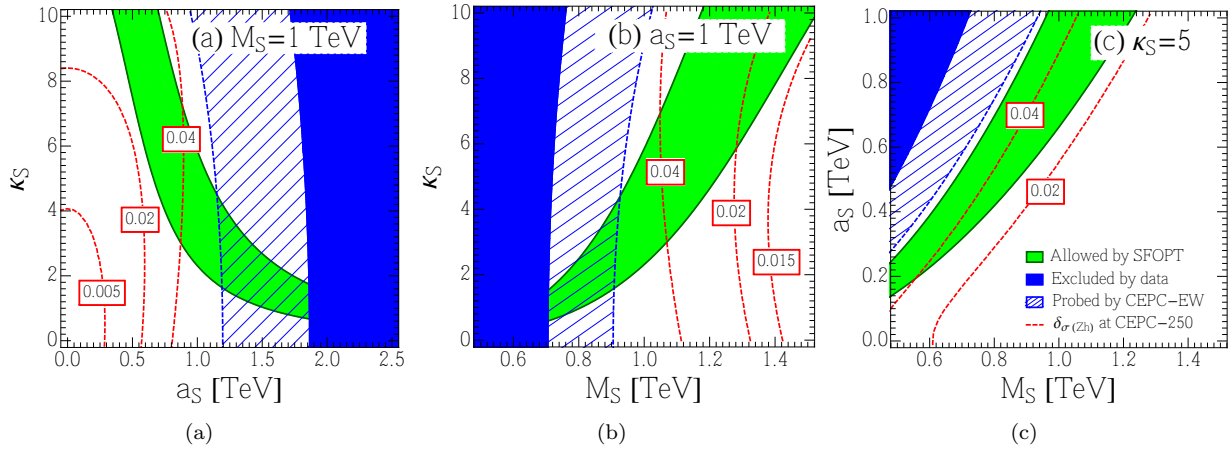


Fig. 39. The parameter space compatible with a strong first order phase transition (green region) and the deviations in  $\sigma(ZH)$  (dashed red contours) in the real singlet scalar model, reproduced from Ref. [136]. The solid blue region is excluded by current EW and Higgs data, and the region with dashed blue lines can be probed by the CEPC Z-pole run.

since the singlet could only modify the Higgs potential at loop levels. To produce the same level of deviation in the Higgs potential, a much stronger coupling between the Higgs boson and the singlet is required, which often exceeds the limits imposed by the requirement of perturbativity. For the same reason, the expected loop induced deviation in the triple Higgs coupling is also generically smaller in this case, and is about 10–15%, as shown in Fig. 40(a). Even in this difficult case, we see in Fig. 40(b) that the expected deviation of the cross section  $\sigma(ZH)$  is about 0.6%. Therefore, the CEPC will see the first evidence of new physics even in this very difficult case. In the more general classes of models, the new physics which modifies the Higgs boson coupling could carry other SM gauge quantum numbers, such as electric charge and/or color. In such cases, there will be significant modifica-

tions to the  $Hgg$  and  $H\gamma\gamma$  couplings. One such example is shown in Fig. 40(c), with a 6% deviation in the  $H\gamma\gamma$  coupling expected in order to obtain a first order phase transition. As shown in Table 7.1, the combination of CEPC and HL-LHC measurements could constrain  $\kappa_\gamma$  to a precision of 1.7%, and would test this scenario with a sensitivity of more than three standard deviations.

In general, the newly discovered Higgs particle could serve as a gateway to new physics. One generic form of the Higgs boson coupling to new physics is the so-called Higgs portal,  $H^\dagger H \mathcal{O}_{NP}$ , where  $\mathcal{O}_{NP}$  is an operator composed out of new physics fields. Since  $H^\dagger H$  is the lowest dimensional operator that is consistent with all the symmetries in the Standard Model, it is easy to construct scenarios in which such Higgs portal couplings are the most relevant ones for the low energy phenomenol-

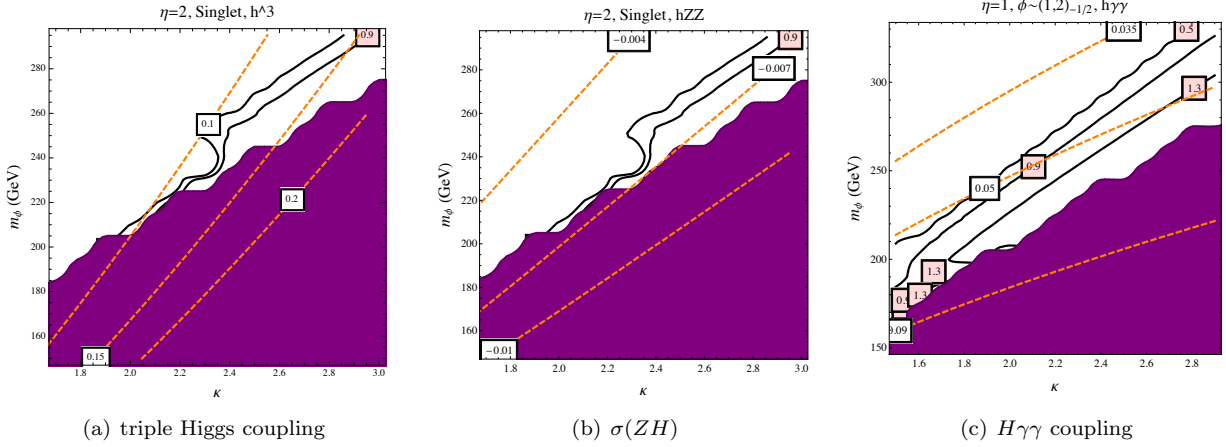


Fig. 40. Deviations in the triple Higgs,  $\sigma(ZH)$  and  $H\gamma\gamma$  couplings in models with  $Z_2$  symmetry. In each plot, the dashed orange lines are contours of constant deviations in the corresponding quantity, the solid black lines are contours of constant electroweak phase transition strength parameter  $\xi = v(T_c)/T_c$ , where  $v(T_c)$  is the Higgs VEV at temperature  $T_c$ . The shaded region is excluded for producing a color-breaking vacuum.

ogy of new physics. The singlet extended Higgs sector and the scalar top partner, discussed earlier, are special examples of this scenario. In general, the Higgs portal interactions will shift the Higgs boson couplings, and can be thoroughly tested at the CEPC. Moreover, if the new physics is lighter than  $m_H/2$ , the Higgs portal coupling will lead to new Higgs decay channels. We have already seen in Section 8.2 that the CEPC has an excellent capability of probing such exotic decays, and could cover a vast range of decay signals.

## 10 Conclusion

The Higgs boson is responsible for the electroweak symmetry breaking. It is the only fundamental scalar particle in the Standard Model observed so far. The discovery of such a particle at the LHC is a major breakthrough on both theoretical and experimental fronts. However, the Standard Model is likely only an effective theory at the electroweak scale. To explore potential new physics at the electroweak scale and beyond, complementary approaches of direct searches at the energy frontier as well as precision measurements will be needed. The current LHC and the planned HL-LHC have the potential to significantly extend its new physics reach and to measure many of the Higgs boson couplings with preci-

sion of a few percents.

However, many new physics models predict Higgs boson coupling deviations at the sub-percent level, beyond those achievable at the LHC. The CEPC complements the LHC and will be able to study the properties of the Higgs boson in great details with unprecedented precision. Therefore it is capable of unveiling the true nature of this particle. At the CEPC, most Higgs boson couplings can be measured with precision at a sub-percent level. More importantly, the CEPC will be able to measure many of the key Higgs boson properties such as the total width and decay branching ratios model independently, greatly enhancing the coverage of new physics searches. Furthermore, the clean event environment of the CEPC will allow the detailed study of known decay modes and the identification of potential unknown decay modes that are impractical to test at the LHC.

This paper provides a snapshot of the current studies, many of them are ongoing and more analyses are needed to fully understand the physics potential of the CEPC. Nevertheless, the results presented here have already built a strong case for the CEPC as a Higgs factory. The CEPC has the potential to “undress” the Higgs boson as what the LEP has done to the  $Z$  boson, and shed light on new physics.

## References

- 1 ATLAS Collaboration, *Observation of a new particle in the search for the Standard Model Higgs boson with the ATLAS detector at the LHC*, *Phys. Lett. B* **716** (2012) 1–29, [arXiv:1207.7214 \[hep-ex\]](#).
- 2 CMS Collaboration, *Observation of a new boson at a mass of 125 GeV with the CMS experiment at the LHC*, *Phys. Lett. B* **716** (2012) 30–61, [arXiv:1207.7235 \[hep-ex\]](#).
- 3 ATLAS Collaboration, *Measurements of Higgs boson production and couplings in diboson final states with the ATLAS detector at the LHC*, *Phys. Lett. B* **726** (2013) 88–119, [arXiv:1307.1427 \[hep-ex\]](#). [Erratum: *Phys. Lett. B* **734**, 406(2014)].
- 4 ATLAS Collaboration, *Evidence for the spin-0 nature of the Higgs boson using ATLAS data*, *Phys. Lett. B* **726** (2013) 120–144, [arXiv:1307.1432 \[hep-ex\]](#).
- 5 CMS Collaboration, *Observation of a new boson with mass near 125 GeV in pp collisions at  $\sqrt{s} = 7$  and 8 TeV*, *JHEP* **1306** (2013) 081, [arXiv:1303.4571 \[hep-ex\]](#).
- 6 CMS Collaboration, *Evidence for the direct decay of the 125 GeV Higgs boson to fermions*, *Nature Phys.* **10** (2014) , [arXiv:1401.6527 \[hep-ex\]](#).
- 7 CMS Collaboration, *Constraints on the spin-parity and anomalous HVV couplings of the Higgs boson in proton collisions at 7 and 8 TeV*, *Phys. Rev. D* **92** (2015) 012004, [arXiv:1411.3441 \[hep-ex\]](#).
- 8 ATLAS and CMS Collaborations, *Measurements of the Higgs boson production and decay rates and constraints on its couplings from a combined ATLAS and CMS analysis of the LHC pp collision data at  $\sqrt{s} = 7$  and 8 TeV*, *JHEP* **08** (2016) 045, [arXiv:1606.02266 \[hep-ex\]](#).
- 9 ATLAS and CMS Collaborations, *Combined Measurement of the Higgs Boson Mass in pp Collisions at  $\sqrt{s} = 7$  and 8 TeV with the ATLAS and CMS Experiments*, *Phys. Rev. Lett.* **114** (2015) 191803, [arXiv:1503.07589 \[hep-ex\]](#).
- 10 P. Glaysher, *ATLAS Higgs physics prospects at the high luminosity LHC*, vol. EPS-HEP2015, p. 160. Proceedings, 2015 European Physical Society Conference on High Energy Physics (EPS-HEP 2015): Vienna, Austria, July 22-29, 2015.
- 11 *CEPC Conceptual Design Report - Detector and Physics*, [arXiv:xxxx.xxxx](#).
- 12 ILD Concept Group - Linear Collider Collaboration, *The International Large Detector: Letter of Intent*, [arXiv:1006.3396 \[hep-ex\]](#).
- 13 T. Behnke, J. E. Brau, P. N. Burrows, J. Fuster, M. Peskin, et al., *The International Linear Collider Technical Design Report - Volume 4: Detectors*, [arXiv:1306.6329 \[physics.ins-det\]](#).
- 14 CEPC-SPPC Study Group, *CEPC-SPPC Preliminary Conceptual Design Report. 1. Physics and Detector* (2015) . [http://cepc.ihep.ac.cn/preCDR/volume.html](#).
- 15 P. Janot, *Particle Flow Event Reconstruction from LEP to LHC*, Presented at Excellence in Detectors and Instrumentation Technologies workshop, CERN (2011). [https://indico.cern.ch/event/96989/contribution/15](#).
- 16 M. Minard, *Jet energy measurement with the ALEPH detector at LEP2*, Presented at CALOR2002 Conference, Pasadena, California, USA (2002). [http://inspirehep.net/record/608013](#).
- 17 M. Thomson, *Particle Flow Calorimetry and the PandoraPFA Algorithm*, *Nucl. Instrum. Meth. A* **611** (2009) 25, [arXiv:0907.3577 \[physics.ins-det\]](#).
- 18 M. Ruan and H. Videau, *Arbor, a new approach of the Particle Flow Algorithm*, [arXiv:1403.4784 \[physics.ins-det\]](#).
- 19 CMS Collaboration, *Particle-Flow Event Reconstruction in CMS and Performance for Jets, Taus, and MET*, CMS-PAS-PFT-09-001 (2009) . [http://cds.cern.ch/record/1194487](#).
- 20 F. Beaudette, *The CMS Particle Flow Algorithm*, pp. 295–304. Proceedings, International Conference on Calorimetry for the High Energy Frontier (CHEF 2013): Paris, France, April 22-25, 2013. [arXiv:1401.8155 \[hep-ex\]](#).
- 21 P. Mora de Freitas and H. Videau, *Detector simulation with MOKKA / GEANT4: Present and future*, Presented at the International Workshop on physics and experiments with future electron-positron linear colliders, Jeju Island, Korea (2002). [http://inspirehep.net/record/609687](#).
- 22 S. Agostinelli et al., *GEANT4: A Simulation toolkit*, *Nucl. Instrum. Meth. A* **506** (2003) 250.
- 23 M. Ruan et al., *Reconstruction of physics objects at the Circular Electron Positron Collider with Arbor*, *Eur. Phys. J. C* **78** (2018) 426.
- 24 H. Zhao, Y.-F. Zhu, C.-D. Fu, D. Yu, and M.-Q. Ruan, *The Higgs Signatures at the CEPC CDR Baseline*, [arXiv:1806.04992 \[hep-ex\]](#).
- 25 D. Yu, M. Ruan, V. Boudry, and H. Videau, *Lepton identification at particle flow oriented detector for the future  $e^+e^-$  Higgs factories*, *Eur. Phys. J. C* **77** (2017) 591, [arXiv:1701.07542 \[physics.ins-det\]](#).
- 26 S. Catani, Y. L. Dokshitzer, M. Olsson, G. Turnock, and B. Webber, *New clustering algorithm for multi-jet cross-sections in  $e^+e^-$  annihilation*, *Phys. Lett. B* **269** (1991) 432.
- 27 T. Tanabe and T. Suehara, *LCFIPlus*, Presented at ILD workshop at Kyushu University (2012). [https://agenda.linearcollider.org/event/5496/session/1/contribution/16](#).
- 28 LHC Higgs Cross Section Working Group, *Handbook of LHC Higgs Cross Sections: 1. Inclusive Observables*, [arXiv:1101.0593 \[hep-ph\]](#).
- 29 LHC Higgs Cross Section Working Group, *Handbook of LHC Higgs Cross Sections: 2. Differential Distributions*, [arXiv:1201.3084 \[hep-ph\]](#).
- 30 W. Kilian, T. Ohl, and J. Reuter, *WHIZARD: Simulating Multi-Particle Processes at LHC and ILC*, *Eur. Phys. J. C* **71** (2011) 1742, [arXiv:0708.4233 \[hep-ph\]](#).
- 31 S. Aplin, J. Engels, and F. Gaede, *A production system for massive data processing in ILCSofT*, . [http://inspirehep.net/record/889841](#).
- 32 D. Asner, T. Barklow, C. Calancha, K. Fujii, N. Graf, et al., *ILC Higgs White Paper*, [arXiv:1310.0763 \[hep-ph\]](#).
- 33 Y. Haddad, *Feasibility of a minimum bias analysis of  $e^+e^- \rightarrow ZH \rightarrow q\bar{q} + X$  at a 250 GeV ILC*, [arXiv:1404.3164 \[hep-ph\]](#).
- 34 M. Oreglia, *A Study of the Reactions  $\psi' \rightarrow \gamma\gamma\psi$* , SLAC-R-0236 (1980) . [http://www.slac.stanford.edu/cgi-wrap/getdoc/slac-r-23\6.pdf](#).
- 35 ATLAS Collaboration, *Observation of  $H \rightarrow b\bar{b}$  decays and VH production with the ATLAS detector*, Submitted to: *Phys. Lett. B* (2018) , [arXiv:1808.08238 \[hep-ex\]](#).
- 36 CMS Collaboration, *Observation of Higgs boson decay to bottom quarks*, Submitted to: *Phys. Rev. Lett.* (2018) , [arXiv:1808.08242 \[hep-ex\]](#).
- 37 LHC Higgs Cross Section Working Group, *Handbook of LHC Higgs Cross Sections: 3. Higgs Properties*, [arXiv:1307.1347 \[hep-ph\]](#).
- 38 X. Chen and Y. Wu, *Search for CP violation effects in the  $h \rightarrow \tau\tau$  decay with  $e^+e^-$  colliders*, *Eur. Phys. J. C* **77** (2017) 697, [arXiv:1703.04855 \[hep-ph\]](#).
- 39 R. E. Shrock and M. Suzuki, *Invisible Decays of Higgs Bosons*, *Phys. Lett. B* **110B** (1982) 250.
- 40 K. Griest and H. E. Haber, *Invisible Decays of Higgs Bosons in Supersymmetric Models*, *Phys. Rev. D* **37** (1988) 719.

- 41 C. Englert, T. Plehn, D. Zerwas, and P. M. Zerwas, *Exploring the Higgs portal*, *Phys. Lett.* **B703** (2011) 298–305, [arXiv:1106.3097 \[hep-ph\]](#).
- 42 C. Bonilla, J. W. F. Valle, and J. C. Romo, *Neutrino mass and invisible Higgs decays at the LHC*, *Phys. Rev.* **D91** (2015) 113015, [arXiv:1502.01649 \[hep-ph\]](#).
- 43 ALEPH, DELPHI, L3, OPAL, LEP Electroweak Collaboration, *Electroweak Measurements in Electron-Positron Collisions at W-Boson-Pair Energies at LEP*, *Phys. Rept.* **532** (2013) 119, [arXiv:1302.3415 \[hep-ex\]](#).
- 44 J. Gao, *Probing light-quark Yukawa couplings via hadronic event shapes at lepton colliders*, *JHEP* **01** (2018) 038, [arXiv:1608.01746 \[hep-ph\]](#).
- 45 LHC Higgs Cross Section Working Group, *LHC HXSWG interim recommendations to explore the coupling structure of a Higgs-like particle*, [arXiv:1209.0040 \[hep-ph\]](#).
- 46 S. Dawson, A. Gribsan, H. Logan, J. Qian, C. Tully, et al., *Working Group Report: Higgs Boson*, [arXiv:1310.8361 \[hep-ex\]](#).
- 47 L. J. Dixon and Y. Li, *Bounding the Higgs Boson Width Through Interferometry*, *Phys. Rev. Lett.* **111** (2013) 111802, [arXiv:1305.3854 \[hep-ph\]](#).
- 48 J. Campbell, M. Carena, R. Harnik, and Z. Liu, *Interference in the  $gg \rightarrow h \rightarrow \gamma\gamma$  On-Shell Rate and the Higgs Boson Total Width*, *Phys. Rev. Lett.* **119** (2017) 181801, [arXiv:1704.08259 \[hep-ph\]](#). [Addendum: *Phys. Rev. Lett.* 119, no. 19, 199901 (2017)].
- 49 ATLAS Collaboration, *Projections for measurements of Higgs boson signal strengths and coupling parameters with the ATLAS detector at a HL-LHC*, ATL-PHYS-PUB-2014-016 (2014). <http://cds.cern.ch/record/1956710>.
- 50 CMS Collaboration, *Search for the associated production of the Higgs boson with a top-quark pair*, *JHEP* **1409** (2014) 087, [arXiv:1408.1682 \[hep-ex\]](#).
- 51 ATLAS Collaboration, *Search for  $H \rightarrow \gamma\gamma$  produced in association with top quarks and constraints on the Yukawa coupling between the top quark and the Higgs boson using data taken at 7 TeV and 8 TeV with the ATLAS detector*, *Phys. Lett.* **B740** (2015) 222, [arXiv:1409.3122 \[hep-ex\]](#).
- 52 A. Banfi, A. Martin, and V. Sanz, *Probing top-partners in Higgs+jets*, *JHEP* **1408** (2014) 053, [arXiv:1308.4771 \[hep-ph\]](#).
- 53 A. Azatov and A. Paul, *Probing Higgs couplings with high  $p_T$  Higgs production*, *JHEP* **1401** (2014) 014, [arXiv:1309.5273 \[hep-ph\]](#).
- 54 C. Grojean, E. Salvioni, M. Schlaffer, and A. Weiler, *Very boosted Higgs in gluon fusion*, *JHEP* **1405** (2014) 022, [arXiv:1312.3317 \[hep-ph\]](#).
- 55 M. Buschmann, C. Englert, D. Goncalves, T. Plehn, and M. Spannowsky, *Resolving the Higgs-Gluon Coupling with Jets*, *Phys. Rev.* **D90** (2014) 013010, [arXiv:1405.7651 \[hep-ph\]](#).
- 56 J. Ellis, V. Sanz, and T. You, *Complete Higgs Sector Constraints on Dimension-6 Operators*, *JHEP* **1407** (2014) 036, [arXiv:1404.3667 \[hep-ph\]](#).
- 57 T. Han, Z. Liu, and J. Sayre, *Potential Precision on Higgs Couplings and Total Width at the ILC*, *Phys. Rev.* **D89** (2014) 113006, [arXiv:1311.7155 \[hep-ph\]](#).
- 58 M. Klute, R. Lafaye, T. Plehn, M. Rauch, and D. Zerwas, *Measuring Higgs Couplings at a Linear Collider*, *Europhys. Lett.* **101** (2013) 51001, [arXiv:1301.1322 \[hep-ph\]](#).
- 59 M. E. Peskin, *Estimation of LHC and ILC Capabilities for Precision Higgs Boson Coupling Measurements*, [arXiv:1312.4974 \[hep-ph\]](#).
- 60 K. Fujii et al., *Physics Case for the 250 GeV Stage of the International Linear Collider*, [arXiv:1710.07621 \[hep-ex\]](#).
- 61 T. Barklow, K. Fujii, S. Jung, R. Karl, J. List, T. Ogawa, M. E. Peskin, and J. Tian, *Improved Formalism for Precision Higgs Coupling Fits*, [arXiv:1708.08912 \[hep-ph\]](#).
- 62 A. Denner, S. Heinemeyer, I. Puljak, D. Rebuszi, and M. Spira, *Standard Model Higgs-Boson Branching Ratios with Uncertainties*, *Eur. Phys. J.* **C71** (2011) 1753, [arXiv:1107.5909 \[hep-ph\]](#).
- 63 L. G. Almeida, S. J. Lee, S. Pokorski, and J. D. Wells, *Study of the standard model Higgs boson partial widths and branching fractions*, *Phys. Rev.* **D89** (2014) 033006, [arXiv:1311.6721 \[hep-ph\]](#).
- 64 G. P. Lepage, P. B. Mackenzie, and M. E. Peskin, *Expected Precision of Higgs Boson Partial Widths within the Standard Model*, [arXiv:1404.0319 \[hep-ph\]](#).
- 65 C. Bernaciak, T. Plehn, P. Schichtel, and J. Tattersall, *Spying an invisible Higgs boson*, *Phys. Rev.* **D91** (2015) 035024, [arXiv:1411.7699 \[hep-ph\]](#).
- 66 J. Ellis and T. You, *Sensitivities of Prospective Future  $e+e-$  Colliders to Decoupled New Physics*, *JHEP* **03** (2016) 089, [arXiv:1510.04561 \[hep-ph\]](#).
- 67 J. Ellis, P. Roloff, V. Sanz, and T. You, *Dimension-6 Operator Analysis of the CLIC Sensitivity to New Physics*, [arXiv:1701.04804 \[hep-ph\]](#).
- 68 G. Durieux, C. Grojean, J. Gu, and K. Wang, *The leptonic future of the Higgs*, *JHEP* **09** (2017) 014, [arXiv:1704.02333 \[hep-ph\]](#).
- 69 T. Barklow, K. Fujii, S. Jung, M. E. Peskin, and J. Tian, *Model-Independent Determination of the Triple Higgs Coupling at  $e^+e^-$  Colliders*, [arXiv:1708.09079 \[hep-ph\]](#).
- 70 S. Di Vita, G. Durieux, C. Grojean, J. Gu, Z. Liu, G. Panico, M. Riembau, and T. Vantalon, *A global view on the Higgs self-coupling at lepton colliders*, *JHEP* **02** (2018) 178, [arXiv:1711.03978 \[hep-ph\]](#).
- 71 W. H. Chiu, S. C. Leung, T. Liu, K.-F. Lyu, and L.-T. Wang, *Probing 6D operators at future  $e^-e^+$  colliders*, *JHEP* **05** (2018) 081, [arXiv:1711.04046 \[hep-ph\]](#).
- 72 M. Beneke, D. Boito, and Y.-M. Wang, *Anomalous Higgs couplings in angular asymmetries of  $H \rightarrow Z\ell^+\ell^-$  and  $e^+e^- \rightarrow HZ$* , *JHEP* **11** (2014) 028, [arXiv:1406.1361 \[hep-ph\]](#).
- 73 N. Craig, J. Gu, Z. Liu, and K. Wang, *Beyond Higgs Couplings: Probing the Higgs with Angular Observables at Future  $e^+e^-$  Colliders*, *JHEP* **03** (2016) 050, [arXiv:1512.06877 \[hep-ph\]](#).
- 74 S. M. Barr and A. Zee, *Electric Dipole Moment of the Electron and of the Neutron*, *Phys. Rev. Lett.* **65** (1990) 21–24. [Erratum: *Phys. Rev. Lett.* 65, 2920 (1990)].
- 75 J. Fan and M. Reece, *Probing Charged Matter Through Higgs Diphoton Decay, Gamma Ray Lines, and EDMs*, *JHEP* **06** (2013) 004, [arXiv:1301.2597 \[hep-ph\]](#).
- 76 ACME Collaboration, J. Baron et al., *Order of Magnitude Smaller Limit on the Electric Dipole Moment of the Electron*, *Science* **343** (2014) 269–272, [arXiv:1310.7534 \[physics.atom-ph\]](#).
- 77 Y. T. Chien, V. Cirigliano, W. Dekens, J. de Vries, and E. Mereghetti, *Direct and indirect constraints on CP-violating Higgs-quark and Higgs-gluon interactions*, *JHEP* **02** (2016) 011, [arXiv:1510.00725 \[hep-ph\]](#).
- 78 R. Harnik, A. Martin, T. Okui, R. Primulando, and F. Yu, *Measuring CP violation in  $h \rightarrow \tau^+\tau^-$  at colliders*, *Phys. Rev.* **D88** (2013) 076009, [arXiv:1308.1094 \[hep-ph\]](#).
- 79 K. Hagiwara, S. Ishihara, R. Szalapski, and D. Zeppenfeld, *Low-energy effects of new interactions in the electroweak boson sector*, *Phys. Rev.* **D48** (1993) 2182–2203.
- 80 G. Gounaris et al., *Triple gauge boson couplings*, [arXiv:hep-ph/9601233 \[hep-ph\]](#).
- 81 L. Bian, J. Shu, and Y. Zhang, *Prospects for Triple Gauge Coupling Measurements at Future Lepton Colliders and the*

- 14 TeV LHC, *JHEP* **09** (2015) 206, [arXiv:1507.02238 \[hep-ph\]](#).
- 82 A. Falkowski, *Higgs Basis: Proposal for an EFT basis choice for LHC HXSWG*, LHCHXSWG-INT-2015-001 (March, 2015). <https://cds.cern.ch/record/2001958>.
- 83 ATLAS Collaboration, *Projections for measurements of Higgs boson cross sections, branching ratios and coupling parameters with the ATLAS detector at a HL-LHC*, ATL-PHYS-PUB-2013-014 (2013). <https://cds.cern.ch/record/1611186>.
- 84 ATLAS Collaboration, *HL-LHC projections for signal and background yield measurements of the  $H \rightarrow \gamma\gamma$  when the Higgs boson is produced in association with  $t$  quarks,  $W$  or  $Z$  bosons*, ATL-PHYS-PUB-2014-012 (2014). <https://cds.cern.ch/record/1741011>.
- 85 ATLAS Collaboration, *Update of the prospects for the  $H \rightarrow Z\gamma$  search at the High-Luminosity LHC*, ATL-PHYS-PUB-2014-006 (2014). <https://cds.cern.ch/record/1703276>.
- 86 ATLAS Collaboration, *Prospects for the study of the Higgs boson in the  $VH(bb)$  channel at HL-LHC*, ATL-PHYS-PUB-2014-011 (2014). <https://cds.cern.ch/record/1740962>.
- 87 ATLAS Collaboration, *Studies of the VBF  $H \rightarrow \tau\tau_{had}$  analysis at High Luminosity LHC conditions*, ATL-PHYS-PUB-2014-018 (2014). <https://cds.cern.ch/record/1956732>.
- 88 A. Falkowski, M. Gonzalez-Alonso, A. Greljo, and D. Marzocca, *Global constraints on anomalous triple gauge couplings in effective field theory approach*, *Phys. Rev. Lett.* **116** (2016) 011801, [arXiv:1508.00581 \[hep-ph\]](#).
- 89 A. Butter, O. J. P. Éboli, J. Gonzalez-Fraile, M. C. Gonzalez-Garcia, T. Plehn, and M. Rauch, *The Gauge-Higgs Legacy of the LHC Run I*, *JHEP* **07** (2016) 152, [arXiv:1604.03105 \[hep-ph\]](#).
- 90 R. Contino, A. Falkowski, F. Goertz, C. Grojean, and F. Riva, *On the Validity of the Effective Field Theory Approach to SM Precision Tests*, *JHEP* **07** (2016) 144, [arXiv:1604.06444 \[hep-ph\]](#).
- 91 A. Falkowski, M. Gonzalez-Alonso, A. Greljo, D. Marzocca, and M. Son, *Anomalous Triple Gauge Couplings in the Effective Field Theory Approach at the LHC*, *JHEP* **02** (2017) 115, [arXiv:1609.06312 \[hep-ph\]](#).
- 92 Z. Zhang, *Time to Go Beyond Triple-Gauge-Boson-Coupling Interpretation of  $W$  Pair Production*, *Phys. Rev. Lett.* **118** (2017) 011803, [arXiv:1610.01618 \[hep-ph\]](#).
- 93 S.-F. Ge, H.-J. He, and R.-Q. Xiao, *Probing new physics scales from Higgs and electroweak observables at  $e^+e^-$  Higgs factory*, *JHEP* **10** (2016) 007, [arXiv:1603.03385 \[hep-ph\]](#).
- 94 S.-F. Ge, H.-J. He, and R.-Q. Xiao, *Testing Higgs coupling precision and new physics scales at lepton colliders*, *Int. J. Mod. Phys. A* **31** (2016) 1644004, [arXiv:1612.02718 \[hep-ph\]](#). [55(2017)].
- 95 ATLAS Collaboration, *Search for the Standard Model Higgs and  $Z$  Boson decays to  $J/\psi\gamma$ : HL-LHC projections*, ATL-PHYS-PUB-2015-043 (2015). <http://cds.cern.ch/record/2054550>.
- 96 G. T. Bodwin, F. Petriello, S. Stoynev, and M. Velasco, *Higgs boson decays to quarkonia and the  $H\bar{c}c$  coupling*, *Phys. Rev. D* **88** (2013) 053003, [arXiv:1306.5770 \[hep-ph\]](#).
- 97 G. Perez, Y. Soreq, E. Stamou, and K. Tobioka, *Constraining the charm Yukawa and Higgs-quark coupling universality*, *Phys. Rev. D* **92** (2015) 033016, [arXiv:1503.00290 \[hep-ph\]](#).
- 98 I. Brivio, F. Goertz, and G. Isidori, *Probing the Charm Quark Yukawa Coupling in Higgs+Charm Production*, *Phys. Rev. Lett.* **115** (2015) 211801, [arXiv:1507.02916 \[hep-ph\]](#).
- 99 F. Bishara, U. Haisch, P. F. Monni, and E. Re, *Constraining Light-Quark Yukawa Couplings from Higgs Distributions*, [arXiv:1606.09253 \[hep-ph\]](#).
- 100 L. M. Carpenter, T. Han, K. Hendricks, Z. Qian, and N. Zhou, *Higgs Boson Decay to Light Jets at the LHC*, *Phys. Rev. D* **95** (2017) 053003, [arXiv:1611.05463 \[hep-ph\]](#).
- 101 A. Falkowski, *Effective field theory approach to LHC Higgs data*, *Pramana* **87** (2016) 39, [arXiv:1505.00046 \[hep-ph\]](#).
- 102 A. Falkowski and F. Riva, *Model-independent precision constraints on dimension-6 operators*, *JHEP* **02** (2015) 039, [arXiv:1411.0669 \[hep-ph\]](#).
- 103 ATLAS Collaboration, *Study of the double Higgs production channel  $H(\rightarrow b\bar{b})H(\rightarrow \gamma\gamma)$  with the ATLAS experiment at the HL-LHC*, ATL-PHYS-PUB-2017-001, CERN, Geneva, Jan, 2017. <https://cds.cern.ch/record/2243387>.
- 104 R. Contino et al., *Physics at a 100 TeV pp collider: Higgs and EW symmetry breaking studies*, CERN Yellow Report (2017) 255–440, [arXiv:1606.09408 \[hep-ph\]](#).
- 105 M. McCullough, *An Indirect Model-Dependent Probe of the Higgs Self-Coupling*, *Phys. Rev. D* **90** (2014) 015001, [arXiv:1312.3322 \[hep-ph\]](#).
- 106 S. Di Vita, C. Grojean, G. Panico, M. Riembau, and T. Vantalon, *A global view on the Higgs self-coupling*, *JHEP* **09** (2017) 069, [arXiv:1704.01953 \[hep-ph\]](#).
- 107 A. Azatov, R. Contino, G. Panico, and M. Son, *Effective field theory analysis of double Higgs boson production via gluon fusion*, *Phys. Rev. D* **92** (2015) 035001, [arXiv:1502.00539 \[hep-ph\]](#).
- 108 J. A. Aguilar-Saavedra, *A Minimal set of top anomalous couplings*, *Nucl. Phys. B* **812** (2009) 181–204, [arXiv:0811.3842 \[hep-ph\]](#).
- 109 J. A. Aguilar-Saavedra, *A Minimal set of top-Higgs anomalous couplings*, *Nucl. Phys. B* **821** (2009) 215–227, [arXiv:0904.2387 \[hep-ph\]](#).
- 110 Z. Liu, I. Low, and L.-T. Wang, *Higgs-Top Interactions at Future Circular  $e^+e^-$  Colliders*, [arXiv:2018.nnnn](#).
- 111 G. Li, H.-R. Wang, and S.-h. Zhu, *Probing CP-violating  $h\bar{t}t$  coupling in  $e^+e^- \rightarrow h\gamma$* , [arXiv:1506.06453 \[hep-ph\]](#).
- 112 E. Vryonidou and C. Zhang, *Dimension-six electroweak top-loop effects in Higgs production and decay*, [arXiv:1804.09766 \[hep-ph\]](#).
- 113 G. Durieux, *Precision constraints on the top-quark effective field theory at future lepton colliders*, PoS **DIS2017** (2018) 088, [arXiv:1708.09849 \[hep-ph\]](#).
- 114 Y. Gao, A. V. Gritsan, Z. Guo, K. Melnikov, M. Schulze, and N. V. Tran, *Spin determination of single-produced resonances at hadron colliders*, *Phys. Rev. D* **81** (2010) 075022, [arXiv:1001.3396 \[hep-ph\]](#).
- 115 S. Bolognesi, Y. Gao, A. V. Gritsan, K. Melnikov, M. Schulze, N. V. Tran, and A. Whitbeck, *On the spin and parity of a single-produced resonance at the LHC*, *Phys. Rev. D* **86** (2012) 095031, [arXiv:1208.4018 \[hep-ph\]](#).
- 116 I. Anderson et al., *Constraining anomalous HVV interactions at proton and lepton colliders*, *Phys. Rev. D* **89** (2014) 035007, [arXiv:1309.4819 \[hep-ph\]](#).
- 117 J. Alwall, P. Demin, S. de Visscher, R. Frederix, M. Herquet, F. Maltoni, T. Plehn, D. L. Rainwater, and T. Stelzer, *MadGraph/MadEvent v4: The New Web Generation*, *JHEP* **09** (2007) 028, [arXiv:0706.2334 \[hep-ph\]](#).
- 118 D. Curtin, R. Essig, S. Gori, P. Jaiswal, A. Katz, et al., *Exotic decays of the 125 GeV Higgs boson*, *Phys. Rev. D* **90** (2014) 075004, [arXiv:1312.4992 \[hep-ph\]](#).
- 119 LHC Higgs Cross Section Working Group Collaboration, D. de Florian et al., *Handbook of LHC Higgs Cross Sections. 4. Deciphering the Nature of the Higgs Sector*, [arXiv:1610.07922 \[hep-ph\]](#).
- 120 Z. Liu, L.-T. Wang, and H. Zhang, *Exotic decays of the 125 GeV Higgs boson at future  $e^+e^-$  lepton colliders*, [arXiv:1612.09284 \[hep-ph\]](#).

- 121 J. Liu, Z. Liu, and L.-T. Wang, *Long-lived particles at the LHC: catching them in time*, [arXiv:1805.05957 \[hep-ph\]](#).
- 122 A. Thamm, R. Torre, and A. Wulzer, *Future tests of Higgs compositeness: direct vs indirect*, *JHEP* **07** (2015) 100, [arXiv:1502.01701 \[hep-ph\]](#).
- 123 J. Gu, H. Li, Z. Liu, S. Su, and W. Su, *Learning from Higgs Physics at Future Higgs Factories*, *JHEP* **12** (2017) 153, [arXiv:1709.06103 \[hep-ph\]](#).
- 124 J. Fan, M. Reece, and L.-T. Wang, *Precision Natural SUSY at CEPC, FCC-ee, and ILC*, [arXiv:1412.3107 \[hep-ph\]](#).
- 125 R. Essig, P. Meade, H. Ramani, and Y.-M. Zhong, *Higgs-Precision Constraints on Colored Naturalness*, *JHEP* **09** (2017) 085, [arXiv:1707.03399 \[hep-ph\]](#).
- 126 N. Craig, C. Englert, and M. McCullough, *New Probe of Naturalness*, *Phys. Rev. Lett.* **111** (2013) 121803, [arXiv:1305.5251 \[hep-ph\]](#).
- 127 Z. Chacko, H.-S. Goh, and R. Harnik, *The Twin Higgs: Natural electroweak breaking from mirror symmetry*, *Phys. Rev. Lett.* **96** (2006) 231802, [arXiv:hep-ph/0506256 \[hep-ph\]](#).
- 128 G. Burdman, Z. Chacko, H.-S. Goh, and R. Harnik, *Folded supersymmetry and the LEP paradox*, *JHEP* **02** (2007) 009, [arXiv:hep-ph/0609152 \[hep-ph\]](#).
- 129 N. Craig, M. Farina, M. McCullough, and M. Perelstein, *Precision Higgsstrahlung as a Probe of New Physics*, *JHEP* **03** (2015) 146, [arXiv:1411.0676 \[hep-ph\]](#).
- 130 S. Profumo, M. J. Ramsey-Musolf, C. L. Wainwright, and P. Winslow, *Singlet-catalyzed electroweak phase transitions and precision Higgs boson studies*, *Phys. Rev.* **D91** (2015) 035018, [arXiv:1407.5342 \[hep-ph\]](#).
- 131 A. Katz and M. Perelstein, *Higgs Couplings and Electroweak Phase Transition*, *JHEP* **07** (2014) 108, [arXiv:1401.1827 \[hep-ph\]](#).
- 132 A. Noble and M. Perelstein, *Higgs self-coupling as a probe of electroweak phase transition*, *Phys. Rev.* **D78** (2008) 063518, [arXiv:0711.3018 \[hep-ph\]](#).
- 133 B. Henning, X. Lu, and H. Murayama, *What do precision Higgs measurements buy us?*, [arXiv:1404.1058 \[hep-ph\]](#).
- 134 S. Profumo, M. J. Ramsey-Musolf, and G. Shaughnessy, *Singlet Higgs phenomenology and the electroweak phase transition*, *JHEP* **08** (2007) 010, [arXiv:0705.2425 \[hep-ph\]](#).
- 135 D. Curtin, P. Meade, and C.-T. Yu, *Testing Electroweak Baryogenesis with Future Colliders*, *JHEP* **11** (2014) 127, [arXiv:1409.0005 \[hep-ph\]](#).
- 136 Q.-H. Cao, F. P. Huang, K.-P. Xie, and X. Zhang, *Testing the electroweak phase transition in scalar extension models at lepton colliders*, *Chin. Phys.* **C42** (2018) 023103, [arXiv:1708.04737 \[hep-ph\]](#).
- 137 P. Huang, A. J. Long, and L.-T. Wang, *Probing the Electroweak Phase Transition with Higgs Factories and Gravitational Waves*, *Phys. Rev.* **D94** (2016) 075008, [arXiv:1608.06619 \[hep-ph\]](#).